

Parity-Time Symmetric Telemetry Systems for Wearable and Implantable Sensors

BY

MARYAMSADAT SAKHDARI

B.S., IRAN University of Science and Technology, Tehran, 2009

M.S., Tarbiat Modares University, Tehran, 2013

DISSERTATION

Submitted as partial fulfillment of the requirements
for the degree of Doctor of Philosophy in Electrical and Computer Engineering
in the Graduate College of the
University of Illinois at Chicago, 2020

Chicago, Illinois

Defense Committee:

Pai-Yen Chen, Chair and Advisor
Danilo Erricolo
Piergiorgio Uslenghi
Besma Smida
Nan Jiang, Chemistry

Copyright by
Maryam Sakhdari
2020

To Samira, my best friend forever and ever

ACKNOWLEDGMENTS

First of all, it would be impossible to overstate the thanks I owe to Pai-Yen, whose mentorship for the past four years has been beyond formative. It is a great opportunity for me to work on my Ph.D. studies with Prof. Pai-Yen Chen as my adviser who have been supportive of my career goals and who worked actively to provide me with the protected academic time to pursue those goals. Thanks for everything!

I am grateful to all of those with whom I have had the pleasure to work during this and other related projects. Each of the members of my Dissertation Committee has provided me extensive personal and professional guidance and taught me a great deal about both scientific research and life in general.

I thank all the staff members of the ECE department at both Wayne State University and University of Illinois at Chicago for their help during my Ph.D. study.

Very special thanks to the great team in NuCurrent Inc for all supports and the best work experience with a talented and friendly group in most innovative company in Chicago.

Nobody has been more important to me in the pursuit of this project than the members of my family. I would like to thank my parents; whose love and guidance are with me in whatever I pursue. They are the ultimate role models. Most importantly, I wish to thank my best friend and my research partner, Mehdi, who provides unending inspiration.

TABLE OF CONTENTS

<u>CHAPTER</u>	<u>PAGE</u>
I. INTRODUCTION	1
II. Generalized Parity-Time Symmetry for Enhanced Sensor Telemetry	5
2.1 Telemetric sensing based on compact, battery-less wireless sensors	5
2.2 Theory of Generalized PT-Symmetry	8
2.3 Experimental demonstration of <i>PT/PTX</i> -symmetric telemetric microsensor systems	13
2.4 Methods	23
Exceptional point and phase transitions	23
Wireless measurement setups	25
2.5 Design and Characterization of MEMS-Based Pressure Sensor	25
Design of MEMS-Actuated Capacitive Pressure Sensor	25
Design of Microcoil Inductor	29
2.6 Design of Negative Resistance Converter (NRC)	32
2.7 Microfabrication and Characterization of the Wireless Pressure Sensor	37
Fabrication of Wireless Pressure Sensors by the MEMS processes	37
2.8 Measurement Setup for the MEMS Wireless Pressure Sensors	38
2.9 Analysis of PTX-Symmetric Electronic Systems	41
PTX-Symmetric Circuits in the Parallel Configuration	41
Reflectionless Property and Impedance Matching	43
2.10 Conclusions	46
References	48
III. Ultrasensitive, Parity-Time Symmetric Wireless Reactive and Resistive Sensors	50

TABLE OF CONTENTS (continued)

<u>CHAPTER</u>	<u>PAGE</u>
3.1 Wireless Reactive and Resistive Sensors	50
3.2 Theory of PT-Symmetric Telemetry sensor systems	52
3.3 Implementation and Characterization of Wireless Capacitive Sensors	57
3.4 Implementation and Characterization of Wireless Resistive Sensors.....	61
3.5 Conclusions	64
References	65
 VI. Ultrasensitive Wireless Displacement Sensing Enabled by PT-Symmetric Telemetry	 70
4.1 Displacement sensing systems	70
4.2 PT-Symmetric Telemetry	74
4.3 Experimental Demonstration of PT-Symmetric IDS System.	78
4.5 Conclusions	83
References	84
 V. Ultra-Sensitivity with Divergent Exceptional Points for Radio-Frequency Telemetry	 88
5.1 PT-symmetry and divergent exceptional points (DEPs).....	88
5.2 Divergent exceptional points in <i>PT</i> -symmetric electronic circuit.....	90
5.3 RF reader designs and wireless measurement setups.....	99
5.4 Physical Bounds of the Bifurcation Effect in PT-Symmetric Telemetry Systems	100
5.5 Generalized <i>N</i> th-Order <i>PT</i> -Symmetric Electronic Systems.....	103
5.6 Conclusion	110
References	112
 VI. Robust Extended-Range Wireless Power Transfer Using a Higher-Order PT-Symmetric Platform	 114

TABLE OF CONTENTS (continued)

<u>CHAPTER</u>	<u>PAGE</u>
6.1 wireless power transfer	114
6.2 Higher-order PT-symmetric wireless powering	117
6.3 Experimental demonstration of WPT system with third-order PT symmetry	124
6.4 Method	128
Generalized theory for higher-order PT WPT systems	128
6.5 Dynamic control of PT symmetry in circuits	130
6.6. Temporal responses of the third-order PT-symmetric circuit.....	131
6.7 Characterization of magnetic coupling strength	134
6.8 Evolvement of reflection as a function of magnetic coupling strength	134
6.9 Evolvement of transmission coefficient as a function of intermediate coil loss	135
6.10 Conclusion.....	137
References	139
VII. Low-Threshold Lasing and Coherent Perfect Absorption in the Generalized PT-Symmetric Optical Structures.....	143
7.1 Coherent Perfect Absorber Laser.....	143
7.2 The concept of the generalized PT-symmetric optical systems.....	144
7.3 Implementations of generalized PT-symmetric CPA-laser.....	150
7.4 Metasurface designs	156
7.5 Scattering from an individual metasurface.....	157
7.5 Conclusion	157
References	158
VIII. Conclusion and future works	160

TABLE OF CONTENTS (continued)

<u>CHAPTER</u>	<u>PAGE</u>
Appendix: Copyright permissions.....	162
Vita	177

LIST OF FIGURES

<u>FIGURE</u>	<u>PAGE</u>
<p>Figure 2-1 Non-Hermitian telemetric sensor system. a Schematics of a typical wireless implantable or wearable sensor system, where a loop antenna is used to interrogate the sensor via inductive (magnetic) coupling. The parameters to be sensed can be accessed by monitoring the reflection coefficient of the sensor, typically based on an RLC resonant circuit consisting of a micromachined varactor and inductor. b Equivalent circuit model for the proposed PTX-symmetric telemetric sensor system, where x is the scaling coefficient of the reciprocal-scaling operation X. If $x = 1$, the PTX system converges to the PT-symmetric case. In the close-loop normal mode analysis, an RF signal generator with a source impedance Z_0, connected to the reader, is represented by $-Z_0$. The inset shows the AC model for the Colpitts circuit with a positive feedback, which achieves an equivalent negative resistance and an equivalent series capacitance.....</p>	7
<p>Figure 2-2 MEMS-based wireless pressure sensor. a Schematics of a MEMS-based pressure sensor, which consists of a variable parallel-plate capacitor c connected in series with a microcoil inductor (L), effectively forming a resonant LC tank circuit. Increasing the internal pressure by an air compressor regulator increases the displacement of the upper membrane electrode, thereby reducing the capacitance of the MEMS varactor. b Top view of the microfabricated wireless pressure sensor on a flexible polymer substrate. c Three-dimensional surface profile of the sensor in b, which was measured by scanning white light interferometry (SWLI). d Measurement (dots) and theoretical (solid line) results for the total capacitance in response to pressure (); insets show the displacement of the upper membrane electrode measured by SWLI. Due to the cylindrical symmetry of the capacitor, only displacements in the radial direction (from point A to point B in c) are shown.....</p>	12
<p>Figure 2-3 Evolution of eigenfrequencies and reflection spectra as a function of the non-Hermiticity parameter γ and coupling strength κ. (a,b) Real (left) and imaginary (right) eigenfrequency isosurface normalized by ω_0 in the (γ, κ) parameter space for a PT-symmetric wireless pressure sensor and b conventional passive wireless pressure sensor, where an active reader and a passive loop-antenna are respectively used to interrogate the micromachined sensor</p> <p>in Figure 2-2. c Reflection spectra against the frequency for the PT-symmetric wireless pressure sensor with different coupling strengths, showing a transition from the broken PT-symmetric phase ($\kappa = 0.4$) to the exact PT-symmetric phase ($\kappa = 0.48, 0.49$ and 0.5) when κ increases; here $\gamma = 2.26$, corresponding to applied pressure of 100 mmHg, and $\omega_0 / 2\pi = 180$ MHz. Frequencies and linewidths of reflection dips in c are consistent with the eigenfrequency evolution in a. Solid and dashed lines denote experimental data and theoretical results obtained from the equivalent circuit model in Figure 2-1.....</p>	15

LIST OF FIGURES (continued)

<u>FIGURE</u>	<u>PAGE</u>
<p>Figure 2-4 Pressure-induced spectral changes for conventional and PT-symmetric telemetric sensors. (a,b) Magnitude of reflection coefficient for the MEMS-based pressure sensor (Figure 4) interrogated by a the conventional passive loop antenna and b the active reader realizing a PT-symmetric dimer, under different applied pressures. Solid and dashed lines denote experimental data and theoretical results obtained from the equivalent circuit models.....</p>	18
<p>Figure 2-5 Evolution of the eigenfrequencies and reflection spectra for PTX-symmetric telemetric sensors. a Real (left) and imaginary (right) eigenfrequency as a function of the non-Hermiticity parameter γ for the fully-passive (red hollow circle; Figure 7a), PT-symmetric (blue dot), and PTX-symmetric (green and yellow dots; b and c) telemetric pressure sensors. Solid lines denote theoretical predictions (see Method). (b,c) Magnitude of the reflection coefficient for the PTX-symmetric telemetric sensor systems; here scaling coefficients x used in b and c are 3 and 1/3. Solid and dashed lines in b and c denote the experimental data and theoretical predictions.....</p>	21
<p>Figure 2-6 Maximum displacement of the movable electrode against applied pressure for the MEMS varactor in Fig. 2-2 of the main text.....</p>	27
<p>Figure 2-7 Capacitance against the applied pressure for the MEMS varactor in Fig. 2-2 of the main text.....</p>	29
<p>Figure 2-8 Configurations and physical parameters of planar coils used in the reader and the sensor.....</p>	30
<p>Figure 2-9 a Schematics of the reader circuit for the PT/PTX-symmetric telemetric sensors, consisting of a negative resistance converter (Colpitts oscillator) connected to a microcoil inductor, fed by a RF source (vector network analyzer; VNA). b Input impedance of an open-circuited Colpitts-type circuit $Z_{in}=v_i/i_i$, without connecting to any reactive element. The complex input impedance can be decomposed into a series combination of an equivalent negative resistance $-R_{eq}$ and an equivalent capacitance C_{Eq}. 2- (c)Equivalent circuit model for the PT/PTX-symmetric telemetric sensor system, in which the reader is a series -RLC tank where $-R$ and C are contributed by the Colpitts-type oscillator. (d) Layout and (e) fabricated PCB-based active reader used in the PT-symmetric sensor.....</p>	32
<p>Figure 2-10 (a) Reflection spectra of the NRC versus frequency under different biasing conditions; here, solid and dashed lines represent the experimental and simulation results, and dotted lines</p>	

LIST OF FIGURES (continued)

<u>FIGURE</u>	<u>PAGE</u>
represent the simulation results without considering the parasitic capacitance. Equivalent (b) resistance and (c) capacitance and parasitic components for the NRC in (a). The highlighted areas show the frequency range of interest, where the values of negative resistance and capacitance are nearly constant. The effects of L_p and C_p are negligible if the operating frequency is much lower than the cutoff frequency of the transistor.....	36
Figure 2-11 Schematics of fabrication processes for the MEMS-based IOP sensor in Fig. 2-2 in the main text.....	37
Figure 2-12 Measurement Setup for the MEMS wireless pressure sensor.....	39
Figure 2-13 Variations of eigenfrequencies with the pressure-driven capacitance for conventional and PT-symmetric wireless pressure sensor systems. The pressure corresponding to the specific capacitance can be found in Fig. 2-7. I note that a PTX-symmetric sensor displays the same frequency response because PT and PTX systems share the same eigenspectrum.....	41
Figure 2-14 PTX-symmetric electronic system realized with the parallel-circuit configuration.....	41
Figure 2-15 (a) PTX-symmetric circuits with the RF excitation source connected to the active –RLC tank. (b) Reflection spectrum for the single-port circuit in (a), under different values of x . (c) PTX-symmetric circuits with the RF excitation source connected to the passive RLC tank; the circuits in (a) and (c) share the same eigenfrequencies, as they represent the same type of –RLC/RLC dimer in the coupled-mode analysis. (d) Reflection spectrum the single-port circuit in (a), under different values of y . In the PTX-symmetric circuits, the resonant frequencies remain constant, while the bandwidth (or Q-factor) can be tailored by varying the scaling coefficient x or y	44
Figure 3-1 a Schematics of a wireless passive <i>RLC</i> sensor, inductively coupled to a coil reader, and its equivalent circuit model. b Equivalent-circuit expression of the <i>PT</i> -symmetric wireless sensor system.....	51
Figure 3-2 a Real (left) and imaginary (right) eigenfrequency versus the non-Hermiticity parameter γ for the <i>PT</i> -symmetric circuit in Fig. 2-1b. b is similar to (a), but for measurement results obtained by the micro-coil reader shown in Fig. 1a. Here, eigenfrequencies are in units of ω_0	53

LIST OF FIGURES (continued)

<u>FIGURE</u>	<u>PAGE</u>
<p>Figure 3-3 a Contours of reflection coefficient, as a function of the normalized operating frequency and the non-Hermiticity parameter, for the circuit of (a) the conventional wireless sensor system [Fig. 3-1(a)] and b the <i>PT</i>-symmetric one [Fig. 3-1(b)]; here the coupling strength $\kappa = 0.6$ and the input impedance of the RF source $Z_0 = 0.33 R$.....</p>	56
<p>Figure 3-4 a Circuit diagram for the active reader consisting of an NRC, which is equivalent to a lumped negative resistor and b its practical implementation using the printed circuit board technique.....</p>	57
<p>Figure 3-5 a Measured reflection coefficient for a passive <i>RLC</i> pseudo-sensor with an effective resistance $R = 150 \Omega$ and an effective inductance $L = 300 \text{ nH}$, which is inductively coupled by (a) the conventional coil-antenna reader shown in Fig. 3-1a, and b the active reader ($-RLC$ tank in Fig. 3-1b) that accomplishes the <i>PT</i>-symmetric electronic system. The effective capacitance C of the <i>RLC</i> sensor is varied from 7 pF to 2 pF.....</p>	59
<p>Figure 3-6 a Schematics of the <i>PT</i>-symmetric wireless resistive sensor system. b Real (left) and imaginary (right) eigenfrequency versus the non-Hermiticity parameter γ for the <i>PT</i>-symmetric circuit in (a). The resistance of the pseudo <i>RLC</i> sensor is varied from 190 Ω to 300 Ω, corresponding to the change of γ from 2.8 to 1.9. (b) is similar to (a), but for measurement results obtained by the micro-coil reader shown in Fig. 3-1a. Here, eigenfrequencies are in units of ω_0.....</p>	61
<p>Figure 3-7 a Measured reflection coefficient for a (pseudo) <i>RLC</i> sensor with effective capacitance $C = 2 \text{ pF}$ and effective inductance $L = 600 \text{ nH}$, which is wirelessly read by (a) the conventional coil-antenna reader shown in Fig. 3-1a, and b the active reader ($-RLC$ tank in Fig. 6b). The effective resistance R of the pseudo <i>RLC</i> sensor is varied from 190 Ω to 300 Ω.....</p>	62
<p>Figure 4-1 <i>PT</i>-symmetric inductive displacement sensor (IDS) system. a Schematics (left) and measurement setup (right) for a wireless IDS system, in which a tag (<i>RLC</i> resonant tank) is inductively coupled to a reader antenna (planar inductive coil). b Equivalent circuit model for the <i>PT</i>-symmetric IDS system, in which an active reader ($-RLC$ tank) is used to interrogate tags such that the circuit is invariant after spatial inversion and time reversal. In the close-loop (normal mode) analysis, a RF signal generator with source impedance Z_0 is represented by $-Z_0$, as it provides energy to excite the circuit. The inset pictures show the PCB-based prototypes for the DC-biased active reader (left) and the passive tag (right).....</p>	72

LIST OF FIGURES (continued)

<u>FIGURE</u>	<u>PAGE</u>
<p>Figure 4-2 Complex eigenfrequency of <i>PT</i>-symmetric electronic system. Contours of a real and b imaginary eigenfrequency as a function of the non-Hermiticity parameter γ and the coupling coefficient κ for the <i>PT</i>-symmetric RF circuit in Fig. 4-1b.....</p>	75
<p>Figure 4-3 Effect of normal and tangential displacement on the (inductive) coupling coefficient κ. (a,b) Calculated coupling coefficient versus normal displacement Δz and tangential displacement Δx; here, the inductance ratio between the reader coil and the tag coil, L_R/L_T, is also varied.....</p>	77
<p>Figure 4-4 Reflection spectra for <i>PT</i>-symmetric and conventional (fully-passive) displacement sensors, under different values of Δx (tangential displacement). The reflection coefficient versus frequency for the <i>PT</i>-symmetric IDS systems with a $\gamma = 4.9$, b $\gamma = 2.45$ and c $\gamma = 2$, and for d the conventional passive IDS system using a coil-antenna reader to read the same tag as (c); here, solid and dashed lines represent experimental and analytical results, respectively. When a tangential displacement is introduced, the coupling strength between the reader and tag coils is also varied, which in turn leads to a shift in the resonance frequency. I note that results on the bottom panel of (a) and (b) are obtained for systems operated close to the exceptional point, whereas the result on the bottom panel of (c) designates the broken symmetry phase, with resonance becomes progressively weaker as κ decreases (or Δx increases).....</p>	79
<p>Figure 4-5 Evolution of the eigenfrequency for <i>PT</i>-symmetric and conventional (fully-passive) IDS systems. Contours of real part of eigenfrequency as a function of Δx and Δz for the <i>PT</i>-symmetric IDS systems with a $\gamma = 4.9$, b $\gamma = 2.45$ and c $\gamma = 2$, and for d the conventional fully-passive IDS system using a coil-antenna reader to read the same tag as (c); here, colored surface and dots represent theoretical and experimental results, respectively.....</p>	81
<p>Figure 5-1 Non-Hermitian <i>PT</i>-symmetric telemetric electronic systems. (a, b) Schematics of (a) the standard <i>PT</i>-symmetric telemetric system and (b) the three-elements <i>PT</i>-symmetric system formed by electronic oscillators. (c) Experimental setup of the three-elements <i>PT</i>-symmetric telemetric system. (d) Evolution of complex eigenfrequencies as a function of the non-Hermiticity parameter γ and the coupling strength κ for the third-order <i>PT</i>-symmetric system in b and c. Here, the system's exceptional point (EP) and critical point (CP) are highlighted.....</p>	89
<p>Figure 5-2 Evolution of eigenfrequencies and reflection spectra as a function of the non-Hermiticity parameter γ for the standard (two-elements) and three-elements <i>PT</i>-symmetric telemetric systems. a. Experimental and theoretical complex eigenfrequencies, varying a function</p>	

LIST OF FIGURES (continued)

<u>FIGURE</u>	<u>PAGE</u>
of non-Hermiticity parameter γ , for the three-elements PT -symmetric system (red circles), the standard PT -symmetric system (blue squares), and the conventional telemetric system using a micro-coil reader (green diamonds). In all telemetric systems, the coupling strength κ is fixed to 0.3. (b, c) Magnitude of the reflection coefficient versus frequency for the three-elements PT -symmetric system and the standard PT -symmetric system. Both systems are controlled to operate around the exceptional point (EP), under the coupling strength $\kappa=0.3$. Solid and dashed lines denote experimental and theoretical results, respectively.....	93
Figure 5-3 Multi-links multi-stages PT -symmetric electronic system. a. Schematics of a multi-links three-elements PT -symmetric system with N' coplanar spiral inductors in the intermediary. b. Experimental setup for the PT -symmetric telemetric system in a, with $N'=2$ (four links).....	96
Figure 5-4 Evolution of eigenfrequencies and reflection spectra as a function of the non-Hermiticity parameter γ for the four-links three-elements PT -symmetric telemetric system. a. Experimental and theoretical complex eigenfrequencies, varying a function of non-Hermiticity parameter, for the dual-links three-stages PT -symmetric telemetric system in Fig. 5-3b with $\kappa_c = 0.49$ (red circles), the standard PT -symmetric telemetric system in Fig. 5-1a with $\kappa_c = 0.7$ (blue squares), and the conventional one using a micro-coil reader with $\kappa_c = 0.7$ (green diamonds). (b, c) Magnitude of the reflection coefficient versus frequency for the four-links third-stages PT -symmetric telemetric system in a, in comparison with the standard PT -symmetric telemetric system; here, the non-Hermiticity parameters γ is varied from 0.77 to 2.1. Note that if $\gamma < 1.3$, the standard PT -symmetric system ($\gamma_{EP}=1.3$) operates in the broken phase, which exhibits a weak resonance with a low quality factor. Solid and dashed lines denote experimental and theoretical results, respectively.....	99
Figure 5-5 Generalized N th-order PT -symmetric electronic systems. Schematic illustration for the PT -symmetric telemetric system comprising (a) even-numbered and (b) odd-numbered oscillators, as well as (c) a pair of $-RLC$ and RLC oscillators that are coupled via one or multiple neutral intermediators.....	103
Figure 5-6 Evolutions of eigenspectra for PT -symmetric electronic systems in Fig. 5-9, with different orders ($N = 4, 5, 6, 7, 8, 9$); here, the coupling strength is fixed to $\kappa = 0.5$	105

LIST OF FIGURES (continued)

<u>FIGURE</u>	<u>PAGE</u>
<p>Figure 5-7 (a) Coupling strength κ_c for different <i>PT</i>-symmetric electronic systems in Fig. 5-9. κ_c has an upper bound of 1 (gray area is invalid) and a lower bound of 0.5. (b) Exceptional and critical points (γ_{EP} and γ_c) for different <i>PT</i>-symmetric electronic systems in Fig. 5-9, under a fixed coupling strength $\kappa = 0.5$</p>	107
<p>Figure 5-8 Eigenfrequencies versus the non-Hermiticity parameter for the <i>PT</i>-symmetric electronic system in figures 5-9c, with different numbers of intermediary and coupling strengths.....</p>	108
<p>Figure 6-1. a Schematics for standard (i), third-order (ii), and other higher-order (iii) <i>PT</i>-symmetric electronic systems consisting of electronic molecules with gain (red), neutral (gray) and loss (blue) properties. b Third-order <i>PT</i>-symmetric wireless power transfer system, where a robot car (loss) is wirelessly charged by a platform consisting of a repeater (neutral) and an active transmitter (gain). The inductive coupling strength between the intermediate and receiver coils (κ) is random, and that between the transmitter and intermediate coils (κ') is tuned by rotating the transmitter coil and a feedback algorithm, such that $\kappa = \kappa'$ and <i>PT</i> symmetry is preserve.....</p>	116
<p>Figure 6-2 Evolution of the real (top) and imaginary (bottom) parts of eigenfrequencies as a function the gain-loss parameter γ and the coupling strength κ, for the a third-order and b standard <i>PT</i>-symmetric electronic systems in Fig. 6-1(a) (see type i and ii).....</p>	120
<p>Figure 6-3 Evolvment of reflection and transmission spectra for the a third-order with the coupling strength κ varied from 0.14 to 0.34 and b standard <i>PT</i>-symmetric WPT systems with the coupling strength κ varied from 0.2 to 0.58. Experimental and theoretical results are denoted by solid and dashed lines, respectively.....</p>	126
<p>Figure 6-4 Efficiency of power transfer as a function of the gain-loss parameter γ and the coupling strength κ, for the frequency-locked (1.3 MHz) standard and third-order <i>PT</i>-symmetric WPT systems, here d is the center to center distance between two neighbor coil.....</p>	127
<p>Figure 6-5 a Control of the tilt angle of the transmitter coil by a servo motor SG90. b Measurment setup for the TO-<i>PT</i> WPT system which wirelessly charges a robot car battery (left), and the LabVIEW interface for the feedback control of rotation of the transmitter coil (right).....</p>	130

LIST OF FIGURES (continued)

<u>FIGURE</u>	<u>PAGE</u>
<p>Figure 6-6 q v.s. τ. Temporal dynamics of the charge stored in the capacitor of the $-RLC$ tank (red line), LC tank (black dashed line), and RLC tank (blue line); here, $\gamma = 1.5$ and $\kappa = 0.5$, which lead to the exact phase with $\omega_{1,2,3,4,5,6} = \pm 1, \pm 1.4844$, and ± 0.9527.....</p>	133
<p>Figure 6-7 q v.s. τ. Temporal dynamics of the absolute charge stored in the capacitor of the $-RLC$ tank (red line), LC tank (black dashed line), and RLC tank (blue line); here, $\gamma = 1$ and $\kappa = 0.5$, which lead to the broken phase.....</p>	133
<p>Figure 6-8 a Measurement setup for the coupling strenght between two coils. b Coupling strength as a function of distance (x, y); theoretical and experimental results are denoted by the isosurface and symbols.....</p>	134
<p>Figure 6-9 Magnitude of reflection coficient as a function of frequency and coupling strength for the a standard and b third-order PT-symmetric circuits.</p>	135
<p>Figure 6-10 a Evolution of the real parts of eigenfrequencies as a function of the coupling strength κ, here, $\gamma = 7.7$ and $\varsigma = 0, 0.1, \text{and } 0.2$, b Transmission coefficient at the resonance frequency $\omega = 1$, as a function of the coupling strength κ, and loss in the intermediate coil for $\gamma = 1.4, 2.4$, and 7.7, for the third-order PT-symmetric circuits.....</p>	136
<p>Figure 7-1 Schematics for (a) the PT-symmetric and (b) the generalized PT (gPT)-symmetric optical structures (top) comprising paired gain and loss components, and their corresponding transmission-line network model (bottom). Provided that the structured gain and loss media have subwavelength thickness and unit cells, their optical behaviors can be described by a surface admittance (or surface impedance). In the gPT-symmetric system, if the scaling coefficient $\kappa \neq 1$, the gain-loss balance, as a weaker constraint of PT-symmetry, can be broken, while the scattering properties remain the same at the design frequency.....</p>	145
<p>Figure 7-2 (a) Real (solid) and imaginary (dashed) parts of permittivity of active gain media with different linewidths of amplification γ. (b) Transmittance spectra of gPT-symmetric optical structures in Fig. 7-1b, of which the amplifying metasurface made of gain media in (a); dashed lines and symbols represent analytical and full-wave simulation results, respectively. By varying the scaling coefficient κ, the CPA-laser point with eigenvalues going to zero and infinite (inset) can be achieved, regardless of the resonant gain magnitude. Here, I consider only one excitation source, and, thus, only the lasing mode is observed.....</p>	150

LIST OF FIGURES (continued)

<u>FIGURE</u>	<u>PAGE</u>
<p>Figure 7-3 Contours of Transmittance as functions of γ and κ for the gPT-symmetric optical system in Fig. 7-1(b); here, the locus of optimal (γ, κ) sets, giving the lasing effect, for an individual active metasurface (inset of Fig. 7-3(b)), PT- and gPT-symmetric optical systems are presented for comparison. For a large γ, corresponding to a weak resonant gain, the lasing effect can only be achieved with the gPT-symmetric metasurfaces. If $\kappa = 1$, the system would degenerate into the common PT-symmetric setup, as highlighted with a star. (b) is similar to (a), but for an individual active metasurface, showing an upper bound for lasing in terms of γ. Contours of Transmittance as functions of γ and x (electrical length between amplifying and attenuating surfaces) for the PT-symmetric optical system in Fig. 7-1(a), varying the dielectric permittivity of spacer $\epsilon = \epsilon_0 / \kappa^2$. In this case, a physical bound similar to an individual active metasurface in (b) is still obtained.....</p>	153
<p>Figure 7-4 (a) Transmittance spectra for CPA-laser devices based on gPT-symmetric metasurfaces, which are designed using different scaling coefficients; here, lasing and CPA modes are excited by single and two coherent incident waves. (b) Snapshots of electric fields for the gPT-symmetric CPA-laser in (a) ($\kappa = 1$), operated in the lasing mode (top) and the CPA mode (bottom).....</p>	155

SUMMARY

A generalized parity-time (PT)-symmetric telemetric sensing technique, which enables new mechanisms to manipulate radio frequency (RF) interrogation between the sensor and the reader, in order to boost the effective Q -factor and sensitivity of wireless microsensors was theoretically proposed and experimentally shown. This sensing technique which used MEMS-based wireless pressure sensors operating in the radio-frequency spectrum, overcame the long-standing challenge of implementing a miniature wireless microsensor with high spectral resolution and high sensitivity, and opened opportunities to develop loss-immune high-performance sensors, due to gain-loss interactions via inductive coupling and eigenfrequency bifurcation resulting from the PT (PTX)-symmetry.

It was shown that a real and constant eigenfrequency in specific higher-order of the generalized PT -symmetric electronic systems was exploited to realize a robust wireless power transfer platform locked to the frequency of operation. This PT system, provided breakthrough in dynamic and alignment-free wireless charging technology with extended range wireless charging and sensing at the same time.

I. INTRODUCTION

The concept of PT -symmetry originates from the quantum physics, where a non-Hermitian Hamiltonian can have real eigenfrequencies, if the Schrödinger system is invariant under operations of spatial reflection P and time reversal T . Thanks to formal similarities between Schrödinger and Helmholtz equations, PT -symmetry can be experimentally demonstrated in electromagnetic systems with balanced gain and loss, including transmission-line networks, coupled waveguides/cavities, and lumped-element circuits. PT -symmetric optical structures with balanced gain and loss have unveiled several exotic properties and applications, including unidirectional scattering, coherent perfect absorber-laser, single-mode micro-ring laser, and optical non-reciprocity. Inspired by optical schemes, other PT -symmetric systems in electronics (sub-radiofrequency, 30 KHz and below) acoustics and optomechanics have also been recently reported. The exceptional points (EPs) arising in these systems, found at the bifurcations of eigenfrequencies near the PT -phase transition, show potential to enhance the sensitivity of photonic sensors. Similar to earlier experiments in optical systems, the realization of PT -symmetry in an electronic circuit is achieved when the gain and loss parameters, namely R and $-R$, are delicately balanced, and the reactive components, L and C , satisfy mirror symmetry. This circuit platform of PT -symmetric electronic system leads to sharp and deep resonances, beyond the limitations for passive circuit systems, thus providing improved spectral resolution and modulation depth for sensing. The beneficial of the PT -symmetric electronic system, however, is not limited to sensing application and may be extended to wireless power transfer, non-destructive eddy current test and inductor-less active filter system.

This thesis attempts to fulfil three major porpoises: (1) Generalized Parity-Time Symmetry for Enhanced Sensor Telemetry, (2) Ultra-Sensitivity with Divergent Exceptional Points for Radio-Frequency Telemetry, (3) Robust Extended-Range Wireless Power Transfer Using a Higher-Order PT-Symmetric Platform.

Chapter 2 provides an introduction of the concept of isospectral party-time-reciprocal scaling (*PTX*) symmetry and shows that it can be used to build a new family of radio-frequency wireless microsensors exhibiting ultra-sensitive responses and ultra-high resolution, which are well beyond the limitations of conventional passive sensors. In this chapter, I show theoretically and demonstrate experimentally using microelectromechanical (MEMS)-based wireless pressure sensors, that *PTX*-symmetric electronic systems share the same eigenfrequencies as their parity-time (*PT*)-symmetric counterparts, but crucially have different circuit profiles and eigenmodes. This simplifies the electronic circuit design and enables further enhancements to the extrinsic *Q*-factor of the sensors.

Chapter 3, here I propose a new readout paradigm for enhancing the performance of wireless passive resistor-inductor-capacitor (*RLC*) sensors. Here, I consider a passive *RLC* sensor inductively coupled to an active reader, with the equivalent circuit of the whole telemetry system satisfying the parity-time (*PT*) symmetry or space-time reflection symmetry. I demonstrate that the *PT*-symmetric wireless sensor system, when compared to conventional interrogation techniques using a passive coil reader, may provide significantly improved quality factor (*Q*-factor), sensing resolution, and sensitivity in response to the sensor's reactance or resistance variation.

Chapter 4, here I propose and experimentally demonstrate an ultrasensitive wireless displacement sensing technique based on the concept of parity-time (PT)-symmetry or space-time reflection symmetry, first explored in quantum physics and later extended to wave physics. This PT -symmetric telemetric sensing system comprises an active $-RLC$ tank (stationary reader) and a passive RLC tank (movable tag), which are interrogated in a wireless manner via inductive coupling. Specifically, such a non-Hermitian electronic system obeying the PT -symmetry, when operated around the exceptional point (EP), can achieve drastic frequency responses and high sensitivity, well beyond the limit of conventional fully-passive wireless displacement sensors.

Chapter 5, here I theoretically introduce and experimentally demonstrate a new class of parity-time (PT) symmetric electronic oscillators that combine EPs with another type of mathematical singularity associated with poles of complex functions. These “divergent” exceptional points (DEPs) can exhibit unprecedentedly a large eigenvalue bifurcation beyond those obtained by standard EPs. The results pave the way for building a new generation of telemetering and sensing devices with superior performance.

Chapter 6 discusses a fundamental challenge for the non-radiative wireless power transfer (WPT) resides in maintaining stable power transfer with a consistently high efficiency under dynamic conditions. In this chapter, I propose and experimentally demonstrate that a frequency-locked WPT system satisfying higher-order parity-time (PT) symmetry can achieve a near-unity power transfer efficiency that is resilient to effects of distance variation and misalignment between coils, as well as impedance fluctuations in electric grids. In specific higher-order PT electronic systems, a purely real-valued and invariant (non-bifurcated) eigenfrequency would enable the robust and efficient wireless charging, even in the weak-coupling regime (mid-range operation). I

envision that this WPT technique may provide reliable, fast and efficient power delivery for electric vehicles, consumer electronics, and medical devices.

Chapter 7, here I introduce a generalized PT (gPT)-symmetric optical structures, which have an asymmetric and unbalanced gain/loss profile, while exhibiting similar scattering properties and PT phase transitions as traditional PT-symmetric optical systems around the design frequency. Particularly, I show that the concept of gPT-symmetry may help reducing the threshold gain in achieving newly discovered PT-enabled applications, such as the coherent perfect absorber (CPA)-laser and exceptional points. The concept proposed herein will facilitate the practice of PT-symmetric optical devices by offering greater design flexibility to tailor gain-loss profiles and their thresholds.

Finally, in **chapter 8**, I conclude by briefly foregrounding some of the study impacts, and some of the directions for future research consists that stem from the project.

The proposed projects have been designed and prototypes are fabricated and measured by myself and another PhD. student Mehdi Hajizadegan under supervision of Prof. Pai-Yen Chen at the University of Illinois at Chicago (UIC).

II. GENERALIZED PARITY-TIME SYMMETRY FOR ENHANCED SENSOR TELEMETRY

Parts of this chapter have been presented in (Chen et al., 2018, Nat. Electron.) Copyright©2019, Nature.

Wireless sensors based on micromachined tuneable resonators are important in a variety of applications, ranging from medical diagnosis to industrial and environmental monitoring. The sensitivity of these devices is, however, often limited by their low quality (Q) factor. Here, I introduce the concept of isospectral parity-time-reciprocal scaling (PTX) symmetry and show that it can be used to build a new family of radio-frequency wireless microsensors exhibiting ultra-sensitive responses and ultra-high resolution, which are well beyond the limitations of conventional passive sensors. I show theoretically, and demonstrate experimentally using microelectromechanical (MEMS)-based wireless pressure sensors, that PTX -symmetric electronic systems share the same eigenfrequencies as their parity-time (PT)-symmetric counterparts, but crucially have different circuit profiles and eigenmodes. This simplifies the electronic circuit design and enables further enhancements to the extrinsic Q -factor of the sensors.

2.1 Telemetric sensing based on compact, battery-less wireless sensors

The wireless monitoring of physical, chemical and biological quantities is essential in a range of medical and industrial applications in which physical access and wired connections would introduce significant limitations. Examples include sensors that are required to operate in harsh environments, and those that are embedded, or operate in the vicinity of, human bodies [1].

Telemetric sensing based on compact, battery-less wireless sensors is one of the most feasible ways to perform contactless continuous measurements in such applications. The first compact passive wireless sensor was proposed by Collins in 1967 [2], and used a miniature spiral inductor (L) and a pressure-sensitive capacitor (C) to build a resonant sensor that could measure the fluid pressure inside the eye (an intraocular pressure sensor). The idea was based on a mechanically-adjusted capacitor (or varactor), which has been an effective way of tuning resonant circuits since the advent of the radio [3]. Despite this, wireless capacitive sensing technology has only experienced a rapid expansion in the last two decades, due to the development of microelectromechanical systems (MEMS), nanotechnology, and wireless technology [4]-[8].

Recently, low-profile wireless sensors based on passive LC oscillating circuitry (typically a series RLC tank) have been used to measure pressure [5],[6], strain [7], drug delivery [8], temperature, and chemical reactions [1]. The working principle of these passive LC sensors is typically based on detecting concomitant resonance frequency shifts, where the quantity to be measured detunes capacitive or inductive elements of the sensor. This could occur, for example, through mechanical deflections of electrodes, or variations of the dielectric constant. In general, the readout of wireless sensors relies on mutual inductive coupling (Fig. 2-1a), and the sensor information is encoded in the reflection coefficient. Such telemetric sensor systems can be modeled using a simple equivalent circuit model, in which the compact sensor is represented by a series resonant RLC tank, where the resistance R takes into account the power dissipation of the sensor (Fig. 2-1a).

Although there has been continuous progress in micro- and nanomachined sensors in recent years, the basics of telemetric readout technique remains essentially unchanged since its invention. Nonetheless, improving the detection limit is often hindered by the available levels of Q -factor,

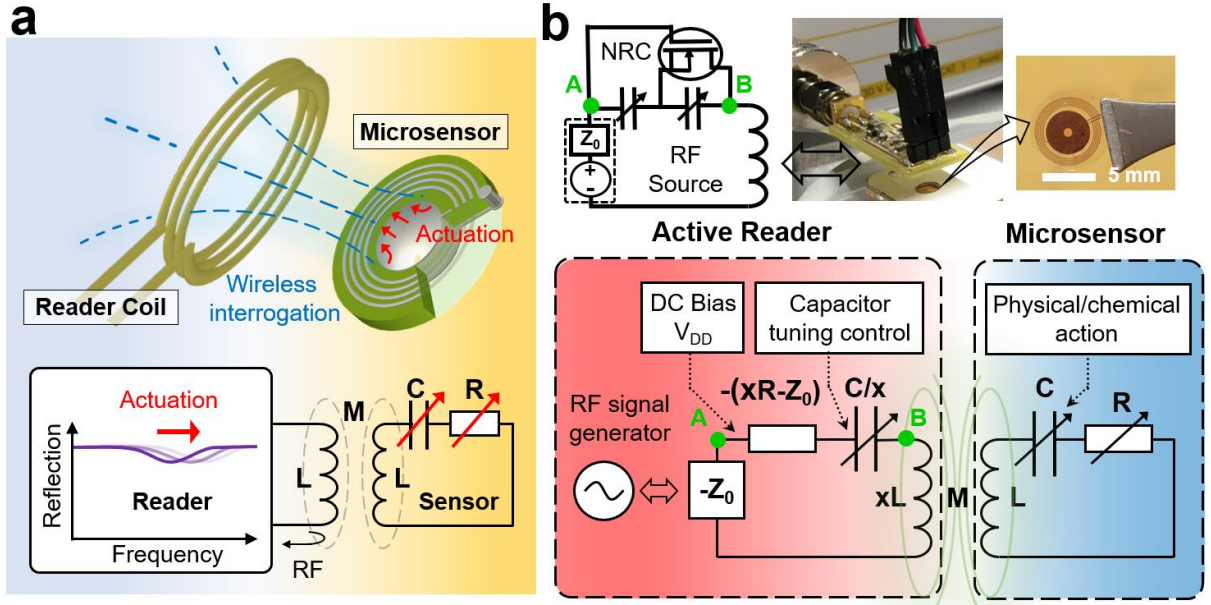


Figure 2-2 Non-Hermitian telemetric sensor system. **a** Schematics of a typical wireless implantable or wearable sensor system, where a loop antenna is used to interrogate the sensor via inductive (magnetic) coupling. The parameters to be sensed can be accessed by monitoring the reflection coefficient of the sensor, typically based on an RLC resonant circuit consisting of a micromachined varactor and inductor. **b** Equivalent circuit model for the proposed PTX-symmetric telemetric sensor system, where x is the scaling coefficient of the reciprocal-scaling operation X . If $x = 1$, the PTX system converges to the PT-symmetric case. In the close-loop normal mode analysis, an RF signal generator with a source impedance Z_0 , connected to the reader, is represented by $-Z_0$. The inset shows the AC model for the Colpitts circuit with a positive feedback, which achieves an equivalent negative resistance and an equivalent series capacitance.

the sensing resolution, and the sensitivity related to the spectral shift of resonance in response to variations of the physical property to be measured. In particular, modern *LC* microsensors based on thin-film resonators or actuators usually have a low modal *Q*-factor, due to relevant power dissipations caused by skin effects, Eddy currents, and the electrically-lossy surrounding

environment (such as biological tissues) [9]. A sharp, narrowband reflection dip has been a long-sought goal for inductive sensor telemetry, because it could lead to superior detection and great robustness to noises.

In this Article, I introduce a generalized parity-time (PT)-symmetric telemetric sensing technique, which enables new mechanisms to manipulate radio frequency (RF) interrogation between the sensor and the reader, in order to boost the effective Q -factor and sensitivity of wireless microsensors. I implement this sensing technique using MEMS-based wireless pressure sensors operating in the radio-frequency spectrum.

2.2 Theory of Generalized PT -Symmetry

The concept of PT -symmetry was first proposed by Bender in the context of quantum mechanics [10] and has been extended to classical wave systems, such as optics [11]-[13], thanks to the mathematical isomorphism between Schrodinger and Helmholtz wave equations. PT -symmetric optical structures with balanced gain and loss have unveiled several exotic properties and applications, including unidirectional scattering [14],[15], coherent perfect absorber-laser [16],[17], single-mode micro-ring laser [18]-[20], and optical non-reciprocity [21]-[24]. Inspired by optical schemes, other PT -symmetric systems in electronics (sub-radiofrequency, 30 KHz and below [25]-[27]), acoustics [28] and optomechanics [29],[30] have also been recently reported. The exceptional points (EPs) arising in these systems, found at the bifurcations of eigenfrequencies near the PT -phase transition, show potential to enhance the sensitivity of photonic sensors [31]-[35].

In principle, exceptional points and bifurcation properties of a PT -symmetric system can be utilized also to enhance sensor telemetry, represented by the equivalent circuit in Fig. 2-1b with x

$= 1$. In this case, the PT -symmetry condition is achieved when the gain and loss parameters, namely R and $-R$, are delicately balanced, and the reactive components, L and C , satisfy mirror symmetry: that is, the impedance of active and passive circuit tanks, multiplied by i , are complex conjugate of each other at the frequency of interest. Similar to earlier experiments in optical systems [22], the realization of PT -symmetry in a telemetric sensor system is expected to exhibit real eigenfrequencies in the exact symmetry phase. This leads to sharp and deep resonances, beyond the limitations discussed above for passive systems, thus providing improved spectral resolution and modulation depth for sensing. Despite this advantage of traditional PT -symmetric systems, practical implementations for the sensor telemetry may encounter difficulties in achieving an exact conjugate impedance profile. For instance, given the limited area of medical bioimplants and MEMS-based sensors, the inductance of the sensor's microcoil L_S is usually smaller than the one of the reader's coil L_R . Although downscaling the reader coil can match L_R to L_S , this would reduce the mutually inductive coupling and degrade the operation of the wireless sensor. Therefore, it is highly desirable to have extra degrees of freedom that allows arbitrarily scaling of the coil inductance and other parameters (for example, capacitance and equivalent negative resistance) in the reader, in order to optimize the wireless interrogation and facilitate the electronic circuit integration.

To overcome these difficulties, and at the same time significantly improve the sensing capabilities of telemetric sensors, I also introduce here the idea of PTX -symmetric telemetry (Fig. 2-1b). This PTX -symmetric electronic system consists of an active reader (equivalently, a $-RLC$ tank), wirelessly interrogating a passive microsensor (RLC tank) via the inductive coupling. Here, the equivalent series $-R$ is achieved with a Colpitts-type circuit (Fig. 2-1b), which acts as a negative resistance converter (see section 2-6 for detailed design, analysis and characterization of the circuit).

By suitably scaling the values of $-R$, L and C in the active reader, the system can be made invariant under the combined parity transformation $\mathcal{P} (q_1 \leftrightarrow q_2)$, time-reversal transformation $\mathcal{T} (t \rightarrow -t)$, and reciprocal scaling $\mathcal{X} (q_1 \rightarrow x^{1/2} q_1, q_2 \rightarrow x^{-1/2} q_2)$, where q_1 (q_2) corresponds to the charge stored in the capacitor in the $-RLC$ (RLC) tank, and x is the reciprocal-scaling coefficient, an arbitrary positive real number. In the following analysis, I will prove that the introduced \mathcal{X} transformation allows operating a system with unequal gain and loss coefficients (also an asymmetric reactance distribution), while exhibiting an eigenspectrum that is identical to the one of the PT -symmetric system. Crucially, the scaling operation \mathcal{X} offers an additional degree of freedom in sensor and reader designs, overcoming the mentioned space limitations of microsensors that pose challenges in realizing PT -symmetric telemetry. Even more importantly, while the scaling provided by the \mathcal{X} operator leaves the eigenspectrum unchanged, it leads to linewidth sharpening and thus boosts the extrinsic Q -factor, the sensing resolution, and the overall sensitivity.

As I demonstrate below, the effective Hamiltonian of PTX and PT systems are related by a mathematical similarity transformation. I start by considering Kirchoff's law of the equivalent circuit representation of the PTX telemetric sensor system (Fig. 2-1b) casted in the form of Liouville-type equation $\partial_\tau \Psi = \mathcal{L} \Psi$ [25] governing the dynamics of this coupled $RLC/-RLC$ dimer, where the Liouvillian \mathcal{L} is given by

$$\mathcal{L} = \begin{pmatrix} 0 & 0 & 1 & 0 \\ 0 & 0 & 0 & 1 \\ -\frac{1}{1-\kappa^2} & \frac{1}{\sqrt{x}} \frac{\kappa}{1-\kappa^2} & \frac{1}{\gamma(1-\kappa^2)} & \frac{1}{\sqrt{x}} \frac{\kappa}{\gamma(1-\kappa^2)} \\ \sqrt{x} \frac{\kappa}{1-\kappa^2} & -\frac{1}{1-\kappa^2} & -\sqrt{x} \frac{\kappa}{\gamma(1-\kappa^2)} & -\frac{1}{\gamma(1-\kappa^2)} \end{pmatrix}, \quad (2-1)$$

and $\Psi \equiv (q_1, q_2, \dot{q}_1, \dot{q}_2)^T$, $\tau \equiv \omega_0 t$, the natural frequency of an isolated lossless LC tank $\omega_0 = 1/\sqrt{LC}$, the coupling strength between the active and passive tanks $\kappa = M / \sqrt{L_R L_S}$, $L_R = xL$, $L_S = L$, and the dimensionless non-Hermiticity parameter $\gamma = R^{-1}\sqrt{L/C} = (x/R)^{-1}\sqrt{(xL)/(C/x)}$; here all frequencies are measured in units of ω_0 . The active and passive tanks have the same non-Hermiticity parameter γ , regardless of the value of x (PT or PTX system). From Eq. 2-1, I can define an effective Hamiltonian $H = i\mathcal{L}$ with non-Hermitian form (i.e., $H^\dagger \neq H$). Such non-Hermitian Hamiltonian system is invariant under a combined \mathcal{PTX} transformation, with

$$\mathcal{P} = \begin{pmatrix} \sigma_x & 0 \\ 0 & \sigma_x \end{pmatrix}, \quad (2-2a)$$

$$\mathcal{T} = \begin{pmatrix} \mathbf{1} & 0 \\ 0 & -\mathbf{1} \end{pmatrix} \mathcal{K}, \quad (2-2b)$$

$$\mathcal{X} = \mathbf{1} \otimes x_0 \text{ and } x_0 = \begin{pmatrix} x^{1/2} & 0 \\ 0 & x^{-1/2} \end{pmatrix}, \quad (2-2c)$$

where σ_x is the Pauli matrix, $\mathbf{1}$ is the identity matrix, \mathcal{K} performs the operation of complex conjugation, and $(\mathcal{PTX})^2 = \mathbf{1}$. The Hamiltonian and eigenmodes of the PTX system are related to

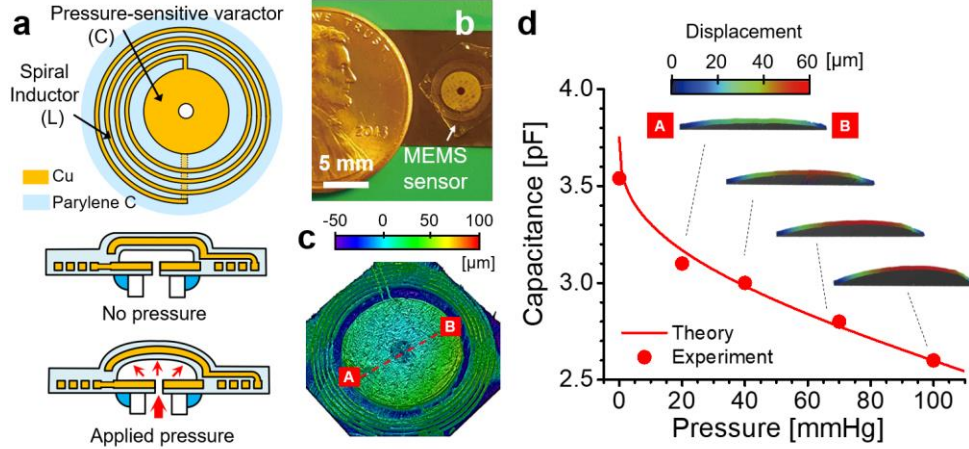


Figure 2-2 MEMS-based wireless pressure sensor. **a** Schematics of a MEMS-based pressure sensor, which consists of a variable parallel-plate capacitor c connected in series with a microcoil inductor (L), effectively forming a resonant LC tank circuit. Increasing the internal pressure by an air compressor regulator increases the displacement of the upper membrane electrode, thereby reducing the capacitance of the MEMS varactor. **b** Top view of the microfabricated wireless pressure sensor on a flexible polymer substrate. **c** Three-dimensional surface profile of the sensor in **b**, which was measured by scanning white light interferometry (SWLI). **d** Measurement (dots) and theoretical (solid line) results for the total capacitance in response to pressure (); insets show the displacement of the upper membrane electrode measured by SWLI. Due to the cylindrical symmetry of the capacitor, only displacements in the radial direction (from point A to point B in **c**) are shown.

those of the PT system (H', Ψ') through the similarity transformation $H = S^{-1}H' S$ and

$\Psi = S^{-1}\Psi'$, where S is an invertible 4-by-4 matrix $S = \mathbf{1} \otimes \zeta$ and $\zeta = \begin{pmatrix} x^{1/2} & 0 \\ 0 & 1 \end{pmatrix}$. As a result,

PTX and PT systems share the same eigenfrequencies, but possess different eigenmodes.

Moreover, H commutes with the transformed operators $\tilde{\mathcal{P}} = S^{-1}\mathcal{P}S$ and $\tilde{\mathcal{T}} = S^{-1}\mathcal{T}S = \mathcal{T}$, i.e.

$[\tilde{\mathcal{PT}}, H] = 0$, where $\tilde{\mathcal{P}}$ performs the combined operations of parity and reciprocal scaling:

$x^{1/2}q_1 \leftrightarrow x^{-1/2}q_2$. After some mathematical manipulations, I obtain $\tilde{\mathcal{PT}} = \mathcal{PTX}$, and, therefore,

H commutes also with \mathcal{PTX} (i.e. $[\mathcal{PTX}, H] = 0$). In the limit when the scaling coefficient $x = 1$, the \mathcal{PTX} -symmetric system converges into the traditional PT -symmetric system. Hence, the \mathcal{PTX} -symmetry can be regarded as a generalized group of the PT -symmetry.

2.3 Experimental demonstration of PT/\mathcal{PTX} -symmetric telemetric microsensor systems

I designed and realized the sensor using a micromachined parallel-plate varactor connected in series to a micromachined planar spiral inductor and also a parasitic resistance (Fig. 2-1b). Figures 2a-2c show the schematics and photograph of the realized device, together with its detailed surface profiles characterized by the scanning white-light interferometry (SWLI) (see Section 2-6 and 2-7 for design and fabrication details). The sensor was encapsulated with epoxy polyamides and connected to an air compressor, and a microprocessor-controlled regulator was used to vary the internal pressure inside the MEMS microcavity from 0 mmHg to 200 mmHg. This procedure simulates, for instance, pressure variations inside the human eye [6] (see Method for the detailed measurement setup). The sensor can be seen as a tunable passive RLC tank, in which the applied pressure mechanically deforms the floating electrode of the varactor (Fig. 2-2a), causing a change in the total capacitance. Figure 2-2d presents the extracted capacitance as a function of the internal pressure, with insets showing the corresponding cross-sectional SWLI images (see section 2-4 for the extraction of RLC values). The measurement results agree well with theoretical predictions, revealing that the capacitance is reduced by increasing the applied pressure.

In our first set of experiments, I designed an active reader, which, together with the passive microsensor, form the PT -symmetric dimer circuit. I investigate the evolution of complex

eigenfrequencies and reflection spectra as I vary γ and κ . In our measurements, the reader was fixed on a XYZ-linear-translation stage used to precisely control κ . For a specific value of κ , γ was tuned by the equivalent capacitance of the microsensor, responsible for the applied pressure. On the reader side, the voltage-controlled impedance converter provides an equivalent negative resistance, whose magnitude is set equal to $-(R - Z_0)$, where the sensor's effective resistance R was measured to be $\sim 150 \Omega$ and Z_0 is the source impedance of the RF signal generator (e.g., vector network analyzer used in the experiment, with $Z_0 = 50 \Omega$) connected in series to the active reader. I note that, in the closed-loop analysis, an external RF source can be modeled as a negative resistance $-Z_0$, as it supplies energy to the system [3]. When the sensor's capacitance changed, the voltage-controlled varactor in the reader circuit was adjusted accordingly to maintain the PT -symmetry condition (see section 2-5 for details of reader design). Wireless pressure sensing was performed by monitoring *in situ* the shift of resonance in the reflection spectrum across 100-350 MHz. In our measurements, a clear eigenfrequency bifurcation with respect to γ and κ of the PT -symmetric system was observed, as shown in Fig. 2-3a, and the agreement between experimental results (dots) and theory (colored contours) is excellent; a detailed theoretical analysis of the critical points is provided in the Methods. At the exceptional point γ_{EP} , real eigenfrequencies branch out into the complex plane. In the region of interest $\gamma \in [\gamma_{EP}, \infty]$, the eigenfrequencies are purely real ($\omega \in \mathbb{R}$) (Fig. 2-3a) and $\mathcal{PT}\Psi' = \Psi'$, such that the PT -symmetry condition is exactly met in the so-called exact PT -symmetric phase. In this phase, the oscillation occurs at two distinct eigenfrequencies corresponding to sharp reflection dips (Fig. 2-3b). Before passing γ_{EP} , the system is in its broken PT -symmetric phase, where complex eigenfrequencies ($\omega \in \mathbb{C}$) exist in the

form of complex conjugate pairs, and the PT -symmetry of eigenmodes is broken, namely $\mathcal{PT}\Psi' \neq \Psi'$.

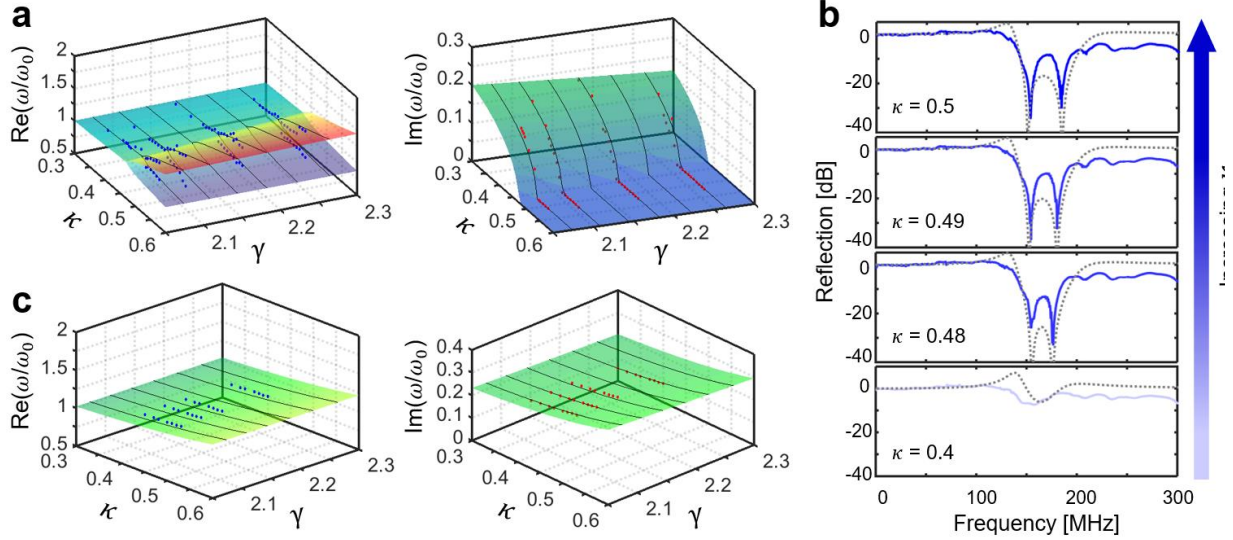


Figure 2-3 Evolution of eigenfrequencies and reflection spectra as a function of the non-Hermiticity parameter γ and coupling strength κ . (a,b) Real (left) and imaginary (right) eigenfrequency isosurface normalized by ω_0 in the (γ, κ) parameter space for **a** PT -symmetric wireless pressure sensor and **b** conventional passive wireless pressure sensor, where an active reader and a passive loop-antenna are respectively used to interrogate the micromachined sensor in **Figure 2-1**. **c** Reflection spectra against the frequency for the PT -symmetric wireless pressure sensor with different coupling strengths, showing a transition from the broken PT -symmetric phase ($\kappa = 0.4$) to the exact PT -symmetric phase ($\kappa = 0.48, 0.49$ and 0.5) when κ increases; here $\gamma = 2.26$, corresponding to applied pressure of 100 mmHg, and $\omega_0 / 2\pi = 180$ MHz. Frequencies and linewidths of reflection dips in **c** are consistent with the eigenfrequency evolution in **a**. Solid and dashed lines denote experimental data and theoretical results obtained from the equivalent circuit model in **Figure 2-1**.

The system exhibits a phase transition when the non-Hermiticity parameter exceeds the critical value γ_{EP} , at which point the non-Hermitian degeneracy can unveil several counterintuitive features, such as the unidirectional reflectionless transparency [14],[28] and the singularity-enhanced sensing [31]-[35]. To better illustrate the system response, I plot the measured reflection spectra, where γ is fixed to 2.26 (corresponding to an applied pressure of 100 mmHg), while κ is continuously varied from 0.4 to 0.5 (Fig. 2-3b). The evolution of the resonant response clearly identifies the eigenfrequency transition (Fig. 2-3a). In the weak coupling region, the system operates in the broken PT -symmetric phase, quantified by $\kappa < \kappa_{PT}$, and its complex eigenfrequency results in a weak and broad resonance. This can be explained by the fact that, if the coupling strength is weak, the energy in the active $-RLC$ tank cannot flow fast enough into the passive RLC tank to compensate for the absorption, thereby resulting in a non-equilibrium system with complex eigenfrequencies. If the coupling strength exceeds a certain threshold, the system can reach equilibrium, since the energy in the active tank can flow fast enough into the passive one to compensate its power dissipation. From Fig. 2-3a, I observe that at higher κ , the threshold of γ for the phase transition (γ_{EP}) can be reduced. As a result, a PT -symmetric telemetric sensor system, if designed properly to work in the exact PT -symmetric phase quantified by $\kappa > \kappa_{PT}$, can exhibit sharp and deep resonant reflection dips, ensuring high sensitivity with electrical noise immunity. From the circuit viewpoint, the reflectionless property in the one-port measurement is due to impedance matching. In the exact PT -symmetric phase with real eigenfrequencies, the input impedance looking into the active reader can be matched to the generator impedance Z_0 at the eigenfrequencies (or resonance frequencies), leading to the dips observed in the reflection spectrum.

We also note that the splitting of the Riemann surface outlined in Fig. 2-3a may lead to an interesting topological response, implying a dramatic shift of the resonance frequency when γ is altered by pressure-induced capacitance changes in the microsensor ($\gamma \propto C^{-1/2}$). It is interesting to compare these results with those obtained with a conventional fully-passive telemetric sensing scheme (Fig. 2-3c) [4]-[9], where the negative resistance converter and varactors are removed from the active reader, leaving a coil antenna to interrogate the same pressure sensor. In this case, the eigenfrequency of the conventional passive system is always complex (Fig. 2-3c), no matter how γ and κ are varied, as expected for a lossy resonator, and the eigenfrequency surface is rather flat for both real and imaginary parts when compared with the *PT*-symmetric system (Fig. 2-3a). Figures 4a and 4b present the evolution of the reflection spectra for the two sensing systems; here κ is fixed to 0.5 and γ is varied by changing the applied pressure (20, 40, 70, and 100 mmHg). The bifurcation of eigenfrequency in the *PT*-symmetric system (Fig. 2-4b) leads to the formation of two eigenmodes with sharp reflection dips, whose spectral shifts in response to γ can be dramatic and coincides with the topological phase transition shown in Fig. 2-3a. On the other hand, the passive system (Fig. 2-4a) exhibits a broad resonance, associated with a low sensing resolution, and a less observable change in the resonance frequency. It is evident that a *PT*-symmetric telemetric sensor can provide largely superior sensitivity when compared with conventional passive ones [4]-[9], as it achieves not only a finer spectral resolution in light of a higher *Q*-factor, but also more sensitive frequency responses (Fig. 2-5a).

Next, I explore the functionality of the *PTX*-symmetric sensor within the same telemetry platform. Unlike the *PT*-symmetric system, the reciprocal scaling in the *PTX* system breaks the mirror symmetry of the effective $|\pm R|$, L , and C , namely their values in the sensor and the reader can be quite different for large or small values of x . In our experiments, the same MEMS-based pressure sensor was now paired with a new type of reader (Fig. 2-1b), whose equivalent circuit is similar to the reader in Fig. 2-4b, but with all elements scaled following the rule: $-R \rightarrow -xR$, $L \rightarrow xL$, and $C \rightarrow x^{-1}C$. This realizes a *PTX*-symmetric telemetry system that has a non-Hermitian Hamiltonian H (Eq. 2- 1) commuting with PTX (Eq. 2- 2). I have tested different values of x to investigate its effect on eigenfrequencies; here κ was fixed to 0.5 in different setups.

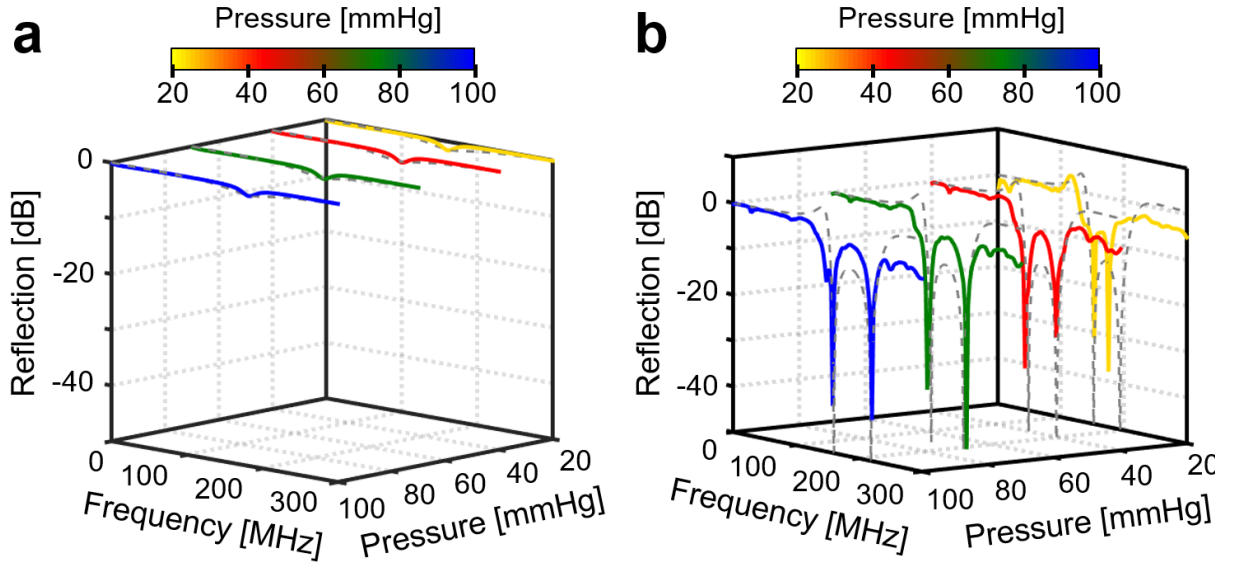


Figure 2-4 Pressure-induced spectral changes for conventional and PT-symmetric telemetric sensors. (a,b) Magnitude of reflection coefficient for the MEMS-based pressure sensor interrogated by **a** the conventional passive loop antenna and **b** the active reader realizing a PT-symmetric dimer, under different applied pressures. Solid and dashed lines denote experimental data and theoretical results obtained from the equivalent circuit models.

Figure 2-5a shows the real and imaginary parts of eigenfrequencies against γ for PTX -symmetric telemetric sensor systems with $x = 3, 1/3$, and 1. I note that $x = 1$ corresponds to the PT -symmetric system discussed before.

We observe that a non-Hermitian PTX -symmetric Hamiltonian also supports real eigenfrequencies in the exact PTX -symmetric phase, thus leading to sharp and deep resonant reflection dips. As discussed earlier, in spite of the introduction of the \mathcal{X} operator, the PTX -symmetric system and its PT -symmetric counterpart possess exactly the same eigenspectrum and bifurcation points, as clearly seen in Fig. 2-5a. In the PTX system, there is also a clear transition between the exact PTX -symmetric phase ($\mathcal{PTX}\Psi = \Psi$) and the broken PTX -symmetric phase (

$\mathcal{PTX}\Psi \neq \Psi$), which are respectively characterized by real and complex eigenfrequencies. Theoretical and experimental results in Fig. 2-5a imply that the spectral shift of resonance associated with the exceptional-point singularity in a PT -symmetric sensor can be likewise obtained in a PTX -symmetric sensor, as the same eigenspectrum is shared. I note that the PT and PTX systems, although sharing the same eigenspectrum, can have different eigenmodes, i.e., $\Psi = S^{-1}\Psi'$ and S is correlated with x . Figures 5b presents reflection spectra for the PTX -symmetric telemetric sensor with $x = 3$, under different applied pressures. Due to the scaling operation \mathcal{X} in the PTX -symmetric system, it is possible to further reduce the linewidth of the reflection dip and achieve a finer sensing resolution by increasing the value of x . In contrast to the case $x > 1$, $x < 1$ results in broadening of the resonance linewidth and thus a lowered Q -factor. I note that the input impedance (looking into the active reader) of PT - and PTX -symmetric telemetry systems can be identical and matched to the generator impedance Z_0 at their shared resonance frequencies, corresponding to reflectionless points (see section 2-6). As the frequency is away from the resonance frequency, the input impedance and reflection coefficient of PT - and PTX -

symmetric systems may be very different, leading to a different resonance linewidth as a function of x . As a result, the *PTX*-symmetric telemetric sensor system (Figs. 5b), when compared with the *PT*-symmetric one (Fig. 2-4b), not only offers more design flexibility by removing certain physical constraints (e.g., mirror-symmetric $|\pm R|$, L and C in the mutually coupled circuit), but also could support greater resolution, sensitivity, and potentially longer interrogation distance enabled by the optimally-designed self and mutual inductances of coils. Most importantly, both systems exhibit the same eigenspectrum and exceptional point. Ideally, in the exact *PTX*-symmetry phase there is no fundamental limit to the Q -factor enhancement. In the extreme case when x approaches infinity, the resonance linewidth becomes infinitesimally narrow, namely the Q -factor is close to infinity, provided that such a reader circuit can be realized. However, in reality, the $-R$, L and C values of electronic devices have their own limits.

For generality, a microsensor (negative resistance converter) can in principle be decomposed into a series or parallel equivalent *RLC* ($-RLC$) tank, and either choice is formally arbitrary, depending on sensor and circuit architectures and on the kind of excitation (i.e., impressed voltage or current source). The *concept of PTX-symmetry can also be generalized to an electronic dimer utilizing the parallel circuit configuration, whose PT-symmetric counterpart has been demonstrated in [25],[26]. It may also be possible to enhance the performance and resolution of a wireless resonant sensor modeled by a parallel RLC tank if the sensor is interrogated by a parallel $-RLC$ tank [25],[26], in order to satisfy the PTX-symmetry condition (see section 2-9 for an example of the PTX-symmetric parallel circuit).*

It is important to note that, in the exact symmetry phase of the *PTX*-symmetric system, although the gain and loss parameters ($-xR$ and R) are not equal, the net power gained in the active tank and the one dissipated in the passive tank are balanced, similar to the *PT*-symmetric case. In

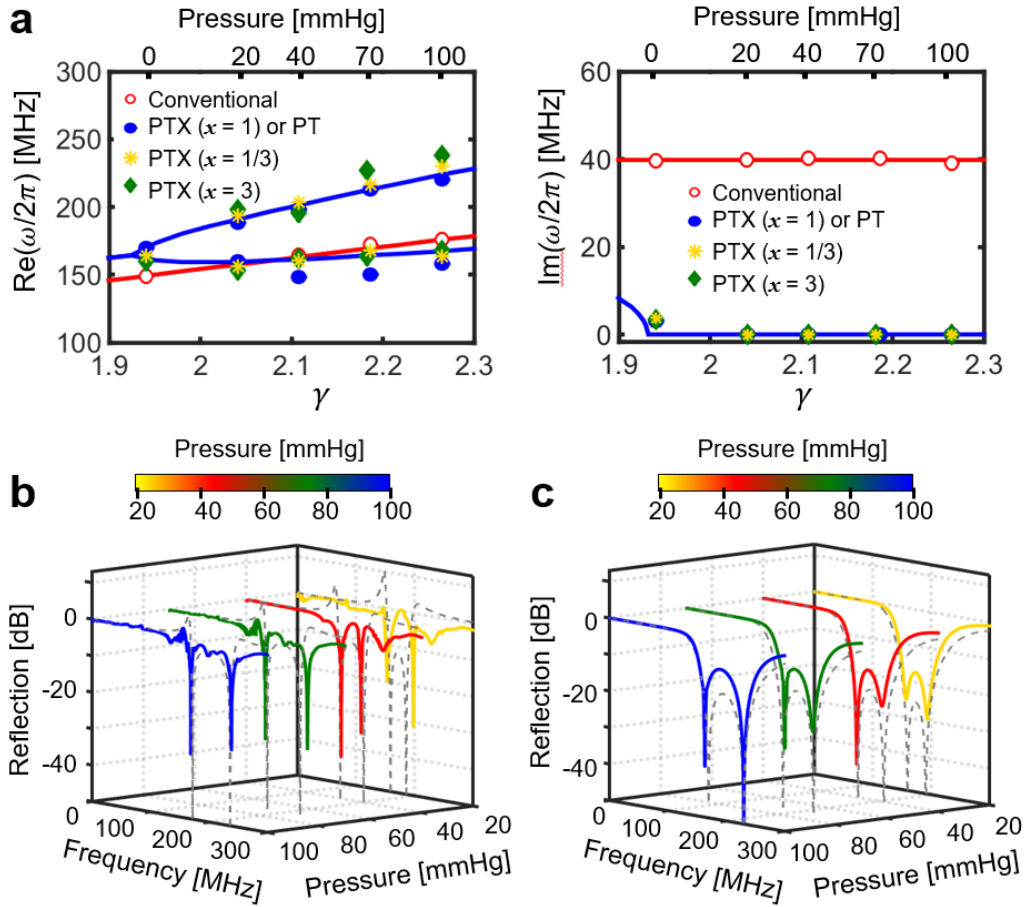


Figure 2-5 Evolution of the eigenfrequencies and reflection spectra for PTX-symmetric telemetric sensors. a Real (left) and imaginary (right) eigenfrequency as a function of the non-Hermiticity parameter γ for the fully-passive (red hollow circle; Figure 7a), PT-symmetric (blue dot), and PTX-symmetric (green and yellow dots; b and c) telemetric pressure sensors. Solid lines denote theoretical predictions (see Method). (b,c) Magnitude of the reflection coefficient for the PTX-symmetric telemetric sensor systems; here scaling coefficients x used in b and c are 3 and 1/3. Solid and dashed lines in b and c denote the experimental data and theoretical predictions

the closed-loop analysis, the power loss in the passive tank $P_{loss} = |\dot{q}_2|^2 R / 2$, while the power gained in the active tank $P_{gain} = |\dot{q}_1|^2 (xR - Z_0) / 2 + |\dot{q}_1|^2 Z_0 / 2$ (where the first term accounts for power gained from the negative-resistance device and the second term corresponds to the external

energy source modeled as a negative resistance $-Z_0$). Since the *PTX*-symmetry enforces the condition $\dot{q}_1 = \dot{q}_2 / \sqrt{x}$ (see Eq. 2- 5), gain and dissipation are always balanced in this system (i.e., $P_{\text{gain}} = P_{\text{loss}}$), regardless of the value of x . Therefore, although this generalized *PT*-symmetric system allows for arbitrary scaling of the gain and loss parameters (R and $-R$ here), the gain-loss power balance is maintained in the exact symmetry condition, as expected by the fact that the eigenvalues are real. However, greater design flexibility on the linewidth of the response could be enabled.

Finally, it is interesting to note that in the *PTX*-symmetric system, if x is sufficiently small such that $xR - Z_0 \leq 0$, both reader and sensor circuits can be fully passive, namely an inductively-coupled *RLC/RLC* dimer is used. Such observation is in stark contrast with what one would expect in conventional *PT*-symmetric systems, where pertinent gain or amplification are necessary to enable the associated peculiar phenomena. Figure 2-5c presents reflection spectra for the *PTX*-symmetric telemetric sensor system with $x = 1/3$; in this case, the reader is also a passive *RLC* tank without the need of a negative-resistance or amplification device. I observe a broad resonance, as the linewidth of reflection dip is widened by decreasing the value of x . This operating regime ($x = 1/3$), although not necessarily of interest for enhanced sensing capabilities, provides an interesting platform to study the dynamics of exceptional points and non-Hermitian physics in a loss-loss dimer, without the need of any active component. The presented *PTX*-symmetric dimer structure may also be extended to other frequencies, including light and ultrasonic waves. For instance, one potential application of our proposed reciprocally-scaling operation is to provide an additional knob to tailor the threshold gain of *PT*-symmetric single-mode lasers [18]-[20] or coherent perfect absorber-lasers [16],[17] by breaking the exact balance of gain and loss coefficients, while preserving the spectrum of eigenvalues.

2.4 Methods

Exceptional point and phase transitions

Applying Kirchhoff's laws to the *PTX*-symmetric circuit in Fig. 2-1b leads to the following set of equations:

$$\frac{d^2 q_1}{d\tau^2} = -\frac{1}{1-\kappa^2} q_1 + \frac{1}{\sqrt{x}} \frac{\kappa}{1-\kappa^2} q_2 + \frac{1}{\gamma(1-\kappa^2)} \dot{q}_1 + \frac{1}{\sqrt{x}} \frac{\kappa}{\gamma(1-\kappa^2)} \dot{q}_2, \quad (2-3a)$$

$$\frac{d^2 q_2}{d\tau^2} = \sqrt{x} \frac{\kappa}{1-\kappa^2} q_1 - \frac{1}{1-\kappa^2} q_2 - \sqrt{x} \frac{\kappa}{\gamma(1-\kappa^2)} \dot{q}_1 - \frac{1}{\gamma(1-\kappa^2)} \dot{q}_2, \quad (2-3b)$$

which leads to the Liouvillian formalism in Eq. 2-2 . After the substitution of time-harmonic charge distributions $q_n = A_n e^{i\omega\tau}$, eigenfrequencies and normal modes for this *PTX*-symmetric electronic circuit can be computed from the eigenvalue equation $(H_{eff} - \omega_k \mathbf{I}) \Psi_k = 0$, with $k = 1, 2, 3, 4$. The eigenfrequencies associated to the non-Hermiticity parameter γ and coupling strength κ can be derived as:

$$\omega_{1,2,3,4} = \pm \omega_0 \sqrt{\frac{2\gamma^2 - 1 \pm \sqrt{1 - 4\gamma^2 + 4\gamma^4 \kappa^2}}{2\gamma^2 (1 - \kappa^2)}}, \quad (2-4)$$

There is a redundancy in Eq. 2-4 because positive and negative eigenfrequencies of equal magnitude are essentially identical. Equation (4) is also valid for the *PT*-symmetric system, as eigenfrequencies in Eq. 2-4 is found to be independent of x . I note that if $x = 1$, the *PTX*-symmetric system would degenerate into the *PT* one. The eigenmodes of the *PT*-symmetric system (Ψ'_k) and the *PTX*-symmetric system (Ψ_k) can be written as:

$$\Psi'_k = c_k \left(e^{-i\phi'_k}, e^{i\phi'_k}, -i\omega_k e^{-i\phi'_k}, -i\omega_k e^{i\phi'_k} \right)^T, \quad c_k \in \mathbb{R}; \quad (2-5a)$$

$$e^{2i\phi'_k} = -\frac{\gamma \left[(1-\kappa^2)\omega_k^2 - 1 \right] + i\omega_k}{\kappa(\gamma + i\omega_k)}; \quad (2-5b)$$

$$\Psi_k = S^{-1} \Psi'_k. \quad (2-5c)$$

Complex eigenfrequencies would evolve with γ , unveiling three distinct regimes of behavior (Fig. 2-3a). The eigenfrequencies undergo a bifurcation process and branch out into the complex plane at the exceptional point (or spontaneous *PTX*-symmetry breaking point):

$$\gamma_{EP} = \frac{1}{\kappa} \sqrt{\frac{1 + \sqrt{1 - \kappa^2}}{2}}. \quad (2-6)$$

In the parametric region of interest $\gamma \in [\gamma_{EP}, \infty]$, *PTX*-symmetry is exact, rendering real eigenfrequencies and $\mathcal{PTX}\Psi_k = \Psi_k$. The region $\gamma \in [\gamma_c, \gamma_{EP}]$ is known as the broken *PTX*-symmetric phase with complex eigenfrequencies. Another crossing between the pairs of degenerate frequencies (and another branching) occurs at the lower critical point:

$$\gamma_c = \frac{1}{\kappa} \sqrt{\frac{1 - \sqrt{1 - \kappa^2}}{2}}. \quad (2-7)$$

In the sub-critical region $\gamma \in [0, \gamma_c]$, ω_k become purely imaginary and, therefore, the modes have no oscillatory part and simply blow up or decay away exponentially. These modes correspond to the overdamped modes of a single oscillator, which is of little interest, particularly for sensor applications that require sharp resonances.

Wireless measurement setups

Our experimental setup comprised a MEMS-based wireless pressure sensor, inductively coupled to a conventional passive reader or an active reader (a picture of experimental setup is shown in section 2-5). The MEMS varactor is constituted by two circular parallel metal-sheets with a diameter of 4 mm and an air gap of 8 μm . To simulate variations of internal pressure inside the human eye, the sensor was encapsulated with epoxy polyamides and connected with an air compressor. A microprocessor-controlled regulator (SMC E/P Regulator) was used to control the internal pressure inside the air cavity of MEMS varactor. The active reader composed of $-RLC$ tank was fixed on a XYZ linear translation stage and connected to VNA (Agilent E5061B). This allows for precise control of the coupling strength κ between the MEMS-based pressure sensor and the reader coil. The internal pressure inside the micromachined air cavity of the sensor, as the main physiological parameter of interest, was characterized by tracking the resonance frequency from the measured reflection coefficients. In our experiments, the pressure was varied from 0 mmHg to 200 mmHg, and the VNA and the pressure regulator were synchronously controlled by the LabVIEW program.

2.5 Design and Characterization of MEMS-Based Pressure Sensor

Design of MEMS-Actuated Capacitive Pressure Sensor

A typical passive pressure sensor contains an LC resonator, including a pressure-tuned parallel-plate capacitor and a planar micro-coil inductor. Such device architecture has been widely adopted for pressure sensors in many medical, industrial, automotive, defense and consumer applications [1]-[9]. Assuming no fringe effect, the capacitance is given by:

$$C = \epsilon_0 \epsilon_r \frac{A}{d}, \quad (2-8)$$

where ε_r is the relative permittivity, ε_0 is free space permittivity, A and d are the area of two capacitor electrodes and the separation distance between them (when no pressure is applied). As schematically shown in Fig. 2-2 in the main text, the MEMS varactor includes a movable upper electrode and a stationary lower electrode, which are separated by a variable air gap ($\varepsilon_r = 1$). The lower electrode is fixed to the substrate and has a small drain hole connected to the compressor through a sealed tube. Therefore, the pressure inside the encapsulated air cavity can be controlled by a pressure regulator. As the internal pressure increases, the upper electrode is gradually bent upward such that the total capacitance of the MEMS varactor is varied. The maximum displacement of the movable upper electrode Δd , as a function of pressure P and electrode's material parameters (Young's modulus E and Poisson ratio ν), can be calculated using the Euler–Bernoulli theory [5], leading to:

$$\Delta d = \frac{3Pa_0^4(1-\nu^2)}{16Et^3} \frac{1}{1 + 0.448\left(\frac{d}{t}\right)^2}, \quad (2-9)$$

where a_0 and t represent the radius and thickness of the circular metallic plates. Consider the pressure-driven displacement, the capacitance can be calculated by conducting the surface integral over the metallic disk:

$$C' = 2\pi\varepsilon_r\varepsilon_0 \int_0^{a_0} \frac{r}{d + \delta d(r)} dr, \quad (2-10)$$

where $d(r)$ is the function of deflection depending on the radial position of the membrane. Under an internal pressure, C' can be approximately expressed as a function of Δd [5]:

$$C' = C \frac{\sqrt{\frac{\Delta d}{d}}}{\tanh^{-1} \sqrt{\frac{\Delta d}{d}}}. \quad (2-11)$$

For most commonly used copper electrodes, important material parameters are: $E = 117$ GPa and $\nu = 0.33$ [10]. In our design, the two copper disks have the same radius $a_0 = 2$ mm and are initially separated by an air gap $d = 100$ μm .

Figure 2-6 shows the theoretical and measurement results for the maximum displacement of the movable upper electrode as a function of the applied pressure. The scanning white-light interferometry (SWLI) was used to determine the maximum displacement. It is seen from Fig. 2-6 that the experimental results agree with the theory quite well, confirming the validity of Eq. 2-11. As can be expected, the displacement of upper electrode increases with increasing the applied pressure, which, in turn, reduces the total capacitance.

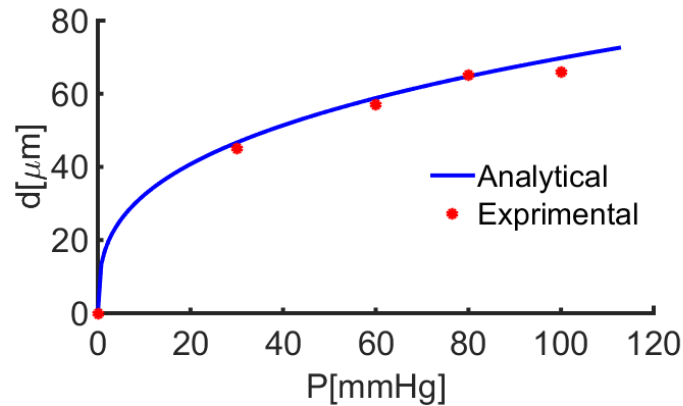


Figure 2-6: Maximum displacement of the movable electrode against applied pressure for the MEMS varactor in Fig. 2-2 of the main text.

To characterize the practical capacitance and the effective resistance of the sensor, I first used an external coil to contactlessly read the sensor, and then analyzed the reflection responses to retrieve lumped-element parameters in the equivalent circuit. In our characterizations, I first characterized an individual micro-coil (without loading the capacitor) for knowing its inductance value, as well as the mutual inductance between two tightly coupled micro-coils. Once the impedance of the micro-coil is known, the capacitance of the complete sensor as a function of applied pressure can be retrieved by fitting experiment data with the equivalent circuit model. From the complex reflection coefficient, the effective resistance of the sensor can also be retrieved, which is found to be almost invariant under different pressures ($\sim 150 \Omega$). Figure 2-7 presents theoretical and experimental values of capacitance of the MEMS varactor; here capacitance as a function of pressure was calculated using Eqs. (2-8)-(2-11). The experimental and theoretical results exhibit good agreement, despite slight differences due to fringing effects and microfabrication imperfections. It is seen from Fig. 2-7 that the sensor's capacitance decreases with increasing the applied pressure, due to the enlarged air gap Δd (Fig. 2-6).

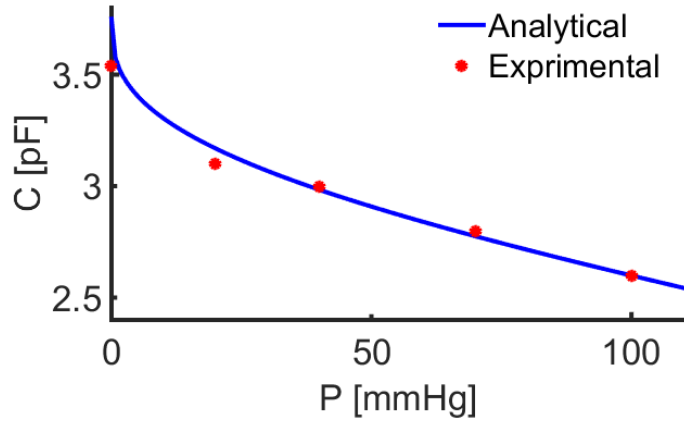


Figure 2-7. Capacitance against the applied pressure for the MEMS varactor in Fig. 2-2 of the main text.

Design of Microcoil Inductor

The self-inductance of the planar micro-coil inductor in Fig. 2-8 can be derived from the ratio between the magnetic flux and current, which has an approximate expression as [11]:

$$L = \frac{\mu_0 N^2 d_{avg}}{2} \left[\ln \left(\frac{2.46}{\phi} \right) + 0.2\phi^2 \right], \quad (2-12)$$

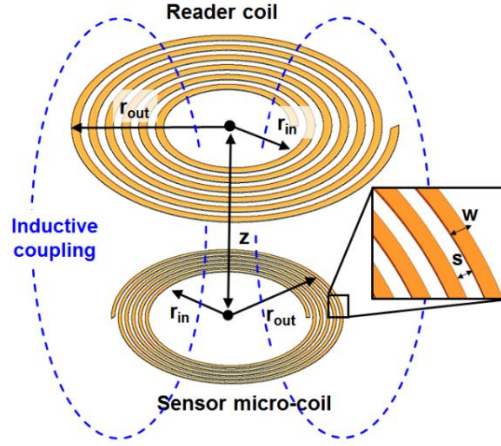


Figure 2-8. Configurations and physical parameters of planar coils used in the reader and the sensor.

where μ_0 is the free space permeability, N is number of turn, $d_{avg} = 2r_{in} + N \times (s + w)$ is the average diameter of spiral coil, $2r_{in}$ is inner diameter of spiral coil, w and s are width and spacing of the coil, and $\phi = N \times (s + w) / [d_i + N \times (s + w)]$ is the filling ratio. I have applied Eq. 2-12 to design the reader/sensor micro-coils. For example, the inductance values and important design parameters for micro-coils used in the *PT*-symmetric sensor (Fig. 2-4b) are summarized in Table 1.

	L [μH]	N	s [mm]	w [mm]	r_{in} [mm]
Sensor	0.3	5.5	0.075	0.075	2.4
Reader	0.28	6	0.25	0.25	2

Table 2-1. Physical parameters for IOP sensor and reader.

The mutual inductance for two filamentary currents i and j can be computed using the double integral Neumann formula [12]:

$$M_{ij} = \frac{\mu_0}{4\pi} \int_{C_i} \int_{C_j} \frac{1}{|R_{ij}|} d\vec{l}_i \cdot d\vec{l}_j, \quad (2-13)$$

where R_{ij} represents the distance between metallic lines, which has a relation with the radius of each coil and the central distance between them. The calculation of total mutual inductance for coils with multiple turns is possible with the summation of the separate mutual inductance of each current filament:

$$M = \rho \sum_{i=1}^{N_R} \sum_{j=1}^{N_S} M_{ij}, \quad (2-14)$$

where i (j) represents the i -th (j -th) turn of micro-coil on the reader (sensor) side, ρ is the shape factor of planar coil [12], and M_{ij} is the mutual inductance between the loops i and j , which are given by:

$$M_{ij} \approx \frac{\mu_0 \pi a_i^2 b_j^2}{2(a_i^2 + b_j^2 + z^2)^{3/2}}, \quad (2-15)$$

where z is the central distance between two micro-coils, $a_i = r_{o,R} - (N_i - 1)(w_R + s_R) - w_R / 2$, $b_j = r_{o,S} - (N_j - 1)(w_S + s_S) - w_S / 2$, N_i (N_j) represents the i -th (j -th) turn of reader (sensor) coil, r_o is the outer radius of the microcoil, and the subscript R (S) represents reader (sensor). Finally, the coupling coefficient between the reader and sensor micro-coils is given by $\kappa = M / \sqrt{L_R L_S}$, where L_R is the reader coil inductance and L_S is the sensor coil inductance. In our designs, I first characterized the self-inductance of each individual coil using the analytical formula of Eq. 2-(15), which has been confirmed with the full-wave simulation [13]. Then, the total mutual inductance between two micro-coils was calculated using the analytical formula of Eqs. (2-13)-(2-

15) and the result was confirmed by the full-wave simulations. In our designs, the coupling coefficient κ is in the range of 0 to 0.5.

2.6 Design of Negative Resistance Converter (NRC)

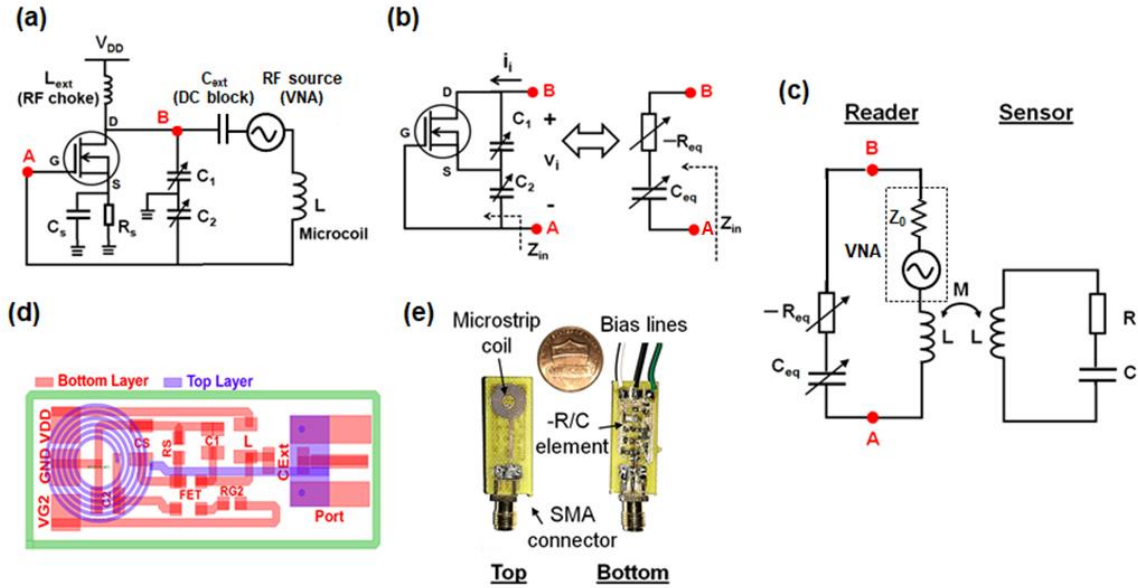


Figure 2-9. **a** Schematics of the reader circuit for the PT/PTX-symmetric telemetric sensors, consisting of a negative resistance converter (Colpitts oscillator) connected to a microcoil inductor, fed by a RF source (vector network analyzer; VNA). **b** Input impedance of an open-circuited Colpitts-type circuit $Z_{in}=v_i/i_i$, without connecting to any reactive element. The complex input impedance can be decomposed into a series combination of an equivalent negative resistance $-R_{eq}$ and an equivalent capacitance C_{eq} . **c** Equivalent circuit model for the PT/PTX-symmetric telemetric sensor system, in which the reader is a series $-RLC$ tank where $-R$ and C are contributed by the Colpitts-type oscillator. **d** Layout and **e** fabricated PCB-based active reader used in the PT-symmetric sensor.

To build the *PT*/*PTX*-symmetric electronic circuit, it requires a negative resistor ($-R$), realized using a negative resistance converter (NRC) at high frequencies. An active NRC could

pull in power to the circuit, rather than dissipating it like a passive resistor. Figure 2-9a shows the circuit diagram of our NRC, inspired by the design of Colpitts-type oscillator [14]-[21]. This NRC as an active lumped resistor may provide stable and almost non-dispersive negative resistance over a broad frequency range. The negative resistance can be a series or a parallel element, depending on how the circuit is designed, i.e., a series (parallel) circuit model is usually used for voltage-controlled negative resistance oscillators (current-controlled negative conductance oscillators) [22]. For example, in Ref. [23], a one-port op-amp inverting circuit operating at KHz frequencies, equivalent to a parallel negative resistance, was used to demonstrate a PT -symmetric system based on parallel $-RLC$ and RLC tanks. In the circuit analysis, it is common to model the Colpitts- or Hartley-type oscillator with positive feedback as a negative resistor ($-R$). One method of oscillator analysis is to determine its input impedance, neglecting any external reactive component at the input port, as shown in Fig. 2-9b. For the Colpitts circuit configuration in Fig. 2-9b, the complex input impedance ($Z_{in} = v_i/i_i$) looking into the points A and B can be derived as [14]-[21]:

$$Z_{in(AB)} = -\frac{g_m}{\omega^2 C_1 C_2} + \left(\frac{1}{i\omega C_1} + \frac{1}{i\omega C_2} \right), \quad (2-16)$$

where g_m is the transconductance of the field-effect transistor (FET); here I assume that the $g_m \gg \omega C_{gs}, \omega C_{gd}$, and C_{gs} and C_{gd} are the gate-drain capacitance and gate-source capacitances), which is approximately valid at moderately low frequencies (e.g., VHF band in this project). As a result, the input impedance looking into the points A and B is equivalent to a series $-RC$ circuit consisting of a negative resistance $-R_{eq}$ and an equivalent capacitance C_{eq} , as shown in Fig. 2-9b [1]-[6]:

$$-R_{eq} = -\frac{g_m(V_{bias})}{\omega^2 C_1 C_2} \quad \text{and} \quad C_{eq} = \frac{C_1 C_2}{C_1 + C_2}. \quad (2-17)$$

By connecting the input port to an inductor, a positive feedback oscillator can be made by controlling the open-loop and feedback gains at the resonance frequency. As known from Eq. 2-(17), the negative resistance can be increased by using larger values of transconductance and smaller values of capacitance. If the two capacitors are replaced by inductors, the circuit becomes a Hartley oscillator, whose input impedance becomes the $-RL$ combination.

According to Eqs. (2-16) and (2-17), the effective resistance is controlled by the transistor's transconductance, readily adjusted by DC offset voltages. The RF transistors used here have high cutoff frequencies up to several GHz, ensuring the minimum parasitic effects and the stability of circuit. The effective capacitance is determined by the two lumped capacitances C_1 and C_2 , which could be contributed by the voltage-controlled varactors such that the effective capacitance of the $-RLC$ tank is tunable. If a microcoil inductor is connected to the input of the Colpitts oscillator (points A and B in Figs. S4b and S4c), a series $-RLC$ tank can be realized if that the AC source is connected in series to the inductor, as can be seen in Fig. 2-9c. Figures S4d and S4e show the circuit layout and the fabricated printed circuit board (PCB) for the active reader used in *PT*-symmetric system (Fig. 2-4b), respectively. This active reader consists of the voltage-tuned NRC (Fig. 2-9a), which are connected in series to a planar coil, forming the $-RLC$ tank.

The effective impedance of the NRC can be retrieved from the measured reflection coefficient of an isolated series $-RLC$ tank connected to the vector network analyzer (VNA), by decomposing the contribution of the coil inductance. An individual $-RLC$ tank can allow the reflected RF signal to have larger amplitude than the incident one, namely the steady-state reflection gain is achieved. However, in experiments the reflection cannot be infinitely large because all transistors and electronic components have maximum operating voltage/current ranges, large-signal effects, and inherent nonlinearities. In a similar sense, although in theory a pole could

arise in a $-RLC$ tank, an ever-growing eigenmode (charge/charge flow) is never achieved due to the above-mentioned nonlinear effects in real-world electronic devices. A more detailed equivalent circuit of the Colpitts-type NRC is shown in Fig. 2-10a, which includes also a shunt inductance L_p and a parasitic capacitance C_p [22]. I note that, at sufficiently low frequencies, C_p has a high RF impedance $Z_c = i / \omega C_p$ (acting like a low-pass filter or an open circuit), while L_p has a low RF impedance $Z_l = -i\omega L_p$ (acting like a short circuit). Therefore, the parasitic effect may be minimized if the operating frequency is moderately low, well below the transistor's cutoff frequency (f_T) and maximum frequency (f_{max}). Figure 2-10a presents the experimental (solid) and simulated (dashed) reflection spectra of the Colpitts-NRC shown in Fig. 2-9, under different DC bias conditions. In our simulations, the equivalent resistive and reactive values in the circuit model, as shown in Figs. S5b and S5c, were extracted from the measured reflection coefficients by using the numerical optimization. From Fig. 2-10a, a good agreement is found between the experimental and simulation results. Here, I also present the reflection spectra for the equivalent circuit in Fig. 2-10a without the parasitic capacitance (dotted). The results show no significant difference in the frequency range of interest, when compared to those obtained from experiments and the full equivalent circuit model.

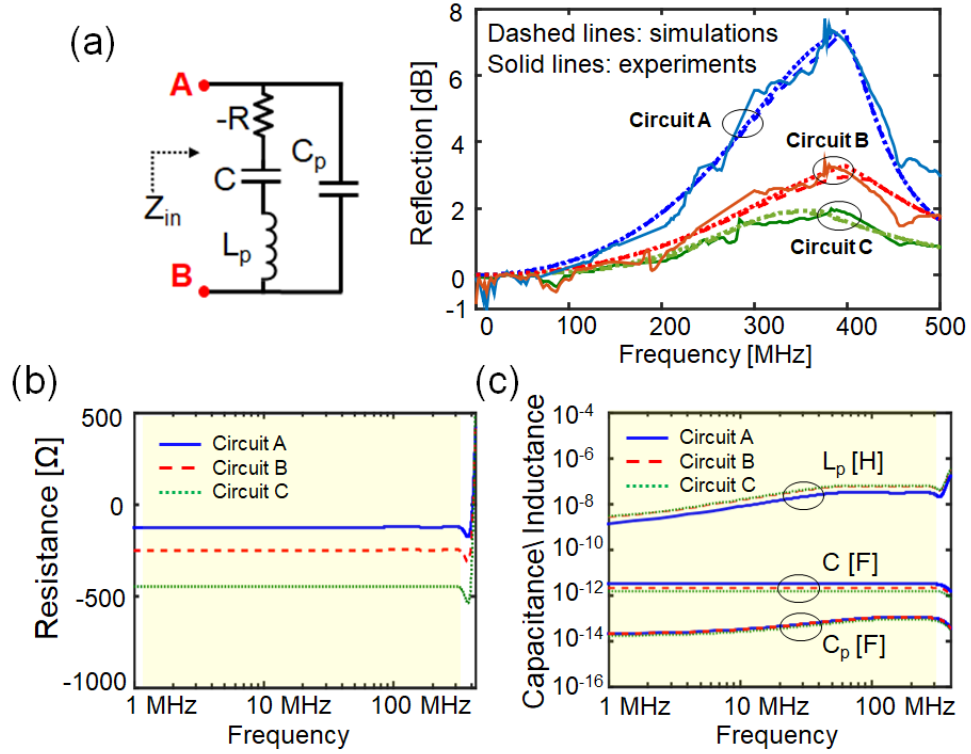


Figure 2-10 . (a) Reflection spectra of the NRC versus frequency under different biasing conditions; here, solid and dashed lines represent the experimental and simulation results, and dotted lines represent the simulation results without considering the parasitic capacitance. Equivalent (b) resistance and (c) capacitance and parasitic components for the NRC in (a). The highlighted areas show the frequency range of interest, where the values of negative resistance and capacitance are nearly constant. The effects of L_p and C_p are negligible if the operating frequency is much lower than the cutoff frequency of the transistor.

As a result, for our initial analysis, parasitic elements and device nonlinearities are ignored. In the frequency range of interest, the experimentally measured input impedance can be decomposed into a series combination of a negative resistance and a capacitance. This simplified model shows an acceptable comparison with experimental results, as can be seen in Fig. 2-10a. It is clearly seen

from Fig. 2-10b that that negative resistance can be tuned by adjusting the DC offset voltage and their values are nearly invariant at low frequencies.

2.7 Microfabrication and Characterization of the Wireless Pressure Sensor

Fabrication of Wireless Pressure Sensors by the MEMS processes

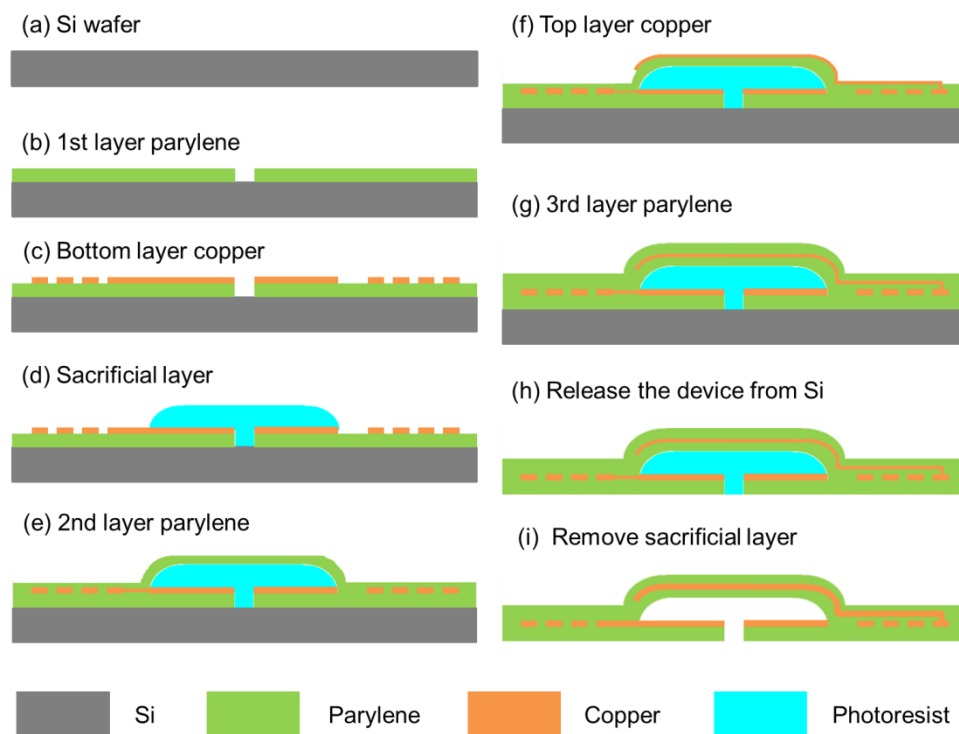


Figure 2-11. Schematics of fabrication processes for the MEMS-based IOP sensor in Fig. 2-2 in the main text.

Figure 2-11 presents the fabrication flow of the MEMS-based intraocular pressure (IOP) sensor in Fig. 2-2. In step (a), the silicon (Si) wafer was first cleaned following the standard RCA cleaning process. In step (b), an 8 μm -thick parylene layer was deposited using the thermally activated chemical vapor deposition (CVD) method in the Specialty Coating Systems (SCS PDS 2010). In this parylene layer, the sensor's backside was etched to form a pressure access hole with diameter of 0.8 mm by using the oxygen reactive ion etching (RIE, DryTech RIE 184). In step (c), a 3 μm -thick copper (Cu) film was deposited using the electron beam evaporation (Temescal Model BJD-1800 e-beam evaporator). Standard photolithography was used to pattern the copper and form the coil inductor and the capacitor pad. In steps (d)-(e), a 10 μm -thick sacrificial photoresist layer was patterned by the lithographic method, following the coating of the second parylene layer that has a thickness of 4 μm . In step (f), the second Cu layer was deposited and patterned by the lithographic method; here the top and bottom metallic structures were connected by a Cu interconnect patterned by oxygen RIE. In step (g), the third parylene with a thickness of 8 μm was coated as protection layer. After that, the device was released from Si substrate using the KOH solution. In the last step, (h), the sacrificial layer was removed in acetone solution with the critical point dryer (CPD) (Tousimis 931). Finally, the microfabricated IOP sensor was made with a flexible air cavity that can be actuated by the internal pressure, as shown in (i).

2.8 Measurement Setup for the MEMS Wireless Pressure Sensors

Figure 2-12 shows our wireless measurement setup, which comprises a MEMS-based pressure sensor, inductively coupled to a passive or active reader (interrogator). The MEMS-based pressure sensor consists of a variable capacitor (varactor) functioning as a transducer, connected in series to a planar microcoil inductor. In the equivalent circuit diagram, the pressure sensor itself stands for a RLC tank, where the applied pressure mechanically deforms the MEMS varactor and

therefore varies the sensor's natural frequency. The pressure sensor was encapsulated with epoxy polyamides and connected with an air compressor. A microprocessor-controlled regulator (SMC E/P Regulator) was used to control the internal pressure inside the air cavity of MEMS varactor. The active reader composed of $-RLC$ tank was fixed on a XYZ linear translation stage and connected to vector network analyzer (VNA: Agilent E5061B). This setup allows for precise control of the coupling strength κ between the MEMS sensor and the reader coil.

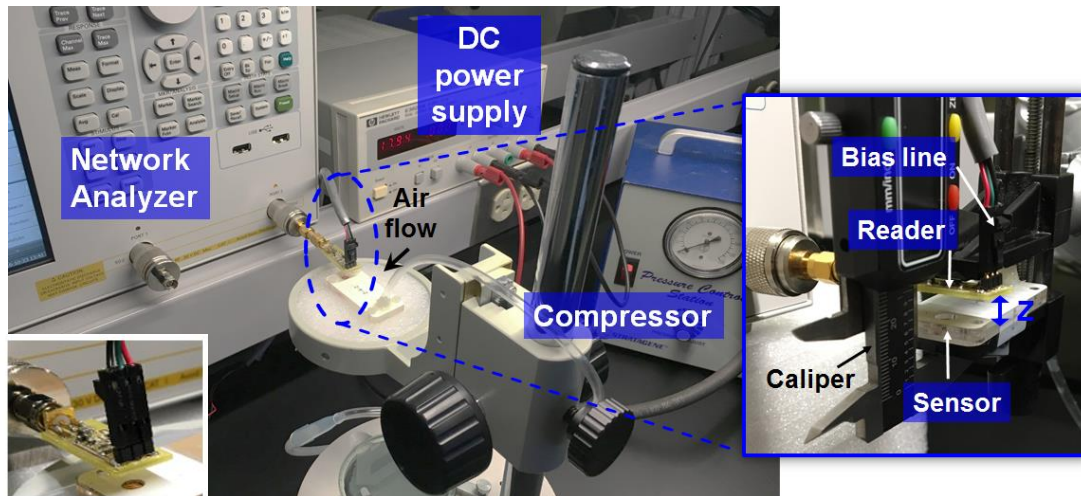


Figure 2-12. Measurement Setup for the MEMS wireless pressure sensor.

Figure 2-13 shows the theoretical and experimental results for eigenfrequency variations of the *PT*-symmetric wireless pressure sensor system, where the capacitance of the microfabricated pressure sensor is changed with respect to the pressure-induced displacement; here an equivalent resistance of $150\ \Omega$ was measured for the sensor, and the inductance of the sensor's micro-coil is about 300 nH. When the sensor's capacitance is varied (Fig. 2-7), the effective capacitance of the active reader should also be tuned accordingly to maintain the *PT*-symmetry. This can be achieved by precisely controlling the DC offset voltage of varactors in the reader circuit. To make a fair comparison, I also studied the conventional wireless pressure sensor system, where a passive external coil (the same as the one used in the active reader) was used to read the microsensor. As can be seen in Fig. 2-13, the *PT*-symmetric telemetric sensor system can provide a larger resonance frequency shift in response to pressure-driven capacitance variations. I note that a *PTX*-symmetric sensor would display the same sensitivity because the *PT* and *PTX* systems share the same eigenspectrum, as discussed in the main text.

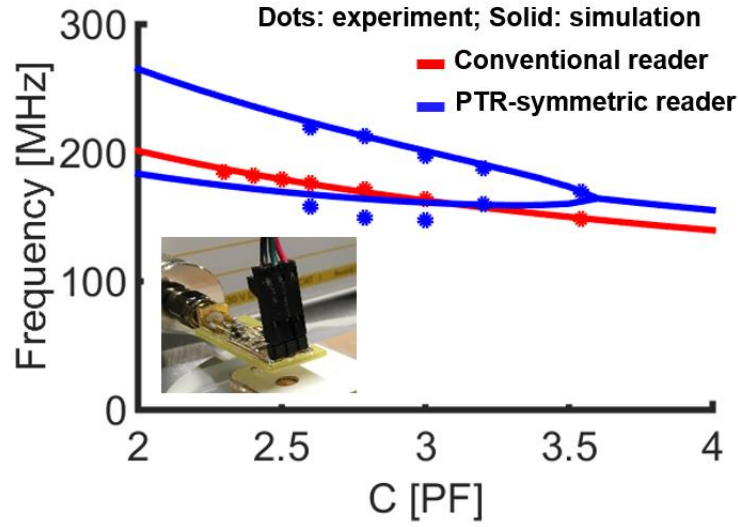


Figure 2-13. Variations of eigenfrequencies with the pressure-driven capacitance for conventional and PT-symmetric wireless pressure sensor systems. The pressure corresponding to the specific capacitance can be found in Fig. 2-7. I note that a PTX-symmetric sensor displays the same frequency response because PT and PTX systems share the same eigenspectrum.

2.9 Analysis of PTX-Symmetric Electronic Systems

PTX-Symmetric Circuits in the Parallel Configuration

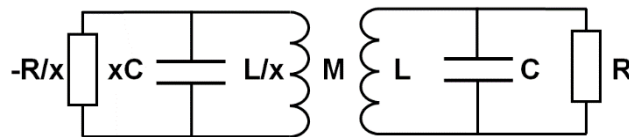


Figure 2-14. PTX-symmetric electronic system realized with the parallel-circuit configuration.

The passive LC wireless sensors are also commonly designed and modeled using an *equivalent, parallel RLC circuit (excited by an impressed current source)*. I note that the concept of *PTX-symmetry can in principle be applied to different types of series and parallel circuits, and possibly their complex combinations*. Figure 2-14 shows a PTX-symmetric circuit formed by the parallel –RLC and RLC tanks, which communicate through the inductive coupling. Such a system is invariant under the parity transformation $\mathcal{P} (q_1 \leftrightarrow q_2)$, time-reversal transformation $\mathcal{T} (t \rightarrow -t)$, and reciprocal scaling $\mathcal{X} (q_1 \rightarrow x^{1/2} q_1, q_2 \leftrightarrow x^{-1/2} q_2)$, where q_1 (q_2) corresponds to the charge stored in the capacitor in the parallel –RLC (RLC) tank. Its PT-symmetric counterpart with $x = 1$ have been experimentally demonstrated in Ref. [23], in which a shunt negative resistor was realized using the op-amp inverting circuit. According to the Kirchoff's law, the Liouvillian \mathcal{L} and the effective Hamiltonian H of the PTX-symmetric circuit in Fig. 2-11 can be derived as:

$$H = i\mathcal{L} \text{ and } \mathcal{L} = \begin{pmatrix} 0 & 0 & 1 & 0 \\ 0 & 0 & 0 & 1 \\ -\frac{1}{1-\kappa^2} & \frac{1}{\sqrt{x}} \frac{\kappa}{1-\kappa^2} & \gamma & 0 \\ \sqrt{x} \frac{\kappa}{1-\kappa^2} & -\frac{1}{1-\kappa^2} & 0 & -\gamma \end{pmatrix} \quad (2-18)$$

where $\omega_0 = 1/\sqrt{LC}$, the coupling strength between the active and passive tanks $\kappa = \sqrt{x}M/L$, the non-Hermiticity parameter $\gamma = R^{-1}\sqrt{L/C} = (|-R/x|)^{-1}\sqrt{(L/x)/(xC)}$, and all frequencies are measured in units of ω_0 . The effective Hamiltonian is non-Hermitian (i.e., $H^\dagger \neq H$) and commutes with PTX ; here \mathcal{P} , \mathcal{T} , and \mathcal{X} are defined in Eq. 2- 2 in the main text. The Hamiltonian

and eigenmodes of this PTX system can be linked to those of its PT counterpart (H', Ψ') through the similarity transformation $H = S^{-1} H' S$ and $\Psi = S^{-1} \Psi'$, where S is an invertible 4-by-4 matrix $S = \mathbf{1} \otimes \zeta$ and $\zeta = \begin{pmatrix} x^{1/2} & 0 \\ 0 & 1 \end{pmatrix}$. As a result, the PTX and PT systems share the same eigenfrequencies, given by:

$$\omega_{1,2,3,4} = \pm \sqrt{\frac{2 - \gamma^2(1 - \kappa^2) \pm \sqrt{4\kappa^2 - 4\gamma^2(1 - \kappa^2) + \gamma^4(1 - \kappa^2)^2}}{2(1 - \kappa^2)}}, \quad (2-19)$$

which is found to be independent of x . Such results are consistent with our previous findings on the series $-RLC/RLC$ dimer satisfying the PTX -symmetry. The scaling coefficient x plays a role in controlling the linewidth of the resonance. Therefore, the PTX -symmetry concept can also be exploited to improve the Q -factor and sensitivity of a wireless resonant sensor based on a parallel RLC circuit model.

Reflectionless Property and Impedance Matching

Figure 2-15a considers a generalized PTX -symmetric circuit that is invariant under the PTX transformation. Here, $\mathcal{X} = \mathbf{1} \otimes x_0$ and $x_0 = \begin{pmatrix} (x/y)^{1/2} & 0 \\ 0 & (x/y)^{-1/2} \end{pmatrix}$, which yield $q_1 \rightarrow (x/y)^{1/2} q_1$ and $q_2 \leftrightarrow (x/y)^{-1/2} q_2$. In this case, both active and passive tanks have the same non-Hermiticity parameter as $\gamma = (x|-R|)^{-1} \sqrt{(xL)/(C/x)} = (yR)^{-1} \sqrt{(yL)/(C/y)}$. For this coupled circuit, the input impedance looking into the $-RLC$ tank from the RF generator end can be derived as:

$$Z_{in} = Z_0 \frac{\omega^2 - i\omega\gamma(\omega^2 - 1) - x \left[\omega^2 - \gamma^2 (2\omega^2 + \omega^4(\mu^2 - 1) - 1) \right] / \eta}{\omega^2 - i\omega\gamma(\omega^2 - 1)}, \quad (2-20)$$

where ω is the angular frequency, the generator impedance $Z_0 = \eta R$ [Ω], and η is the impedance normalization factor. In the single-port measurement, the information is encoded in the reflection coefficient at the input port, which can be written as:

$$\Gamma = (Z_{in} - Z_0) / (Z_{in} + Z_0). \quad (2-21)$$

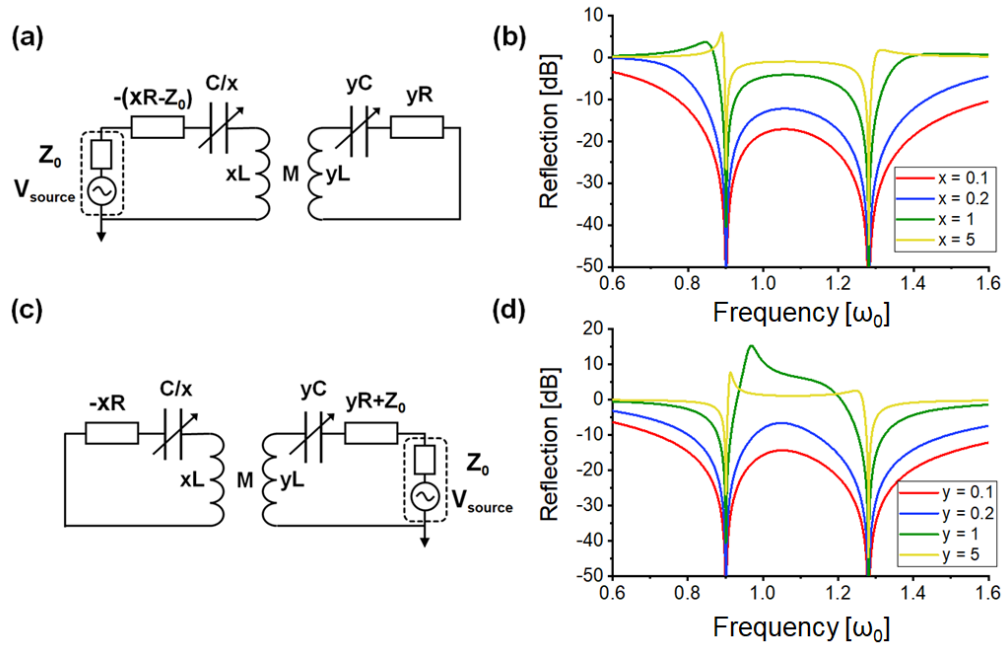


Figure 2-15 (a) PTX-symmetric circuits with the RF excitation source connected to the active -RLC tank. (b) Reflection spectrum for the single-port circuit in (a), under different values of x . (c) PTX-symmetric circuits with the RF excitation source connected to the passive RLC tank; the circuits in (a) and (c) share the same eigenfrequencies, as they represent the same type of -RLC/RLC dimer in the coupled-mode analysis. (d) Reflection spectrum the single-port circuit in (a), under different values of y . In the PTX-symmetric circuits, the resonant frequencies remain constant, while the bandwidth (or Q-factor) can be tailored by varying the scaling coefficient x or y .

It is interesting to note that the input impedance and the reflection coefficient are independent of y used in the RLC tank. This could enable more flexibility in the sensor design when compared with the traditional PT -symmetric setup. The input impedance and reflection coefficient of the PT -symmetric telemetry system are obtained by setting $x = 1$ in Eq. 2- (21). In the exact PT -/ PTX -symmetric phase, the eigenfrequencies are real, corresponding to the dips in the reflection spectrum. From the RF circuit viewpoint, the reflectionless property is due to the perfect impedance matching, namely $Z_{in} = Z_0$ at the eigenfrequencies (resonance frequencies), leading to $\Gamma = 0$.

Figure 2-15b shows the reflection spectrum for the PTX -symmetric circuits in Fig. 2-60a, under different values of x ; here $\gamma = 2.5$, $\mu = 2.5$, $\eta = 0.2$, and y is an arbitrary positive real number (because Z_{in} and Γ are independent of y). The PT -symmetric system is obtained when $x = y = 1$. It can be seen from Fig. 2-60b that for different PTX -symmetric systems, the reflection coefficient is always zero at the given eigenfrequencies, while the resonance linewidth can be tuned by varying the scaling coefficient x . Most importantly, the Q -factor, which is inversely proportional to the resonance bandwidth, increases with increasing the value of x , as has been demonstrated in our telemetry experiments (Fig. 2-5). As opposed to an active reader, a passive reader with $x \leq \eta$ can exhibit low reflection over a broad bandwidth, which could be of interest for applications that require large amounts of bandwidth, such as the high-speed communication.

Figure 2-15c considers the second case, in which the RF input port is connected to the passive RLC tank (e.g., an active sensor interrogated by a passive reader). In this scenario, the input impedance can be derived as:

$$Z_{in} = Z_0 \frac{\omega^2 + i\omega\gamma(\omega^2 - 1) + y \left[\omega^2 - \gamma^2 (2\omega^2 + \omega^4(\mu^2 - 1) - 1) \right] / \eta}{\omega^2 + i\omega\gamma(\omega^2 - 1)}. \quad (2-22)$$

It is worth mentioning that in this case, the input impedance and the reflection coefficient are independent of x used in the active tank. According the coupled-mode analysis, the circuits in Figs. S10a and S10c share the same eigenfrequencies. In the exact *PTX*-symmetric phase, applying the real eigenfrequencies to the input impedance in Eq. 2- (22) results in $Z_{in} = Z_0$ and thus zero reflection can be obtained in these frequencies. Figure 2-15d shows the reflection spectra for the *PTX*-symmetric circuits in Fig. 2-60c, under different values of y ; here $\gamma = 2.5$, $\mu = 2.5$, $\eta = 0.2$, and x is an arbitrary positive real number (because Z_{in} and Γ are independent of x). It is clearly seen that the zero reflection takes place at the same frequencies observed in Fig. 2-60b, and the resonance linewidth can be tuned by varying the value of y .

2.10 Conclusions

We have applied *PT*-symmetry and the generalized *PTX*-symmetry condition to RF sensor telemetry with a particular focus on compact wireless micro-mechatronic sensors and actuators. Our approach overcomes the long-standing challenge of implementing a miniature wireless microsensor with high spectral resolution and high sensitivity, and opens opportunities to develop loss-immune high-performance sensors, due to gain-loss interactions via inductive coupling and eigenfrequency bifurcation resulting from the *PT* (*PTX*)-symmetry. Our findings also provide alternative schemes and techniques to reverse the effects of loss and enhance the Q -factor of various RF systems. Through our study of *PTX*-symmetry, I have shown that even asymmetric profiles of gain and loss coefficients can yield exotic non-Hermitian physics observed in *PT*-symmetric structures. Importantly, compared to *PT*-symmetry, *PTX*-symmetry offers greater

design flexibility in manipulating resonance linewidths and Q-factors, while exhibiting eigenfrequencies identical to the associated PT -symmetric system.

REFERENCES

- [1] Chen, P.J., et al. "Microfabricated implantable parylene-based wireless passive intraocular pressure sensors." *J. Microelectromech. Syst.*, vol. **17**, 1342-1351, 2008.
- [2] Chen, P.J, Saati, S., Varma, R., Humayun, M.S., and Tai, Y.C., "Wireless intraocular pressure sensing using microfabricated minimally invasive flexible-coiled LC sensor implant." *J. Microelectromech. Syst.*, vol. **19**, 721-734, 2010.
- [3] Nopper, R., Niekrawietz, R., and Reindl, L., "Wireless readout of passive LC sensors." *IEEE Trans. Instrum. Meas.*, vol. **59**, 2450–2457, 2010.
- [4] Tan, Q., et al. "A harsh environment-oriented wireless passive temperature sensor realized by LTCC technology." *Sensors*, vol. **14**, 4154-4166, 2014.
- [5] Li, C., et al. "A high-performance LC wireless passive pressure sensor fabricated using low-temperature co-fired ceramic (LTCC) technology." *Sensors*, vol.**14**, 23337-23347, 2014.
- [6] Li, C., Rodger, D.C., Saati, S., Humayun, M.S., and Tai, Y.C., "A noncontact wireless passive radio frequency (RF) resonant pressure sensor with optimized design for applications in high-temperature environments." *Meas. Sci. Technol.*, vol. **25**, 075101, 2014.
- [7] Peng, Y., et al. "Characterization of a passive telemetric system for ISM band pressure sensors," *J. Electron. Test.*, vol. **30**, 665-671, 2014.
- [8] Wang, X., *Wireless pressure sensor system for medical applications*, University of South Carolina, 2013 (Open access thesis at: <http://scholarcommons.sc.edu/etd>).
- [9] Mokwa, W., "Medical implants based on microsystems." *Meas. Sci. Technol.*, vol. **18**, R47-R57, 2007.
- [10] Liu, C., *Foundations of MEMS*, Pearson Education, India, 2012.
- [11] Lee, T.H., *Planar microwave engineering: a practical guide to theory, measurement, and circuits*, Cambridge University Press, Cambridge, United Kingdom, 2004.

- [12] Raju, S., Wu, R., Chan, M., and Yue, C.P., "Modeling of mutual coupling between planar inductors in wireless power applications." *IEEE Trans. Power Electron.*, vol. **29**, 481-490, 2014.
- [13] CST Microwave Studio at: <http://www.cst.com>.
- [14] Yazgi, M., Toker, A., and Virdee, B.S., "A new negative resistance circuit and an application for loss compensation in a distributed amplifier." *Ana. Int. Cir. Sig. Process.*, vol. **60**, 215-220, 2009.
- [15] Razavi, B., *RF microelectronics*, vol. **1**, New Jersey: Prentice Hall, 1998.
- [16] Razavi, B., "The Cross-Coupled Pair—Part III." *IEEE J. Solid-State Circuits*, vol. **11**, 2015.
- [17] Vittoz, E., Degrauwe, M.G.R., and Bitz, S., "High-performance crystal oscillator circuits: theory and application." *IEEE J. Solid-State Circuits*, vol. **23**, 774-783, 1988.
- [18] Rohde, U.L., Poddar, A.K., and Böck, G., *The design of modern microwave oscillators for wireless applications: theory and optimization*, John Wiley & Sons, 2005.
- [19] Rohde, U.L. and Rudolph, M., *RF/microwave circuit design for wireless applications*, John Wiley & Sons, 2013.
- [20] Ulansky, V.V., Fituri, M.S., and Machalin, I.A., "Mathematical modeling of voltage-controlled oscillators with the Colpitts and Clapp topology." *Electronics and Control Systems*, vol. **19**, 82-90, 2009.
- [21] Mayaram, K., "Output voltage analysis for the MOS Colpitts oscillator." *Trans. Circuits Syst. I, Fundam. Theory Appl.*, vol. **47**, 260-263, 2000.
- [22] Pozar, D.M., *Microwave engineering*, John Wiley & Sons, 2009.
- [23] Schindler, J., et al. "PT-symmetric electronics." *J. Phys. A: Math. Theor.* vol. **45**, 444029, 2012.
- [24] Advanced Design System (ADS) at: <http://www.keysight.com/>.

III. ULTRASENSITIVE, PARITY-TIME SYMMETRIC WIRELESS REACTIVE AND RESISTIVE SENSORS

Parts of this chapter have been presented in (Sakhdari et al., 2018, IEEE) Copyright©2019, IEEE.

We propose a new readout paradigm for enhancing the performance of wireless passive resistor-inductor-capacitor (*RLC*) sensors. Here, I consider a passive *RLC* sensor inductively coupled to an active reader, with the equivalent circuit of the whole telemetry system satisfying the parity-time (*PT*) symmetry or space-time reflection symmetry. I demonstrate that the *PT*-symmetric wireless sensor system, when compared to conventional interrogation techniques using a passive coil reader, may provide significantly improved quality factor (*Q*-factor), sensing resolution, and sensitivity in response to the sensor's reactance or resistance variation. Our results may have impact on various wireless sensing, detection, and imaging systems, particularly for emerging micromachined sensors, miniature implants and wearables, and internet-of-things (IoTs) applications.

3.1 Wireless Reactive and Resistive Sensors

Many medical, industrial, and automotive applications require sensing of local physical or chemical quantities, where the wired connection between the sensor and the data acquisition system is not accessible. Representative examples include various bio-implants inside the human body (e.g. intraocular pressure sensors, intravascular pressure sensors, intracranial sensors, and tissue-characterization sensors [1]-[6]), pressure sensors on rotating components of vehicle, and sensing in harsh environments (e.g. corrosive media or high temperature [7]-[8]).

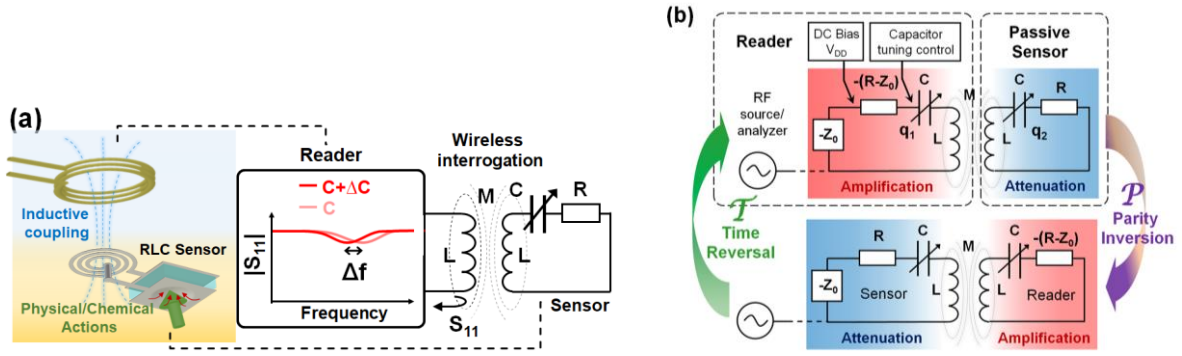


Figure 3-1 (Color online) **a** Schematics of a wireless passive RLC sensor, inductively coupled to a coil reader, and its equivalent circuit model. **b** Equivalent-circuit expression of the PT -symmetric wireless sensor system.

Telemetric sensing based on battery-free passive wireless sensors or radio-frequency identification (RFID) tags is perhaps one of the most viable ways to achieve the contactless and continuous measurement for the above mentioned applications. To date, a great number of low-cost and low-profile wireless sensors have been proposed to measure miscellaneous quantities, such as temperature [8]-[9], pressure [1],[7],[10],[12], liquid volume [13]-[14], humidity [15]-[16], mechanical strain [17], and chemical reactions (e.g., chemiresistive sensors) [13]. Most of these sensing devices are based on the passive RLC tank, where the quantity to be measured may detune the resistance or reactance of the sensor, resulting in the resonance frequency shift. A reader coil antenna is usually used to measure the frequency response of the wireless sensor through the inductive coupling, as illustrated in Fig. 3-1a.

Although so far many research efforts have been focused on the design and fabrication of the miniature and functional sensors, very limited effort has been made to develop a more robust and sensitive wireless readout technique. However, existing readout methods for passive wireless sensors still face several challenges. For instance, sensitivity and minimum detection range of the miniature wireless sensors (e.g. integrated circuit piezoelectric or ICP sensors) usually suffer from

the small resonance frequency shift and the low Q -factor, resulting from limited device dimensions, skin-effect and Eddy-current losses, and background absorption (e.g. human body at high frequencies). In general, an effective resistance taking into account the total power dissipation must be introduced into the RLC tank, as shown in Fig. 3-1a.

In this work, I present a new wireless readout technique based on the concept of PT -symmetry, which may significantly enhance the sensitivity and the detection limit of the transformer-based sensors. Figure 3-1b shows the equivalent circuit of the proposed PT -symmetric wireless sensor system, where the passive wireless functional sensor, modeled by an equivalent RLC tank circuit, is inductively coupled to an active $-RLC$ reader circuit. The whole telemetry system fulfills the spatial-inversion and time-reversal symmetry, so-called PT -symmetry. In the following, I will theoretically and experimentally investigate the performance and critical operation conditions of the proposed PT -symmetric wireless sensors, which can provide loss compensation and optimal sensing performance.

3.2 Theory of PT -Symmetric Telemetry sensor systems

The concept of PT -symmetry originates from the quantum physics, where a non-Hermitian Hamiltonian can have real eigenfrequencies, if the Schrödinger system is invariant under operations of spatial reflection P and time reversal T [18]. Thanks to formal similarities between Schrödinger and Helmholtz equations, PT -symmetry can be experimentally demonstrated in electromagnetic systems with balanced gain and loss [19]-[24], including transmission-line networks, coupled waveguides/cavities, and lumped-element circuits [25]-[30]. As illustrated in Fig. 3-1b, a PT -symmetric electronic circuit can be made by pairing the $-RLC$ and RLC tanks, correspondingly responsible for the amplification and attenuation of the RF signal. When a RF source, such as a frequency synthesizer based on the negative-resistance device, excites this dimer circuit, a negative

generator impedance $-Z_0$ must be included in the normal-mode (closed-loop) analysis [31]. While a positive resistor renders energy dissipation, a negative resistor implies an energy source. Therefore, for balancing gain and loss in the system, a negative-resistance converter (NRC) with resistance of $-(R-Z_0)$ must be used in the $-RLC$ tank, if the $-RLC$ tank is connected to the RF signal generator.

Applying Kirchhoff's laws to the circuit in Fig. 3-1b leads to the following set of equations:

$$\begin{aligned} \frac{d^2 q_1}{d\tau^2} &= -\frac{1}{1-\kappa^2} q_1 + \frac{\kappa}{1-\kappa^2} q_2 + \frac{1}{\gamma(1-\kappa^2)} \dot{q}_1 + \frac{\kappa}{\gamma(1-\kappa^2)} \dot{q}_2 \\ \frac{d^2 q_2}{d\tau^2} &= \frac{\kappa}{1-\kappa^2} q_1 - \frac{1}{1-\kappa^2} q_2 - \frac{\kappa}{\gamma(1-\kappa^2)} \dot{q}_1 - \frac{1}{\gamma(1-\kappa^2)} \dot{q}_2, \end{aligned} \quad (3-1)$$

where q_1 (q_2) corresponds to the charge stored on the capacitor in the amplifying (attenuating) tank, $\tau \equiv \omega_0 t$, $\omega_0 = 1/\sqrt{LC}$ is the natural frequency of an RLC tank, $\gamma = R^{-1}\sqrt{L/C}$ is the dimensionless gain-loss parameter or the non-Hermiticity parameter in the terminology of PT -symmetric systems, and

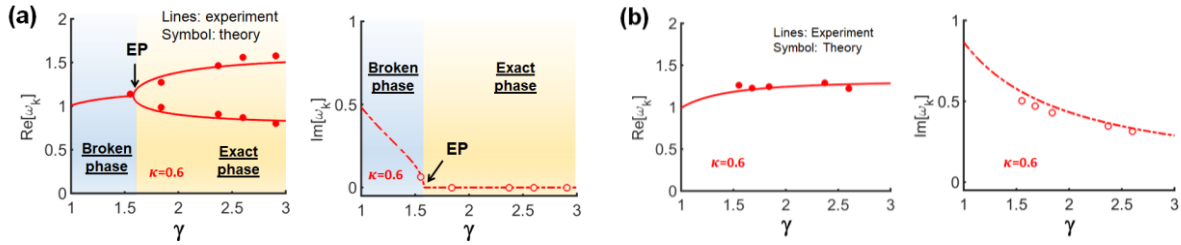


Figure 3-2 (Color online) **a** Real (left) and imaginary (right) eigenfrequency versus the non-Hermiticity parameter γ for the PT -symmetric circuit in Fig. 2-1b. **b** is similar to (a), but for measurement results obtained by the micro-coil reader shown in Fig. 1a. Here, eigenfrequencies are in units of ω_0 .

$\kappa = M/L$ is the coupling strength between the $-RLC$ and RLC tanks; here all frequencies are measured in units of ω_0 . I find that Eq. (3-1) remains unchanged under the combined \mathcal{P} ($q_1 \leftrightarrow q_2$) and \mathcal{T} ($t \leftrightarrow -t$) transformations. Further, Eq. (3-1) can be written in the Liouvillian formalism as [32]:

$$\frac{d\Psi}{d\tau} = \mathcal{L}\Psi;$$

$$\mathcal{L} = \begin{pmatrix} 0 & 0 & 1 & 0 \\ 0 & 0 & 0 & 1 \\ -\frac{1}{1-\kappa^2} & \frac{\kappa}{1-\kappa^2} & \frac{1}{\gamma(1-\kappa^2)} & \frac{\kappa}{\gamma(1-\kappa^2)} \\ \frac{\kappa}{1-\kappa^2} & -\frac{1}{1-\kappa^2} & -\frac{\kappa}{\gamma(1-\kappa^2)} & -\frac{1}{\gamma(1-\kappa^2)} \end{pmatrix}, \quad (3-2)$$

where $\Psi = (q_1, q_2, \dot{q}_1, \dot{q}_2)^T$. An effective Hamiltonian can be defined as $H_{eff} = i\mathcal{L}$, which takes a non-Hermitian form and is symmetric with respect to generalized \mathcal{PT} transformations:

$$\mathcal{P} = \begin{pmatrix} \sigma_x & 0 \\ 0 & \sigma_x \end{pmatrix}, \quad \mathcal{T} = \begin{pmatrix} \mathbf{I} & 0 \\ 0 & -\mathbf{I} \end{pmatrix} \mathcal{K}, \quad (3-3)$$

σ_x is the Pauli matrix, \mathbf{I} is an 2×2 identity matrix, and \mathcal{K} conducts the operation of complex conjugation. H_{eff} commutes with \mathcal{PT} , namely $[\mathcal{PT}, H_{eff}] = 0$, which implies that H_{eff} and \mathcal{PT} share the same set of eigenstates.

After the substitution of time-harmonic charge distributions $q_n = A_n e^{j\omega t}$, eigenfrequencies and eigenstates for this PT -symmetric circuitry can be obtained from the eigenvalue equation, $(H_{eff} - \omega_k \mathbf{I})\Phi_k = 0$ and $k = 1, 2, 3, 4$, as functions of the non-Hermiticity parameter γ and the coupling strength κ :

$$\omega_{1,2,3,4} = \pm \omega_0 \sqrt{\frac{2\gamma^2 - 1 \pm \sqrt{1 - 4\gamma^2 + 4\gamma^4 \kappa^2}}{2\gamma^2 (1 - \kappa^2)}}, \quad (3-4a)$$

$$\Phi_k = c_k \left(e^{j\phi_k}, e^{-j\phi_k}, j\omega e^{j\phi_k}, j\omega e^{-j\phi_k} \right)^T; c_k \in \mathbb{R}, \quad (3-4b)$$

$$e^{-2j\phi_k} = -\frac{\gamma \left[(1-\kappa^2)\omega_k^2 - 1 \right] - j\omega_k}{\kappa(\gamma - j\omega_k)}. \quad (3-4c)$$

The complex eigenfrequencies evolve with γ , showing three distinct regimes of behavior, as shown in Fig. 3-2a. The eigenfrequencies undergo a bifurcation process and branch out into the complex plane at the exceptional point (or the spontaneous PT -symmetry breaking point):

$$\gamma_{EP} = \frac{1}{\kappa} \sqrt{\frac{1 + \sqrt{1 - \kappa^2}}{2}}. \quad (3-5)$$

In the parametric region $\gamma \in [\gamma_{EP}, \infty]$, eigenfrequencies are purely real ($\gamma \in \mathbb{R}$) and $\mathcal{PT}\Phi_k = \Phi_k$ such that the PT -symmetry is *exact*. Moreover, if one seeks only purely real solutions, there is redundancy because positive and negative eigenfrequencies of equal magnitude are essentially identical. The motion in this exact PT -symmetric phase is oscillatory at the two eigenfrequencies (resonance frequencies in the reflection spectrum). At the exceptional point γ_{EP} , eigenfrequencies undergo a bifurcation process and branch out into the complex plane, and thus the PT -symmetry is spontaneously broken. The region $\gamma \in [\gamma_c, \gamma_{EP}]$ is known as the broken PT -symmetric phase, where that eigenfrequencies become two complex conjugate pairs ($\gamma \in \mathbb{C}$). In this region, $\mathcal{PT}\Phi_k \neq \Phi_k$ and thus the PT -symmetry is broken. Another crossing between the pairs of degenerate frequencies (and another branching) occurs at the lower critical point:

$$\gamma_c = \frac{1}{\kappa} \sqrt{\frac{1 - \sqrt{1 - \kappa^2}}{2}}. \quad (3-6)$$

In the sub-critical region $\gamma \in [0, \gamma_c]$, ω_k become purely imaginary and, therefore, the modes have no oscillatory part and simply blow up or decay away exponentially, which is of little interest for

telemetry sensing applications. Finally, I note that in the lossless scenario ($\gamma \rightarrow \infty$), two frequency pairs are given by $\omega_{1,2,3,4} = \pm 1 / \sqrt{1 \pm \kappa}$. These modes are associated with a pair of double-degenerate

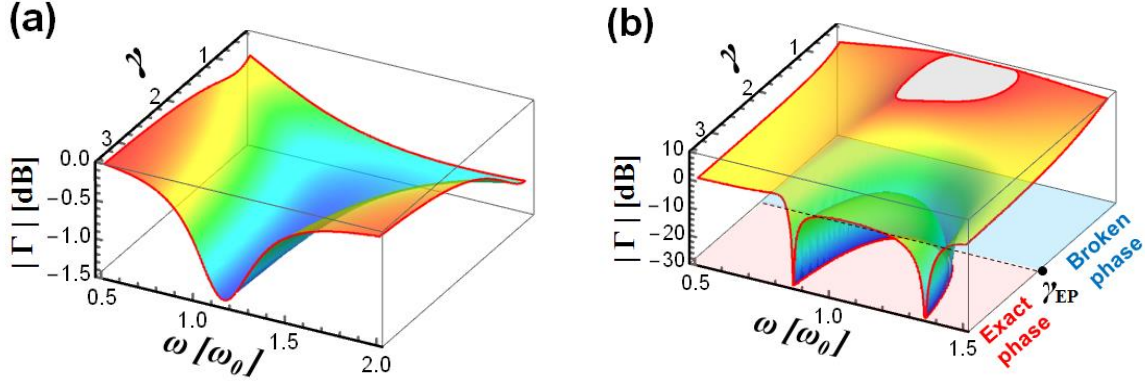


Figure 3-3 **a** Contours of reflection coefficient, as a function of the normalized operating frequency and the non-Hermiticity parameter, for the circuit of (a) the conventional wireless sensor system [Fig. 3-1(a)] and **b** the PT -symmetric one [Fig. 3-1(b)]; here the coupling strength $\kappa = 0.6$ and the input impedance of the RF source $Z_0 = 0.33 R$.

frequencies $\omega_k = \pm 1$ for a single isolated LC tank with $\kappa = 0$.

Figures 3a and 3b show the frequency responses of reflection (Γ), as functions of γ and the normalized frequency ω_k / ω_0 , for the conventional one [Fig. 3-1a] and the PT -symmetric wireless sensor system [Fig. 3-1b] [1]-[17] (which uses a reader coil with inductance L to interrogate the same passive sensor); here, I assume that the coupling strength $\kappa = 0.5$ and the input impedance of the RF source (e.g. a vector network analyzer or VNA) $Z_0 = 0.1R$. I find that resonant reflection dips in Fig. 3-3b are in consistent with the eigenfrequency analysis in Fig. 3-2a: (1) if $\gamma < \gamma_c$, there is no clear resonant peak, but purely amplifying or decay phenomena; (2) if $\gamma \in [\gamma_c, \gamma_{EP}]$, a broadband resonance is obtained, as the system operates in the broken PT -symmetry phase; (3) if $\gamma > \gamma_{EP}$, the

exact PT -symmetry phase yields two real eigenfrequencies, resulting in sharp reflection dips. Comparing the conventional fully-passive wireless sensing scheme and the PT one, it is seen that the proposed approach may provide superior sensitivity in terms of modulation depth, spectral resolution, and resonance frequency shift due to changes in γ (which is related to the sensor's effective resistance, capacitance, and inductance).

3.3 Implementation and Characterization of Wireless Capacitive Sensors

To validate the theoretical results in Section II, I have built a PT -symmetric RF circuit resembling a practical wireless sensor system. For example, many medical and industrial pressure

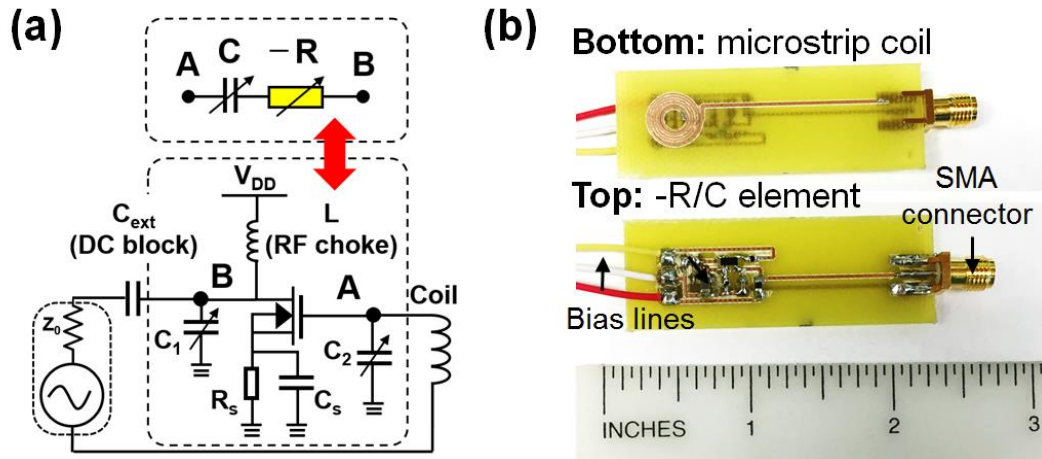


Figure 3-4 **a** Circuit diagram for the active reader consisting of an NRC, which is equivalent to a lumped negative resistor and **b** its practical implementation using the printed circuit board technique.

sensors are based on the capacitance change due to the mechanical deflection or the variation of

dielectric constant [8],[10]. In order to mimic a passive wireless capacitive sensor, I have made an onboard series RLC tank [Fig. 3-1a], consisting of a variable capacitor (BBY40: $C = 2\text{-}32$ pF), a resistor (MNR02JR-0402: $R = 150 \pm 0.5\% \Omega$) and a microstrip coil ($L = 0.3 \mu\text{H}$) [34]. To suit the PT -symmetric circuit topology in Fig. 3-1b, the reader needs to involve a negative resistor $-R$, which can be realized by a NRC that pulls in power to the circuit, rather than dissipating it like a resistor. The active reader, as a $-RLC$ tank, has the same effective capacitance and inductance as those of the passive RLC tank (i.e., sensor).

Figures 4a and 4b respectively show the circuit diagram and the photograph of the positive-feedback Colpitts-type NRC [34]-[38],[45],[46], which is equivalent to a negative resistor in series with a capacitor. Both effective $-R$ and C are tunable (via the external DC bias), stabilized, and non-dispersive over a wide frequency range. For the NRC circuit in Fig. 3-4a, if the transistor's transconductance $g_m \gg C_{gd}, C_{gs}$ (C_{gd} and C_{gs} are the gate-drain and gate-source capacitances), the equivalent impedance of the NRC is approximately given by:

$$Z_{eq} \approx -\frac{g_m}{\omega^2 C_1 C_2} - j\left(\frac{1}{\omega C_1} + \frac{1}{\omega C_2}\right), \quad (3-7)$$

where the real and imaginary parts correspond to the negative resistance and the capacitance.

The negative resistance value can be controlled by the DC offset voltages of the transistor (RF n-channel MOSFET: SOT-143). The effective capacitance of NRC is also tunable, if two voltage-controlled varactors C_1 and C_2 are used. We have designed and manufactured an active onboard reader ($-RLC$ tank) to wirelessly interrogate the RLC tank simulating the capacitive wireless sensor. Once the capacitance of the RLC tank is varied, the effective capacitance of the reader is adjusted accordingly to maintain the PT -symmetry condition. The inset of Fig. 3-5 shows our measurement setup, where the reader and the pseudo-sensor are separated by an air gap of 5 mm,

yielding a coupling strength $\kappa = 0.6$. Figures 5a and 5b present evolutions of the reflection spectrum with different capacitance values for the conventional [Fig. 3-1a] and PT -symmetric [Fig. 3-1b] wireless sensor systems, respectively; here the effective capacitance C of the RLC tank is varied from 2 pF to 7 pF, corresponding to the change of γ from 2.905 to 1.553.

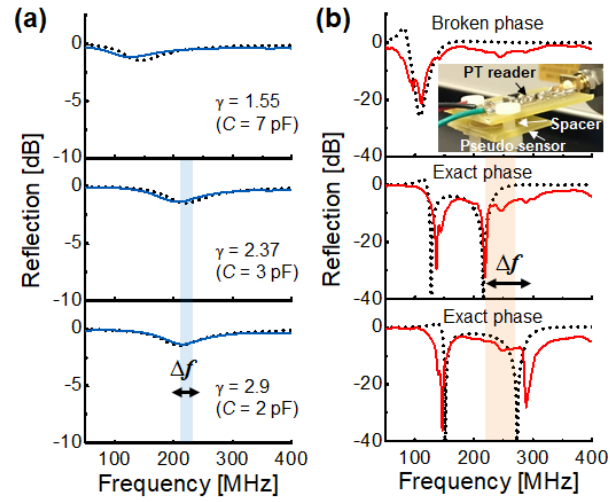


Figure 3-5 **a** Measured reflection coefficient for a passive RLC pseudo-sensor with an effective resistance $R = 150 \, \Omega$ and an effective inductance $L = 300 \, \text{nH}$, which is inductively coupled by (a) the conventional coil-antenna reader shown in Fig. 3-1a, and **b** the active reader ($-RLC$ tank in Fig. 3-1b) that accomplishes the PT -symmetric electronic system. The effective capacitance C of the RLC sensor is varied from 7 pF to 2 pF.

As can be seen in Fig. 3-5, experimental (solid lines) and theoretical (dashed lines) results agree quite well. The slight difference between the theory and experiment can be further improved by flattening the frequency response of NRC, which, for instance, could be achieved with the cross-

coupled transistor pair [34],[39] and the on-chip design. In this case, the non-Hermiticity parameter of the PT system, γ , as a function of C , determines whether the PT -symmetry is exact or broken. If $\gamma < \gamma_{EP}$, the system will operate in the broken PT -symmetric phase and vice versa. I have retrieved from measurement results [32] the complex eigenfrequency versus γ for both fully-passive and active wireless sensor systems in Fig. 3-5. Results are highlighted as dots in Fig. 3-2, which show excellent agreement with the theory. It is seen from Fig. 3-2 and Fig. 3-5 that by sweeping C from high to low values (or, effectively, sweeping γ from low to high values), the PT -symmetric telemetry system may evolve from the broken symmetry phase to the exact symmetry phase. The exact PT -symmetric phase results in real eigenfrequencies, associated with narrowband and sharp-peaked resonances. On the other hand, the broken PT -symmetry phase exhibits complex eigenfrequencies, associated with a weak and broad resonance. From Fig. 3-5, it is evidently seen that the PT -symmetric wireless readout technique, when operating in the exact symmetry phase, may enable much sharper reflection dips and greater Q -factor than the fully-passive readout technique. I note that if the negative resistor in the reader is replaced by a normal resistor of the same absolute resistance value, the PT -symmetry is no more valid and, therefore, the sharp resonances disappear (not shown here for saving some space).

It is worth mentioning that the PT -symmetric circuit may provide not only the loss compensation effect and the high- Q resonance, but also the enhanced sensitivity in response to the sensor's impedance perturbation. As can be seen in Figs. 3-2a and 3-2b, under the same values of $\Delta\gamma$, the PT -symmetric telemetric system shows a more dramatic shift in the resonance frequency, when compared with the traditional one using a coil reader (whose eigenfrequency variation is a flat line after being normalized by $\omega_0 = 1/\sqrt{LC}$). The sensitivity enhancement is particularly obvious around the singular exceptional point γ_{EP} , where the eigenfrequency bifurcation occurs [44].

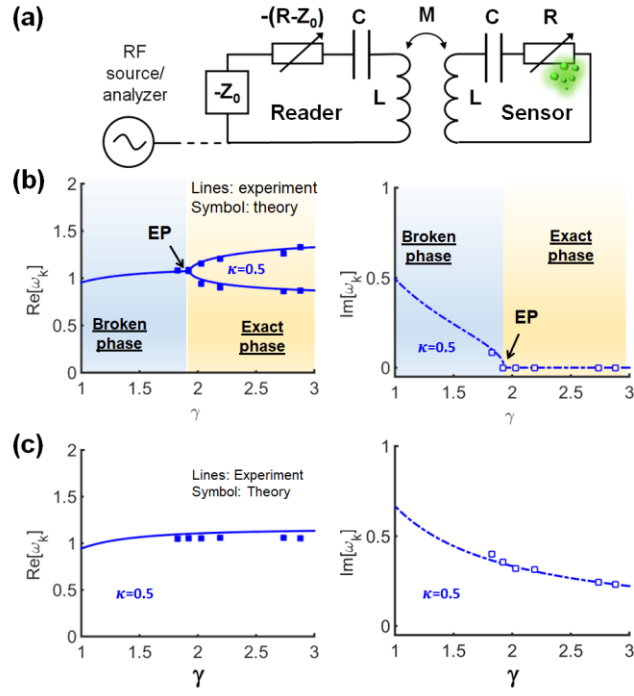


Figure 3-6 **a** Schematics of the PT -symmetric wireless resistive sensor system. **b** Real (left) and imaginary (right) eigenfrequency versus the non-Hermiticity parameter γ for the PT -symmetric circuit in (a). The resistance of the pseudo RLC sensor is varied from $190 \, \Omega$ to $300 \, \Omega$, corresponding to the change of γ from 2.8 to 1.9. (b) is similar to (a), but for measurement results obtained by the micro-coil reader shown in Fig. 3-1a. Here, eigenfrequencies are in units of ω_0 .

3.4 Implementation and Characterization of Wireless Resistive Sensors

Recently, there has been substantial investigation and research in wireless (bio-)chemical sensors based on the chemiresistor (i.e., chemically-tuned variable resistor). Particularly, nanomaterials (e.g., graphene [47],[48]) has been a recent thrust in micro/nano-sensor development. However, these resistive sensors typically exhibit poor sensitivity, due to the large electrical resistance of chemiresistor, which results in a low Q -factor and imperceptible resonance frequency shift. In this work, I also apply the concept of PT -symmetric telemetry to improve the sensing performance of wireless resistive sensors. In this scenario, a variable resistor is connected in series with a capacitor and an inductor, forming a passive RLC tank. The passive sensor is

inductively coupled to an active reader based on a $-RLC$ tank, as shown in Fig. 3-6a. For the proof-

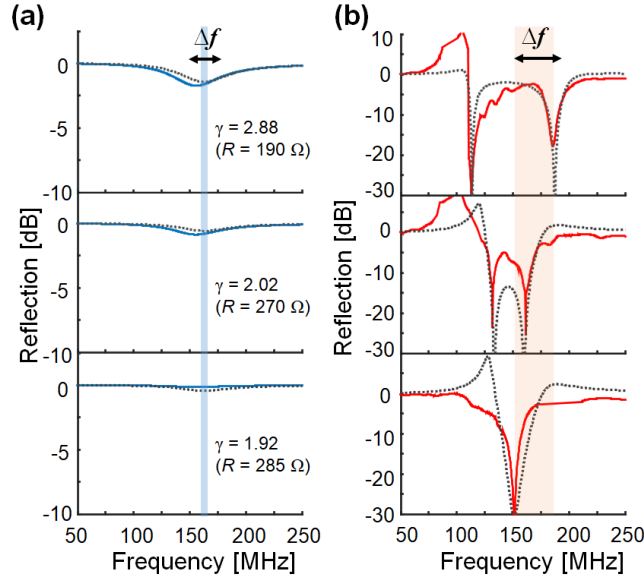


Figure 3-7 **a** Measured reflection coefficient for a (pseudo) RLC sensor with effective capacitance $C = 2$ pF and effective inductance $L = 600$ nH, which is wirelessly read by (a) the conventional coil-antenna reader shown in Fig. 3-1a, and **b** the active reader ($-RLC$ tank in Fig. 6b). The effective resistance R of the pseudo RLC sensor is varied from 190Ω to 300Ω .

of-concept demonstration, I used a variable onboard RLC tank with a variable resistor to simulate the resistance variation caused by, for instance, chemical reactions in a chemiresistor. The series RLC tank is built by a microstrip coil ($L \approx 0.6 \mu\text{H}$), a capacitor (BBY40: $C \approx 2$ pF), and a variable resistor (MNR02JR-0402: $R = 150\sim 300 \pm 0.5\% \Omega$). The active reader is similar to the one used in Section III, of which the effective negative resistance is tuned by the external DC bias. When the active reader ($-RLC$ tank) is used to wirelessly interrogate the pseudo resistive sensor (RLC tank), the PT -symmetric telemetry system can be achieved, with the equivalent circuit shown in Fig. 3-6a.

Figure 3-6b presents the theoretical (solid lines) and experimental (dots) results for the complex eigenfrequency as a function of the non-Hermiticity parameter γ , which is varied by adjusting the effective resistance of the *RLC* tank sensor. A good agreement between experimental and simulation results can be seen in Fig. 3-6. Similar to the case of *PT*-symmetric wireless capacitive sensor [Fig. 3-2], there exists two distinct regimes of behavior divided by the exceptional point. As can be seen in Fig. 3-6b, near the exceptional point, the real eigenfrequencies become ultrasensitive to perturbation of the sensor's effective resistance. Figure 3-6c is similar to Fig. 3-6b, but for the fully-passive wireless sensing scheme using a simple micro-coil reader, showing that the eigenfrequency is a complex and quite insensitive to the change in γ (or R of the sensor).

Figs. 3-7a and 3-7b respectively present evolutions of reflection spectrum for the fully-passive and *PT*-symmetric wireless sensor systems in Fig. 3-6. In both cases, measurements results (solid lines) are in good agreement with theory (dashed lines). As can be seen in Fig. 3-7, in the *PT*-symmetric telemetry system, the real eigenfrequencies give rise to sharp and high- Q reflection dips, even though the sensor's effective resistance is large. However, the passive micro-coil reader only achieves a weak resonance with a broad linewidth. Again, our results demonstrate that a wireless sensor system engineered into the *PT*-symmetric dimer can provide superior sensitivity and detectivity, as it achieves not only higher spectral resolution and greater modulation depth, but also more very sensitive frequency responses associated with the exceptional point, well beyond the capability of fully-passive interrogation techniques. Fundamentally different from conventional loss-compensation resonator circuit, where $-R$ and R components are in direct contact, [45][46], in our *PT*-symmetric telemetry system, the balanced gain and loss are wirelessly interacted, thus offering a promising route for improving the performance of the wireless reactive and resistive sensors (e.g., without the need of active component and power source in the sensor).

3.5 Conclusions

We have put forward the concept and practical designs of the PT -symmetric telemetry system for enhancing the sensitivity and detection limit of versatile RLC -based passive wireless sensors. Specifically, the equivalent circuit of the wireless sensor system is properly tailored to satisfy the spatial-inversion and time-reversal symmetry. I have first theoretically studied different PT phases and critical conditions for obtaining the optimal sensing performance. Then, I have experimentally demonstrated the possibility of using the PT -symmetry concept to wirelessly read the (lossy) capacitive and resistive sensors, with high spectral resolution and high sensitivity. The proposed wireless sensing technique is potentially revolutionary, as it may be beneficial to a plurality of environmental, wearable, and implantable wireless sensors, as well as emerging applications in the fields of IoTs and RFIDs.

REFERENCES

- [1] P. J. Chen, D. C. Rodger, S. Saati, M. S. Humayun, and Y. C. Tai, "Microfabricated implantable parylene-based wireless passive intraocular pressure sensors." *J. Microelectromech. Syst.*, vol. 17, no. 6, pp. 1342-1351, Dec. 2008.
- [2] L. Brancato, G. Keulemans, T. Verbelen, B. Meyns, and R. Puers, "An implantable intravascular pressure sensor for a ventricular assist device." *Micromachines*, vol. 7, no. 8, p. 135, Aug. 2016.
- [3] M. Yvanoff, and J. Venkataraman, "A feasibility study of tissue characterization using LC sensors." *IEEE Trans. Antennas Propag.*, vol. 57, no. 4, pp. 885-893, Apr. 2009.
- [4] M. Sakhdari, M. Hajizadegan, Y. Li, M. M.-C. Cheng, J. C. Hung, and P.-Y. Chen, "Ultrasensitive, Parity-Time-Symmetric Wireless Reactive and Resistive Sensors," *IEEE Sensors Journal*, 2018.
- [5] L. Y. Chen, B. C. K. Tee, A. L. Chortos, G. Schwartz, V. Tse, D. J. Lipomi, H. S. Ph. Wong, M. V. McConnell, and Z. Bao, "Continuous wireless pressure monitoring and mapping with ultra-small passive sensors for health monitoring and critical care." *Nature Commun.*, vol. 5, Oct. 2014.
- [6] M. W. A. Khan, T. Björninen, L. Sydänheimo, and L. Ukkonen, "Remotely powered piezoresistive pressure sensor: toward wireless monitoring of intracranial pressure." *IEEE Microwave Wireless Compon. Lett.*, vol. 26, no. 7, pp. 549-551, Jul. 2016.
- [7] S. Rodriguez, S. Ollmar, M. Waqar, and A. Rusu, "A batteryless sensor ASIC for implantable bio-impedance applications." *IEEE Trans. Biomed. Circuits Syst.*, vol. 10, no. 3, pp. 533-544, Jun. 2016.
- [8] C. Li, D. C. Rodger, S. Saati, M. S. Humayun, and Y. C. Tai, "A noncontact wireless passive radio frequency (RF) resonant pressure sensor with optimized design for applications in high-temperature environments." *Meas. Sci. Technol.*, vol. 25, no. 7, pp. 075101, May. 2014.
- [9] Q. Tan, T. Luo, J. Xiong, H. Kang, X. Ji, Y. Zhang, M. Yang, X. Wang, C. Xue, J. Liu, and W. Zhang, "A harsh environment-oriented wireless passive temperature sensor realized by LTCC technology." *Sensors*, vol. 14, no. 3, pp. 4154-4166, Mar. 2014.

- [10] H. Kairm, D. Delfin, M. A. I. Shuvo, L. A. Chavez, C. R. Garcia, J. H. Barton, S. M. Gaytan, M. A. Cadena, R. C. Rumpf, R. B. Wicker, and Y. Lin, "Concept and model of a metamaterial-based passive wireless temperature sensor for harsh environment applications." *IEEE Sens. J.*, vol. 15, no. 3, pp. 1445-1452, Mar. 2015.
- [11] C. Li, Q. Tan, C. Xue, W. Zhang, Y. Li, and J. Xiong, "A high-performance LC wireless passive pressure sensor fabricated using Low-Temperature Co-Fired Ceramic (LTCC) technology." *Sensors*, vol. 14, no. 12, pp. 23337-23347, Dec. 2014.
- [12] P. J. Chen, S. Saati, R. Varma, M. S. Humayun, and Y. C. Tai, "Wireless intraocular pressure sensing using microfabricated minimally invasive flexible-coiled LC sensor implant." *J. Microelectromech. Syst.*, vol. 19, no. 4, pp. 721-734, Aug. 2010.
- [13] U. Kawoos, X. Meng, M. Tofighi, and A. Rosen, "Too much pressure: Wireless intracranial pressure monitoring and its application in traumatic brain injuries." *IEEE Microwave Mag.*, vol. 16, no. 2, pp. 39-53, Mar. 2015.
- [14] H. Huang, P. Y. Chen, C. H. Hung, R. Gharpurey, and D. Akinwande, "A zero power harmonic transponder sensor for ubiquitous wireless μ L liquid-volume monitoring." *Sci. Rep.*, vol. 6, p. 18795, Jan. 2016.
- [15] E. Silavwe, N. Somjit, and I. D. Robertson, "A Microfluidic-Integrated SIW Lab-on-Substrate Sensor for Microliter Liquid Characterization." *IEEE Sens. J.*, vol. 16, no. 21, pp. 7628-7635, Nov. 2016.
- [16] Q. Y. Ren, L. F. Wang, J. Q. Huang, C. Zhang, and Q. A. Huang, "Simultaneous remote sensing of temperature and humidity by LC-type passive wireless sensors." *J. Microelectromech. Syst.*, vol. 24, no. 4, pp. 1117-1123, Aug. 2015.
- [17] X. Wang, O. Larsson, D. Platt, S. Nordlinder, I. Engquist, M. Berggren, and X. Crispin, "An all-printed wireless humidity sensor label." *Sens. Actuators, B*, vol. 166, pp. 556-561, May. 2012.
- [18] Y. Peng, B. F. Rahman, T. Wang, G. Wang, X. Liu, and X. Wen, "Characterization of a passive telemetric system for ISM band pressure sensors." *J. Electron. Test.*, vol. 30, no. 6, pp. 665-671, Dec. 2014.
- [19] C. M. Bender, and Stefan Boettcher, "Real spectra in non-Hermitian Hamiltonians having P T symmetry." *Phys. Rev. Lett.*, vol. 80, no. 24, p. 5243, Jun. 1998.

- [20] Z. Lin, H. Ramezani, T. Eichelkraut, T. Kottos, H. Cao, and D. N. Christodoulides, “Unidirectional invisibility induced by P T-symmetric periodic structures.” *Phys. Rev. Lett.*, vol. **106**, no. 21, p. 213901, May. 2011.
- [21] A. Regensburger, M. A. Miri, C. Bersch, J. Nager, G. Onishchukov, D. N. Christodoulides, and U. Peschel, “Observation of defect states in P T-symmetric optical lattices.” *Phys. Rev. Lett.*, vol. 110, no. 22, p. 223902, May. 2013.
- [22] A. Mostafazadeh, “Invisibility and PT symmetry.” *Phys. Rev. A*, vol. 87, no. 21, p. 012103, Jan. 2013.
- [23] L. Feng, Y. L. Xu, W. S. Fegadolli, M. H. Lu, J. E. Oliveira, V. R. Almeida, Y. F. Chen, and A. Scherer, “Experimental demonstration of a unidirectional reflectionless parity-time metamaterial at optical frequencies.” *Nat. Mater.*, vol. 12, no. 2, pp. 108-113, Feb. 2013.
- [24] K. G. Makris, R. El-Ganainy, D. N. Christodoulides, and Z. H. Musslimani, “Beam dynamics in P T symmetric optical lattices.” *Phys. Rev. Lett.*, vol. 100, no. 10, p. 103904, Mar. 2008.
- [25] Ch. E. Ruter, K. G. Makris, R. El-Ganainy, D. N. Christodoulides, M. Segev, and D. Kip, “Observation of parity–time symmetry in optics.” *Nat. Phys.*, vol. 6, no. 3, pp. 192-195, Mar. 2010.
- [26] J. M. Lee, S. Factor, Z. Lin, I. Vitebskiy, F. M. Ellis, and T. Kottos, “Reconfigurable directional lasing modes in cavities with generalized P T Symmetry.” *Phys. Rev. Lett.*, vol. 112, no. 25, p. 253902, Jun. 2014.
- [27] H. Benisty, A. Degiron, A. Lupu, A. De Lustrac, S. Chenais, S. Forget, M. Besbes, G. Barbillon, A. Bruyant, S. Blaize, and G. Lerondel, “Implementation of PT symmetric devices using plasmonics: principle and applications.” *Opt. Express*, vol. 19, no. 19, pp. 18004-18019, Sep.2011.
- [28] R. Fleury, D. Sounas, and A. Alu, “An invisible acoustic sensor based on parity-time symmetry.” *Nat. Commun.*, vol. 6, Jan. 2015.
- [29] X. Y. Lu, H. Jing, J. Y. Ma, and Y. Wu, “P T-symmetry-breaking chaos in optomechanics.” *Phys. Rev. Lett.*, vol. 114, no. 25, p. 253601, Jun. 2015.

- [30] Xun-Wei Xu, Y. X. Liu, C. P. Sun, and Y. Li, "Mechanical PT symmetry in coupled optomechanical systems." *Phys. Rev. A*, vol. 92, no. 1, p. 013852, Jul. 2015.
- [31] L. Chang, X. Jiang, S. Hua, C. Yang, J. Wen, L. Jiang, G. Li, G. Wang, and M. Xiao, "Parity-time symmetry and variable optical isolation in active-passive-coupled microresonators." *Nat. Photonics*, vol. 8, no. 7, pp. 524-529, Jul. 2014.
- [32] D. M. Pozar, *Microwave engineering*. John Wiley & Sons, Sep. 2009.
- [33] J. Schindler, A. Li, M. C. Zheng, F. M. Ellis, and T. Kottos, "Experimental study of active LRC circuits with PT symmetries." *Phys. Rev. A*, vol. **84**, no. 4, p. 040101, Oct. 2011.
- [34] Advanced Design System (ADS): <http://www.keysight.com/>.
- [35] Thomas H. Lee, *Planar microwave engineering: a practical guide to theory, measurement, and circuits*. Cambridge University Press, vol. 1, Aug. 2004.
- [36] M. Yazgi, A. Toker, and B. S. Virdee, "A new negative resistance circuit and an application for loss compensation in a distributed amplifier." *Analog Integrated Circuits and Signal Processing*, vol. 60, no. 30, pp. 215-220, Sep. 2009.
- [37] B. Razavi, *RF microelectronics*. New Jersey: Prentice Hall, vol. 2, Jan. 1998.
- [38] B. Razavi, "The Cross-Coupled Pair—Part III." *IEEE Solid-State Circuits Mag.*, vol. 7, no. 1, pp. 10-13, Feb. 2015.
- [39] E. Vittoz, M. GR. Degrauwe, and S. Bitz, "High-performance crystal oscillator circuits: theory and application." *IEEE J. Solid-State Circuits*, vol. 23, no. 3, pp. 774-783, Jun. 1988.
- [40] P. Y. Chen, Ch. Argyropoulos, and A. Alù, "Broadening the cloaking bandwidth with non-foster metasurfaces." *Phys. Rev. Lett.*, vol. 111, no. 23, p. 233001, Dec. 2013.
- [41] P. Harpe, H. Gao, R. V. Dommele, E. Cantatore, and A. H. V. Roermund, "A 0.20 mm² 3 nW signal acquisition IC for miniature sensor nodes in 65 nm CMOS." *IEEE J. Solid-State Circuits*, vol. 51, no. 1, pp. 240-248, Jan. 2016.

- [42] J. C. Yeo, J. Yu, K. P. Loh, Z. Wang, and C. Teck Lim, "Triple-state liquid-based microfluidic tactile sensor with high flexibility, durability, and sensitivity." *ACS Sensors*, vol. 1, no. 5, pp. 543-551, Mar. 2016.
- [43] W. Song, B. Gan, T. Jiang, Y. Zhang, A. Yu, H. Yuan, N. Chen, C. Sun, and Z. L. Wang, "Nanopillar arrayed triboelectric nanogenerator as a self-powered sensitive sensor for a sleep monitoring system." *ACS Nano*, vol. 10, no. 8, pp. 8097-8103, Aug. 2016.
- [44] M. Han, X. Sh. Zhang, X. Sun, B. Meng, W. Liu, and H. Zhang, "Magnetic-assisted triboelectric nanogenerators as self-powered visualized omnidirectional tilt sensing system." *Sci. Rep.*, vol. 4, p. 4811, Apr. 2014.
- [45] P. Y. Chen, and J. Jung, "PT-Symmetry and singularity-enhanced sensing based on photoexcited graphene metasurfaces." *Phys. Rev. Appl.*, vol. 5, no. 6, p. 064018, Jun. 2016.
- [46] M. Nick, and A. Mortazawi, "Low phase-noise planar oscillators based on low-noise active resonators." *IEEE Trans. Microwave Theory Tech.*, vol. 58, no. 5, pp. 1133-1139, May. 2010.
- [47] Z. Chen, W. Hong, J. X. Chen, J. Zhou, and L. Sh. Li, "Low-phase noise oscillator utilising high-Q active resonator based on substrate integrated waveguide technique." *IET Microwaves Antennas Propag.*, vol. 8, no. 3, pp. 137-144, Feb. 2014.
- [48] H. Huang, L. Tao, F. Liu, L. Ji, Y. Hu, M. M. C. Cheng, P. Y. Chen, and D. Akinwande, "Chemical-sensitive graphene modulator with a memory effect for internet-of-things applications." *Microsystems and Nanoengineering*, Vol. 2, pp. 16018, May 2016.
- [49] M. S. Mannoer, H. Tao, J. D. Clayton, A. Sengupta, D. L. Kaplan, R. R. Naik, N. Verma, F. G. Omenetto, and M. C. McAlpine, "Graphene-based wireless bacteria detection on tooth enamel," *Nat. Communicat.*, Vol. 3, pp. 763, Mar. 2012.

VI. ULTRASENSITIVE WIRELESS DISPLACEMENT SENSING ENABLED BY PT-SYMMETRIC TELEMETRY

Parts of this chapter have been presented in (Hajizadegan et al., 2019, TAP). Copyright©2019, IEEE.

Wireless inductive sensors have been deployed in the position and displacement sensing for a wide variety of applications ranging from manufacturing processes, medical systems, automotive and aerospace industries, to civil infrastructures. Here, I propose and experimentally demonstrate an ultrasensitive wireless displacement sensing technique based on the concept of parity-time (*PT*)-symmetry or space-time reflection symmetry, first explored in quantum physics and later extended to wave physics. This *PT*-symmetric telemetric sensing system comprises an active $-RLC$ tank (stationary reader) and a passive RLC tank (movable tag), which are interrogated in a wireless manner via inductive coupling. Specifically, such a non-Hermitian electronic system obeying the *PT*-symmetry, when operated around the exceptional point (EP), can achieve drastic frequency responses and high sensitivity, well beyond the limit of conventional fully-passive wireless displacement sensors. The proposed telemetric sensing system show great potential for contactless, high-precision measurement of displacement, distance, position, and vibrations, particularly suitable for emerging industrial and healthcare internet-of-things (IoTs).

4.1 Displacement sensing systems

Displacement sensing has been a long time major demand for many industrial, medical, civil, aerospace and automotive applications [1]-[5], which require contactless, high-precision measurements of displacement, motion, position and distance of a targeted object.

Although optical methods, such as fiber laser and optical microscopic systems with a graphic interface [5], allow for high-precision dimension measurement, they typically require complex and costly modules. Moreover, the limited penetration depth of light remains hurdle for many real-world applications. For instance, animal tissues and upper layer of human skin could absorb most of infrared and visible light. In this context, radio-frequency (RF) and microwave have a longer penetration depth than that of light. A RF sensor can detect the disturbance of electromagnetic fields caused by the object motion, converting that physical parameter into an output electrical signal to indicate the position of the target. Specifically, the inductive displacement sensors (IDS) based on printed circuit board (PCB) [6]-[13], or microelectromechanical system (MEMS) techniques [14],[15] can offer a simple, low-cost and contactless method for measuring the displacement. The basic principle of a RF IDS is to employ the magnetic coupling between two coplanar or stereo inductor (L), as schematically shown in Fig. 4-1(a). In general, a RF IDS consists of two components: a stationary reader coil connected to the RF signal generator/analyzer (e.g., a vector network analyzer (VNA) or a portable RFID reader) and a movable tag coil, which is typically terminated by a resistor (R) and a capacitor (C) to form a resonant RLC tank. The mutual inductance (M) are varied when the tag physically moves with respect to the reader in normal and tangential planes, which, in turn, leads to a change in the measured reflection coefficient (S_{11}), as shown in Fig. 4-1(a). As a result, the full displacement information of the tag can be encoded in the reflection coefficient, in terms of its amplitude, phase, and resonance frequency. In contrast to those capacitive sensing techniques [15], inductive methods are less influenced by the lossy background medium (i.e., materials with complex permittivity at high frequencies), and thus the reader coils can be set at a relatively large distance apart from tags.

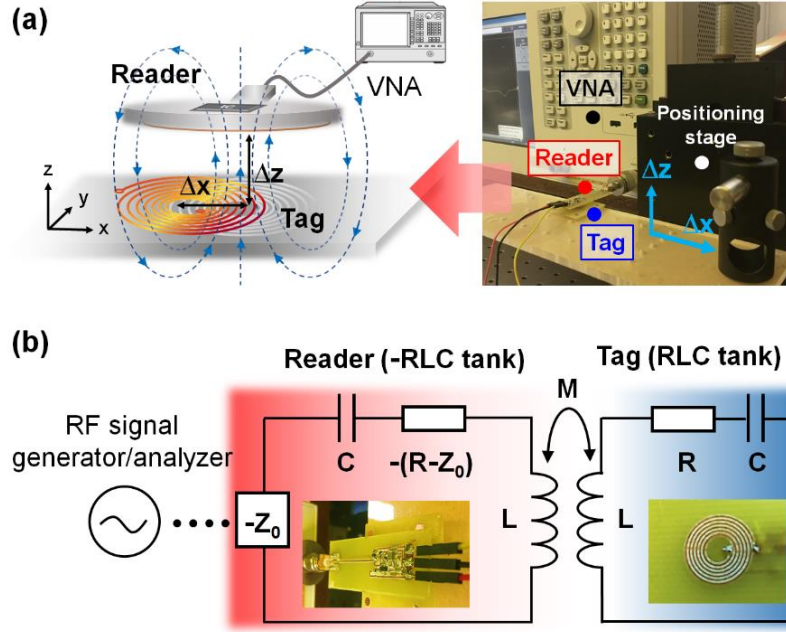


Figure 4-1 *PT*-symmetric inductive displacement sensor (IDS) system. **a** Schematics (left) and measurement setup (right) for a wireless IDS system, in which a tag (*RLC* resonant tank) is inductively coupled to a reader antenna (planar inductive coil). **b** Equivalent circuit model for the *PT*-symmetric IDS system, in which an active reader ($-RLC$ tank) is used to interrogate tags such that the circuit is invariant after spatial inversion and time reversal. In the close-loop (normal mode) analysis, a RF signal generator with source impedance Z_0 is represented by $-Z_0$, as it provides energy to excite the circuit. The inset pictures show the PCB-based prototypes for the DC-biased active reader (left) and the passive tag (right).

In this work, I propose a new *PT*-symmetric IDS telemetry system, as shown in Fig. 4-1(b), which can offer significantly improved sensitivity and resolution compared with conventional IDS systems. The concept of space-time reflection symmetry, or *PT*-symmetry, was first proposed in quantum mechanics by Bender and Boettcher in 1998 [16]. Counterintuitively, it is argued that a non-Hermitian Hamiltonian can have real eigenfrequencies, if a quantum mechanical system is invariant under operations of spatial reflection P and time reversal T [16]. Although the existence of *PT*-symmetric quantum system is still a subject to debates, *PT*-symmetry has been experimentally validated in non-Hermitian electromagnetic, optical and acoustic systems, thanks

to the formal similarities between the Schrödinger and Helmholtz equations [17]-[31]. These PT -symmetric wave systems are usually realized by introducing spatial distribution of balanced gain-loss profiles. At RF and microwave frequencies, a PT -symmetric system can be readily realized with transmission-line networks or lumped-element circuits [32]-[34] described by the telegraph equation. At low frequencies, the gain medium can be achieved with active components, such as operational amplifiers and negative resistance converters (NRCs). For example, a PT -symmetric electronic system can be made by pairing the $-RLC$ and RLC tanks, which are correspondingly responsible for the amplification and attenuation of the RF signal. The contactless interaction between active and passive tanks can be performed through capacitive coupling, inductive coupling, or both [32],[35]. PT -symmetric and non-Hermitian systems exhibit many exotic and anomalous spectral properties and dynamical features. Of particular interest is the exceptional point that leads to drastic eigenfrequency bifurcation and phase transitions, which have been utilized to build ultrasensitive optical sensors based on microcavity or metamaterial structures [36]-[40], with spatially varying gain-loss profiles. Inspired by previous works done in the optical domain, I present here a PT -symmetric electronic circuit and its practical application in high-sensitivity wireless displacement and motion sensing. Figure 4-1(b) shows the equivalent circuit of the PT -symmetric IDS system, which consists of a passive tag (RLC circuit) inductively coupled to an active reader ($-RLC$ circuit). In this scenario, the whole telemetry system fulfills the spatial-inversion and time-reversal symmetry, as demonstrated below. In the following, I will investigate both theoretically and experimentally the performance improvement and critical operating conditions of the PT -symmetric IDS system in Fig. 4-1(b), with laboratory prototypes designed and fabricated by the low-cost PCB technique.

4.2 PT-Symmetric Telemetry

Figure 4-1 shows the photograph and the equivalent circuit of the *PT*-symmetric RF IDS system: the reader ($-RLC$ tank) is stationary and connected to the VNA, whereas the tag (RLC tank) is placed on a movable stage whose normal displacement Δz and tangential displacement Δx (or Δy) can be controlled precisely by the XYZ-positioning stage. In the closed-loop (normal-mode) analysis, the VNA, which contains RF signal generator (energy source) to excite the circuit, should be modeled as a negative generator impedance $-Z_0$, where Z_0 is its source impedance [Pozar]. For balancing gain and loss in the system, the $-RLC$ -reader connected to the VNA should use a NRC with an equivalent resistance of $-(R-Z_0)$. Applying Kirchhoff's laws to the equivalent circuit in Fig. 4-1(b) leads to the Liouvillian formalism as [32]:

$$\frac{d\Phi}{d\tau} = \mathcal{L}\Phi; \quad \mathcal{L} = \begin{pmatrix} 0 & 0 & 1 & 0 \\ 0 & 0 & 0 & 1 \\ -\frac{1}{1-\kappa^2} & \frac{\kappa}{1-\kappa^2} & \frac{1}{\gamma(1-\kappa^2)} & \frac{\kappa}{\gamma(1-\kappa^2)} \\ \frac{\kappa}{1-\kappa^2} & -\frac{1}{1-\kappa^2} & -\frac{\kappa}{\gamma(1-\kappa^2)} & -\frac{1}{\gamma(1-\kappa^2)} \end{pmatrix}, \quad (4-1)$$

where $\Phi \equiv (q_1, q_2, \dot{q}_1, \dot{q}_2)^T$, q_1 and q_2 are charges stored on the capacitor in the amplifying and attenuating tanks, $\tau \equiv \omega_0 t$, $\omega_0 = 1/\sqrt{LC}$ is the natural frequency of an RLC tank, $\gamma = R^{-1}\sqrt{L/C} = |-R|^{-1}\sqrt{L/C}$ is the dimensionless gain-loss parameter or the non-Hermiticity parameter, and $\kappa = M/L$ is the coupling strength between the $-RLC$ and RLC tanks; here all frequencies are measured in units of ω_0 . The effective Hamiltonian can be expressed as $H_{\text{eff}} = i\mathcal{L}$ [32], which takes a non-Hermitian form and is symmetric with respect to generalized PT

transformations: $\mathcal{P} = \begin{pmatrix} \sigma_x & 0 \\ 0 & \sigma_x \end{pmatrix}$, $\mathcal{T} = \begin{pmatrix} \mathbf{I} & 0 \\ 0 & -\mathbf{I} \end{pmatrix} \mathcal{K}$ [32], where σ_x is the Pauli matrix, \mathbf{I} is an 2×2

identity matrix, and \mathcal{K} conducts the operation of complex conjugation. Here, I find that H_{eff} commutes with PT, i.e., $[\mathcal{PT}, H_{eff}] = 0$, and thus H_{eff} shares the same eigenbasis with the parity-time operator PT [32]. After the substitution of time-harmonic charge distributions $q_n = A_n e^{j\omega t}$, eigenfrequencies for this PT -symmetric electronic system, as a function of the non-Hermiticity parameter γ and the coupling strength κ , can be derived as:

$$\omega_{1,2,3,4} = \pm \omega_0 \sqrt{\frac{2\gamma^2 - 1 \pm \sqrt{1 - 4\gamma^2 + 4\gamma^4 \kappa^2}}{2\gamma^2(1 - \kappa^2)}}. \quad (4-2)$$

Although there are four normal modes, there is redundancy and only two distinct modes are necessarily considered, since positive and negative eigenfrequencies of equal magnitude are essentially identical.

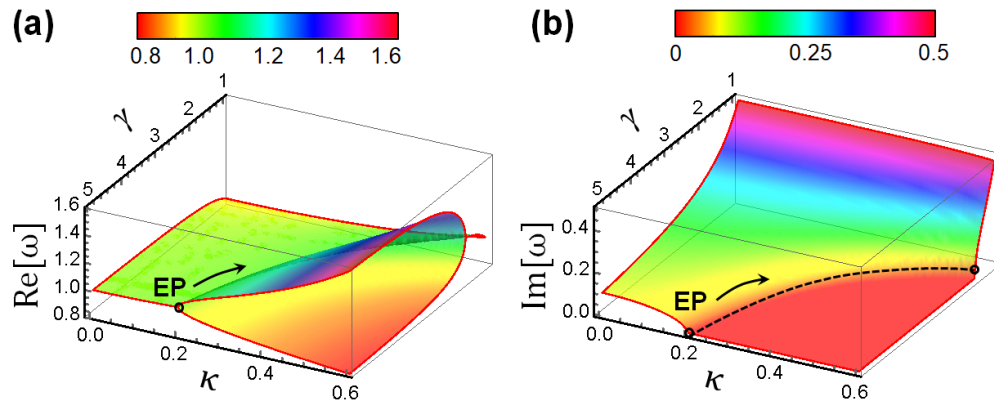


Figure 4-2 Complex eigenfrequency of PT -symmetric electronic system. Contours of **a** real and **b** imaginary eigenfrequency as a function of the non-Hermiticity parameter γ and the coupling coefficient κ for the PT -symmetric RF circuit in Fig. 4-1b.

For a given value of γ , the $\omega - \kappa$ relationship shows two distinct regimes of behavior, depending on the value of κ , as shown in Fig. 4-2. In the parametric region $\kappa > \kappa_{EP}$, the eigenfrequencies are purely real ($\omega \in \mathbb{R}$) and $\mathcal{PT}\Phi = \Phi$, so-called the *exact PT*-symmetric phase. The motion in this exact *PT*-symmetric phase is oscillatory at the two eigenfrequencies, resulting in two resonant dips in the reflection spectrum. At the exceptional point κ_{EP} , eigenfrequencies undergo a bifurcation process and branch out into the complex plane. The exceptional point between two *PT* phases is given by:

$$\kappa_{EP} = \frac{1}{\gamma} \sqrt{1 - \frac{1}{4\gamma^2}}. \quad (4-3)$$

The region where $\kappa < \kappa_{EP}$ is known as the *broken PT*-symmetric phase. In such a weak coupling region, eigenfrequencies become two complex conjugate pairs ($\omega \in \mathbb{C}$) and $\mathcal{PT}\Phi \neq \Phi$, indicating that the *PT*-symmetry is broken. It is particularly interesting to note that nearby the exceptional point, the drastically bifurcating eigenfrequencies with respect to the perturbation of κ [Fig. 4-2] can be used to make an ultrasensitive wireless displacement sensor (κ is varied by the relative distance between two coil inductors).

For a specific value of κ , there exists similar phase transitions under the perturbation of γ , and the exception point is given by:

$$\gamma_{EP} = \frac{1}{\kappa} \sqrt{\frac{1 + \sqrt{1 - \kappa^2}}{2}}.$$

(4-4)

The dramatically bifurcating eigenfrequencies (resonance frequency splitting) around γ_{EP} [Fig. 4-2] may be of interest for the wireless reactive and resistive sensing. In these applications, the passive wireless sensor described by a *RLC* tank has either a variable capacitor (e.g., capacitive pressure sensor [35],[41]) or a variable resistor (e.g., chemiresistor sensor [42]) such that γ can be tuned by the physical/chemical parameter to be sensed (i.e., $\gamma \propto R^{-1}C^{-1/2}$). When the sensor is operated around γ_{EP} , the bifurcation effect is expected to boost the sensitivity associated with the resonance frequency shift.

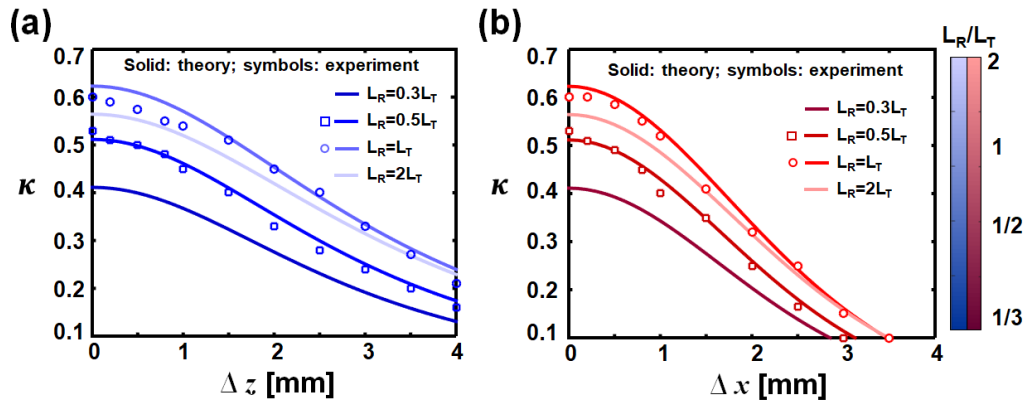


Figure 4-3 Effect of normal and tangential displacement on the (inductive) coupling coefficient K . (a,b) Calculated coupling coefficient versus normal displacement Δz and tangential displacement Δx ; here, the inductance ratio between the reader coil and the tag coil, L_R/L_T , is also varied.

In our IDS telemetry experiments, a planar microstrip spiral inductor is used for both reader and tag. According to Neumann's formula [43], the mutual induction between two spiral inductors is given by:

$$M = \rho \sum_{i=1}^{N_R} \sum_{j=1}^{N_S} M_{ij}, \quad (4-5a)$$

$$M_{ij} = \frac{\mu_0}{4\pi} \int_{C_i} \int_{C_j} \frac{1}{|R_{ij}|} d\vec{l}_i \cdot d\vec{l}_j \approx \frac{\mu_0 \pi a_i^2 b_j^2}{2(a_i^2 + b_j^2 + z^2)^{3/2}}, \quad (4-5b)$$

where M_{ij} is the mutual inductance between two loops, i (j) represents the i -th (j -th) loop of the coil on the sensor (tag), $a_i = r_{o,R} - (N_i - 1)(w_R + s_R) - w_R / 2$, $b_j = r_{o,T} - (N_j - 1)(w_T + s_T) - w_T / 2$, N_i (N_j) is the number of turns in the sensor (tag), R_{ij} represents the distance between filamentary metal lines, ρ is the shape factor of planar coil (here $\rho = 1$ for planar circular-shape coil) [43], μ_0 is the free-space permeability, w and s are width and spacing of copper microstrip lines, z is the central distance between two coils, r_o is the outer radius of the coil, and the subscript R (T) represents the sensor (tag). The mutual inductance depends on both tangential (x - y plane) and normal (x - z plane) displacements of the tag, which determine the value of M_{ij} . Figures 3(a) and 3(b) report the calculated coupling coefficient versus normal and tangential displacements, Δx and Δz ; here, the inductance ratio between the reader and tag coils, L_R/L_T is also varied. The mutual inductance or the inductive coupling coefficient, κ , reaches a maximum value when two spiral coils are perfectly aligned (i.e., $\Delta x=0$), and κ decreases with increasing Δx . Similarly, κ decreases with increasing Δz . As a result, the information of displacement can be encoded in the inductive coupling strength, determining the reflection coefficient measured by the VNA.

4.3 Experimental Demonstration of PT-Symmetric IDS System.

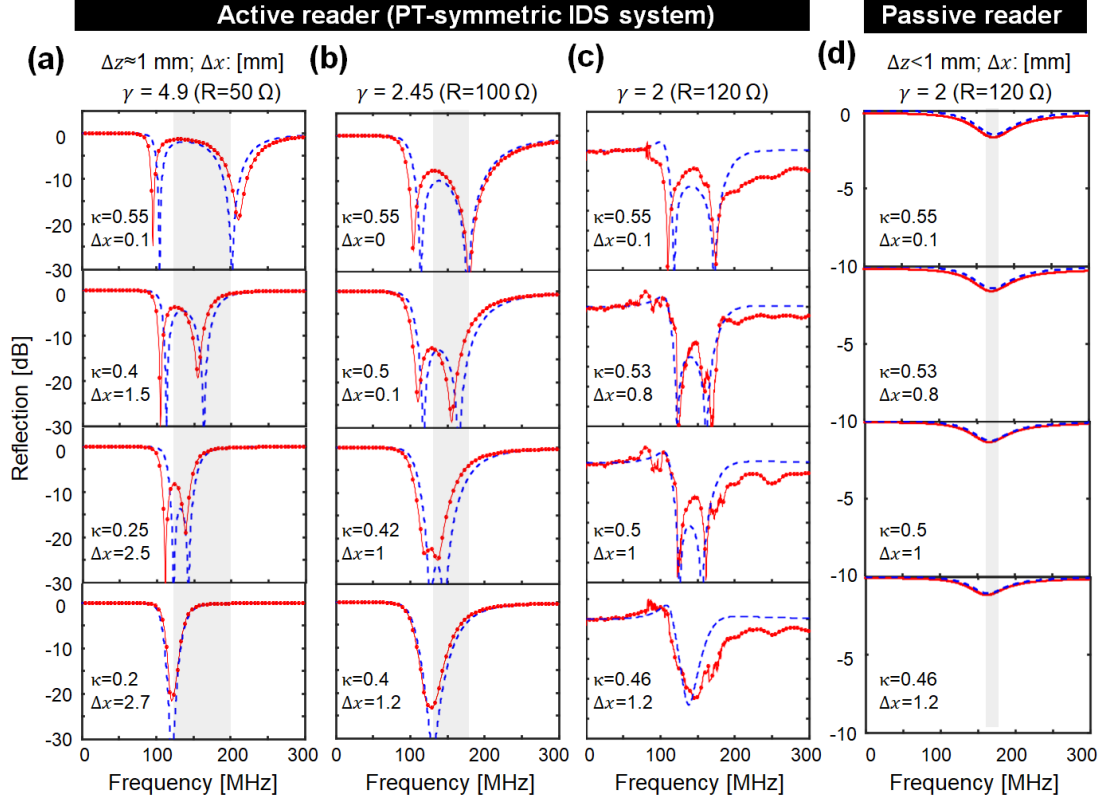


Figure 4-4 Reflection spectra for *PT*-symmetric and conventional (fully-passive) displacement sensors, under different values of Δx (tangential displacement). The reflection coefficient versus frequency for the *PT*-symmetric IDS systems with **a** $\gamma = 4.9$, **b** $\gamma = 2.45$ and **c** $\gamma = 2$, and for **d** the conventional passive IDS system using a coil-antenna reader to read the same tag as (c); here, solid and dashed lines represent experimental and analytical results, respectively. When a tangential displacement is introduced, the coupling strength between the reader and tag coils is also varied, which in turn leads to a shift in the resonance frequency. I note that results on the bottom panel of (a) and (b) are obtained for systems operated close to the exceptional point, whereas the result on the bottom panel of (c) designates the broken symmetry phase, with resonance becomes progressively weaker as κ decreases (or Δx increases).

The PT -symmetric inductive displacement sensing was tested using the PCB-based prototypes shown in Figure 4-1(b). For both $-RLC$ -reader and RLC -tag, their effective inductance and capacitance are fixed as: $L = 0.3 \mu\text{H}$ (planar spiral coil) and $C = 5 \text{ pF}$. The passive tag is loaded with a resistor (MNR02JR-0402), whose resistance value and tolerance are $R = 50/100/120 \pm 0.5\% \Omega$. The active reader has a Colpitts-type NRC, which gives a voltage-controlled equivalent negative resistance in the frequency range of interest [44],[45]. Details of the NRC design can be found in Ref. [ref]. Figure 4-4 reports the reflection coefficient versus the inductive coupling strength for the PT -symmetric IDS systems, with (a) $\gamma = 4.9$ ($R = 50 \Omega$), (b) $\gamma = 2.45$ ($R = 100 \Omega$), and (c) $\gamma = 2$ ($R = 120 \Omega$); here, κ is tuned through the tag's tangential displacement Δx [Fig. 4-3(b)]. It is seen from Fig. 4-4 that theoretical (dashed lines) and measurements (solid lines) results are in excellent agreement. For making a fair comparison, Fig. 4-4(d) reports the reflection spectra for the conventional IDS system, in which a coil antenna (which is identical to the planar spiral coil used in the PT systems) was used to interrogate the same RLC -tag in Fig. 4-4(c) ($\gamma = 2$ and $R = 120 \Omega$). It is clearly seen from Figure 4-4 that under the same magnitude of inductive coupling, the PT -symmetric IDS system [Figures 4(a)-(c)] can exhibit significantly greater sensitivity (resonance frequency shift) than the conventional passive one [Figure 4-4(d)], thanks to the largely bifurcating eigenfrequencies at the exceptional point. In addition, in the exact PT -symmetric phase where $\kappa > \kappa_{EP}$, real eigenfrequencies yield high- Q resonances and two sharp, narrowband reflection dips, ideally suitable for highly-resolution and noise-immune sensing. On the other hand, in the broken PT -symmetric phase where $\kappa < \kappa_{EP}$ (e.g., the bottom panels of Fig. 4-4(c)), complex eigenfrequencies result in a weak and broad resonance with a much reduced Q -factor. Hence, the broken symmetry phase is not suitable for sensing and detection applications.

The above observations can be understood in terms of energy flow: if the coupling strength is weak, the energy in the active $-RLC$ tank cannot flow fast enough into the passive RLC tank for compensating the absorption (loss), resulting in a non-equilibrium system with complex-valued eigenfrequencies. If the coupling strength exceeds a certain threshold K_{EP} , the system can reach equilibrium, since the energy in the active tank can flow fast enough into the passive one for compensating its power dissipations. As can be seen in Fig. 4-2, at a larger K , the critical γ for the phase transition (γ_{EP}) can be reduced, and vice versa. I should point out that the linewidth sharpening or Q -factor enhancement, of importance for telemetric sensors, is also due to power compensation between the two tank circuits. Unlike the conventional loss-compensated filters and resonators [44], Q -factor enhancement is achieved by electrically disconnected gain and loss, which interact through the magnetic coupling.

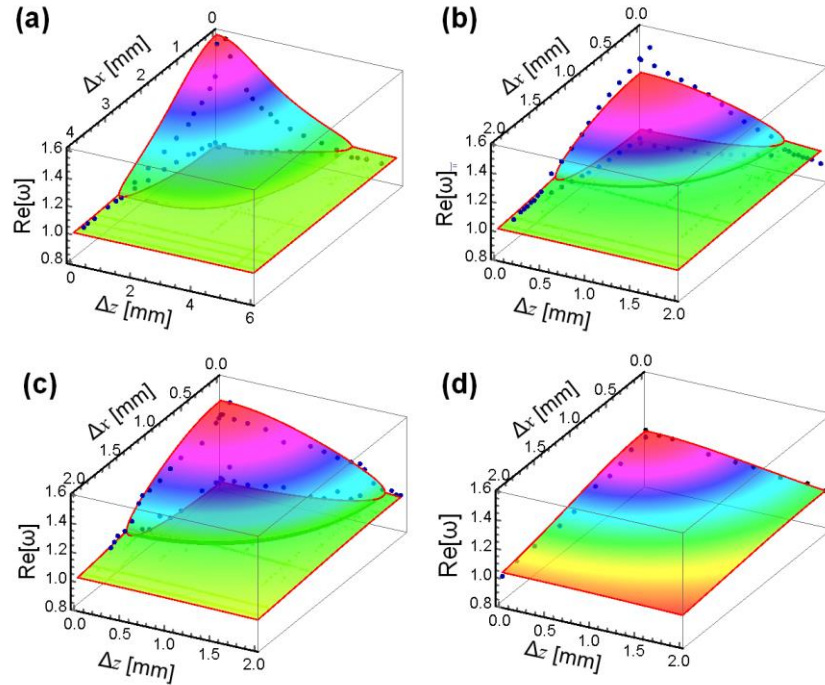


Figure 4-5 Evolution of the eigenfrequency for PT -symmetric and conventional (fully-passive) IDS systems. Contours of real part of eigenfrequency as a function of Δx and Δz for the PT -symmetric IDS systems with **a** $\gamma = 4.9$, **b** $\gamma = 2.45$ and **c** $\gamma = 2$, and for **d** the conventional fully-passive IDS system using

a coil-antenna reader to read the same tag as (c); here, colored surface and dots represent theoretical and experimental results, respectively.

Figure 4-5 shows the contour of real eigenfrequency $\text{Re}[\omega]$ as a function of Δx and Δz [Eq. (4-5)], where (a)-(d) correspond to the IDS telemetry systems in Figs. 4-4(a)-(d). Here, I found a good agreement between theoretical and measurement results, respectively represented by color surfaces and dots. The sensitivity improvement due to the singularity raised by the exceptional point can be better understood with the help of Fig. 4-5. It is clearly seen from Figs. 4-5(a)-(c) that the bifurcation effect can drastically shift the resonance frequencies with respect to κ , or, equivalently, Δx and Δz perturbations. I found that the evolution of the resonance response of the *PT*-symmetric IDS system clearly identifies the eigenfrequency transition predicted by Eq. (4-3), further validating our theoretical hypothesis. For the fully-passive IDS system in Fig. 4-5(d), the exceptional point and the bifurcation effect disappear. Instead, a rather flat contour of $\text{Re}[\omega]$ is obtained, implying a relatively poor sensitivity due to a small resonance frequency shift. Moreover, given by the complex-valued eigenfrequency [Fig. 4-5(d)], the conventional IDS system displays a weak, low- Q resonance, leading to low spectral resolution and small modulation depth. Comparing the active *PT*-symmetric IDS system [Figs. 5(a)-(c)] and the conventional one [Fig. 4-5(d)], one may conclude that the *PT*-symmetric design can, indeed, provide more sensitive frequency response and thus greater sensitivity in measuring the normal and tangential motions of a wireless tag.

Finally, I note that the *PT*-symmetric IDS system based on the PCB prototypes already offers a sub-millimeter scale motion detection, as can be seen from Fig. 4-4. The detection limit can be

further pushed down to micrometer scale by using the MEMS technology. It is also worth mentioning that in the PT -symmetric system, the critical coupling strength κ_{EP} can be reduced by increasing the non-Hermiticity parameter γ (or the intrinsic Q -factor of the tag) [Eq. (4-3)], as can be seen in Figs. 4-4(a)-(c). The increment in γ can be done by, for example, reducing the R and $-R$ in the tag and the reader. A lower κ_{EP} also leads to a more dramatic bifurcation effect and greater sensitivity enhancement, as well as an increased range for effective detection of displacement. However, for an extremely miniaturized micromachined tag, γ is typically quite small because L is limited by the small area and R is quite large due to the skin effect, Eddy currents, and dielectric losses in the background medium. As a result, the maximum value of γ has its physical limitation, and there is a compromise between the size miniaturization of tag/reader and the sensing performance.

4.5 Conclusions

We outline a new paradigm of PT -symmetric wireless displacement and alignment sensors. I have theoretically studied and experimentally validated that the PT -symmetric IDS system based on an active telemetry can offer significantly higher sensitivity, sensing resolution and modulation depth, when compared with conventional fully-passive ones. The improvement in sensing performance can be ascribed to the bifurcation effect (resonance frequency splitting) nearby the exceptional point of the PT -symmetric physical system. Around such a singular point, even a small change in the inductive coupling strength, caused by motion and displacement of a targeted object, can lead to significantly shifted resonance frequencies that can be readily detected in the reflection spectrum. Our findings may have an impact on many

compact wireless displacement and proximity sensors, which will become ubiquitous in the industrial IoTs, manufacturing operations, intellectual civil infrastructures, healthcare systems, and even cyber-physical and humanoid robotic applications.

REFERENCES

- [1] Xi, Z., Wei, L., Adam, A.J.L., Urbach, H.P. and Du, L., “Accurate feeding of nanoantenna by singular optics for nanoscale translational and rotational displacement sensing.” *Phys. Rev. Lett.* **117**, 113903 (2016).
- [2] Park, J.W., Sim, S.H. and Jung, H.J., “Wireless displacement sensing system for bridges using multi-sensor fusion.” *Smart Mater. Struct.* **23**, 045022 (2014).
- [3] Paggi, C., Occhiuzzi, C. and Marrocco, G., “Sub-millimeter displacement sensing by passive UHF RFID antennas.” *IEEE Trans. Antennas Propag.* **62**, 905-912 (2014).
- [4] Di Sante, R., “Fibre optic sensors for structural health monitoring of aircraft composite structures: Recent advances and applications.” *Sensors* **15**, 18666-18713 (2015).
- [5] Barrias, A., Casas, J.R. and Villalba, S., “A review of distributed optical fiber sensors for civil engineering applications.” *Sensors* **16**, 748 (2016).
- [6] Fericean, S., and Droxler, R., “New noncontacting inductive analog proximity and inductive linear displacement sensors for industrial automation.” *IEEE Sens. J.* **7**, 1538-1545 (2007).
- [7] Damnjanovic, M. S., Zivanov, L. D., Nagy, L. F., Djuric, S. M., and Biberdzic, B. N., “A novel approach to extending the linearity range of displacement inductive sensor.” *IEEE Trans. Magn.* **44**, 4123-4126 (2008).
- [8] George, B., Zangl, H., Bretterkieber, Th., and Brasseur, G., “A combined inductive–capacitive proximity sensor for seat occupancy detection.” *IEEE Trans. Instrum. Meas.* **59**, 1463-1470 (2010).
- [9] Djuric, S. M., “Performance analysis of a planar displacement sensor with inductive spiral coils.” *IEEE Trans. Magn.* **50**, 1-4 (2014)

- [10] Tang, Q., Peng, D., Wu, L., and Chen, X., “An inductive angular displacement sensor based on planar coil and contrate rotor.” *IEEE Sens. J.* **15**, 3947-3954 (2015).
- [11] Jeranče, N., Vasiljević, D., Samardžić, N., and Stojanović, G., “A compact inductive position sensor made by inkjet printing technology on a flexible substrate.” *Sensors* **12**, 1288-1298, (2012).
- [12] Babkovic, K., Damnjanovic, M., Nagy, L., Kisic, M., and Stojanovic, G., “Inductive displacement sensor of novel design printed on polyimide foil.” *IEEE Trans. Magn.* **53**, 1-5 (2017).
- [13] Ding, X., Chen, X., Ma, W., Chen, X., and Li, N., “A novel PQCR-L circuit for inductive sensing and its application in displacement detection.” *IEEE Trans. Instrum. Meas.* **65**, 685-693 (2016).
- [14] Velten, Th., Stefan, D., and Obermeier, E., “Micro-coil with movable core for application in an inductive displacement sensor.” *J. Micromech. Microeng.* **9**, 119 (1999).
- [15] Tseng, V.F.G., and Xie, H., “Resonant inductive coupling-based piston position sensing mechanism for large vertical displacement micromirrors.” *J. Microelectromech. Syst.* **25**, 207-216 (2016).
- [16] Bender, C.M., and Boettcher, S., “Real spectra in non-Hermitian Hamiltonians having P T symmetry.” *Phys. Rev. Lett.* **80**, 5243 (1998).
- [17] Makris, K.G., El-Ganainy, R., Christodoulides, D.N., and Musslimani, Z.H., “Beam dynamics in PT symmetric optical lattices.” *Phys. Rev. Lett.* **100**, 103904 (2008).
- [18] Rüter, Ch.E., et al. “Observation of parity–time symmetry in optics.” *Nat. Phys.* **6**, 192-195 (2010).
- [19] Regensburger, A., et al. “Parity-time synthetic photonic lattices.” *Nature* **488**, 167-171 (2012).
- [20] Lin, Z., et al. “Unidirectional invisibility induced by PT-symmetric periodic structures.” *Phys. Rev. Lett.* **106**, 213901 (2011).
- [21] Mostafazadeh, A., “Invisibility and PT symmetry.” *Phys. Rev. A* **87**, 012103 (2013).

- [22] Longhi, S., “PT-symmetric laser absorber.” *Phys. Rev. A* **82**, 031801 (2010).
- [23] Chong, Y.D., Ge, L., and Stone, A.D., “PT-Symmetry breaking and laser-absorber modes in optical scattering systems.” *Phys. Rev. Lett.* **106**, 093902 (2011).
- [24] Feng, L., Wong, Z.J., Ma, R.M., Wang, Y., and Zhang, X., “Single-mode laser by parity-time symmetry breaking.” *Science* **346**, 972-975 (2014).
- [25] Hodaei, H., Miri, M.A., Heinrich, M., Christodoulides, D.N., and Khajavikhan, M., “Parity-time–symmetric microring lasers.” *Science* **346**, 975-978 (2014).
- [26] Wong, Z.J., et al. “Lasing and anti-lasing in a single cavity.” *Nat. Photonics* **10**, 796-801 (2016).
- [27] Lee, J.M., et al. “Reconfigurable directional lasing modes in cavities with generalized PT Symmetry.” *Phys. Rev. Lett.* **112**, 253902 (2014).
- [28] Peng, B., et al. “Parity–time-symmetric whispering-gallery microcavities.” *Nat. Phys.* **10**, 394-398 (2014).
- [29] Ramezani, H., Kottos, T., El-Ganainy, R., and Christodoulides, D.N., “Unidirectional nonlinear PT-symmetric optical structures.” *Phys. Rev. A* **82**, 043803 (2010).
- [30] Chang, L., et al. “Parity-time symmetry and variable optical isolation in active-passive-coupled microresonators.” *Nat. Photonics* **8**, 524-529 (2014).
- [31] Fleury, R., Sounas, D., and Alù, A., “An invisible acoustic sensor based on parity-time symmetry.” *Nat. Communicat.* **6**, (2015).
- [32] Schindler, J., Li, A., Zheng, M.C., Ellis, F.M., and Kottos, T., “Experimental study of active LRC circuits with PT symmetries.” *Phys. Rev. A* **84**, 040101 (2011).
- [33] Schindler, J., et al. “PT-symmetric electronics.” *J. Phys. A: Math. Theor.* **45**, 444029 (2012).
- [34] Bender, N., et al. “Observation of asymmetric transport in structures with active nonlinearities.” *Phys. Rev. Lett.* **110**, 234101 (2013).

- [35] Chen, P.Y., et al. "Generalize parity-time symmetry condition for enhanced sensor telemetry." *Nat. Electron.* , In press.
- [36] Wiersig, J., "Sensors operating at exceptional points: General theory." *Phys. Rev. A* **93**, 033809 (2016).
- [37] Chen, P.Y., and Jung, J., "PT-Symmetry and singularity-enhanced sensing based on photoexcited graphene metasurfaces." *Phys. Rev. Appl.* **5**, 064018 (2016).
- [38] Sakhdari, N., Farhat, M., and Chen, P.Y., "PT-symmetric metasurfaces: wave manipulation and sensing using singular points." *New J. Phys.* **19**, 065002 (2017).
- [39] Liu, Z.P., et al. "Metrology with PT-symmetric cavities: Enhanced sensitivity near the PT-phase transition." *Phys. Rev. Lett.* **117**, 110802 (2016).
- [40] Chen, W., Özdemir, Ş.K., Zhao, G., Wiersig, J., and Yang, L., "Exceptional points enhance sensing in an optical microcavity." *Nature* **548**, 192–196 (2017).
- [41] Hodaei, H., et al. "Enhanced sensitivity at higher-order exceptional points." *Nature* **548**, 187–191 (2017).
- [42] Chen, P.J., Rodger, D.C., Saati, S., Humayun, M.S., and Tai, Y.C., "Microfabricated implantable parylene-based wireless passive intraocular pressure sensors." *J. Microelectromech. Syst.* **17**, 1342-1351 (2008).
- [43] Yao, M. S., Tang, W. X., Wang, G., Nath, B., and Xu, G., "MOF thin film- coated metal oxide nanowire array: significantly improved chemiresistor sensor performance." *Adv. Mater.* **28**, 5229-5234 (2016).
- [44] Raju, S., Wu, R., Chan, M., and Yue, C.P., "Modeling of mutual coupling between planar inductors in wireless power applications," *IEEE Trans. Power Electron.* **29**, 481-490 (2014).
- [45] Yazgi, M., Toker, A., and Virdee, B. S., "A new negative resistance circuit and an application for loss compensation in a distributed amplifier." *Ana. Int. Cir. Sig. Process.*, vol. **60**, 215-220, 2009.
- [46] Razavi, B., *RF microelectronics*, vol. **1**, New Jersey: Prentice Hall, 1998.

CHAPTER 5: ULTRA-SENSITIVITY WITH DIVERGENT EXCEPTIONAL POINTS FOR RADIO-FREQUENCY TELEMETRY

Parts of this chapter have been presented in (Sakhdari et al., 2019, PRL). Copyright©2019, PRL.

Standard Exceptional points (EPs) are non-Hermitian degeneracies that occur in open systems. Their existence features a singularity marked by the failure of Taylor series representation. Here, I theoretically introduce and experimentally demonstrate a new class of parity-time (*PT*) symmetric electronic oscillators that combine EPs with another type of mathematical singularity associated with poles of complex functions. These “divergent” exceptional points (DEPs) can exhibit unprecedentedly a large eigenvalue bifurcation beyond those obtained by standard EPs. Our results pave the way for building a new generation of telemetering and sensing devices with superior performance.

5.1 *PT*-symmetry and divergent exceptional points (DEPs)

Parity-time (*PT*) symmetry in optics and photonics [1] has been a subject of intense investigations with several potential applications in building new types of optical diodes [2], microlasers[3],[4], sensors [5],[6] and nonlinear light sources [7]-[10]. A central notion to the physics of *PT* symmetry is exceptional points (EPs), which mark the onset of *PT* spontaneous symmetry breaking, i.e. the transition from an exact *PT* phase to a broken phase[11],[12]. EPs have been associated with some of the most intriguing features of *PT*-symmetric (and, in general, non-Hermitian) wave dynamics, such as unidirectional invisibility[13]–[15], laser self-termination[16]–[19] and chirality [20],[21], to just mention few examples.

Essentially, EPs arise in the spectrum of non-Hermitian systems and represent a special type of degeneracy, where the eigenvalues and their corresponding eigenvectors coalesce. Mathematically, they are singular points, at which the associated characteristic equation fails to have a Taylor series representation [22].

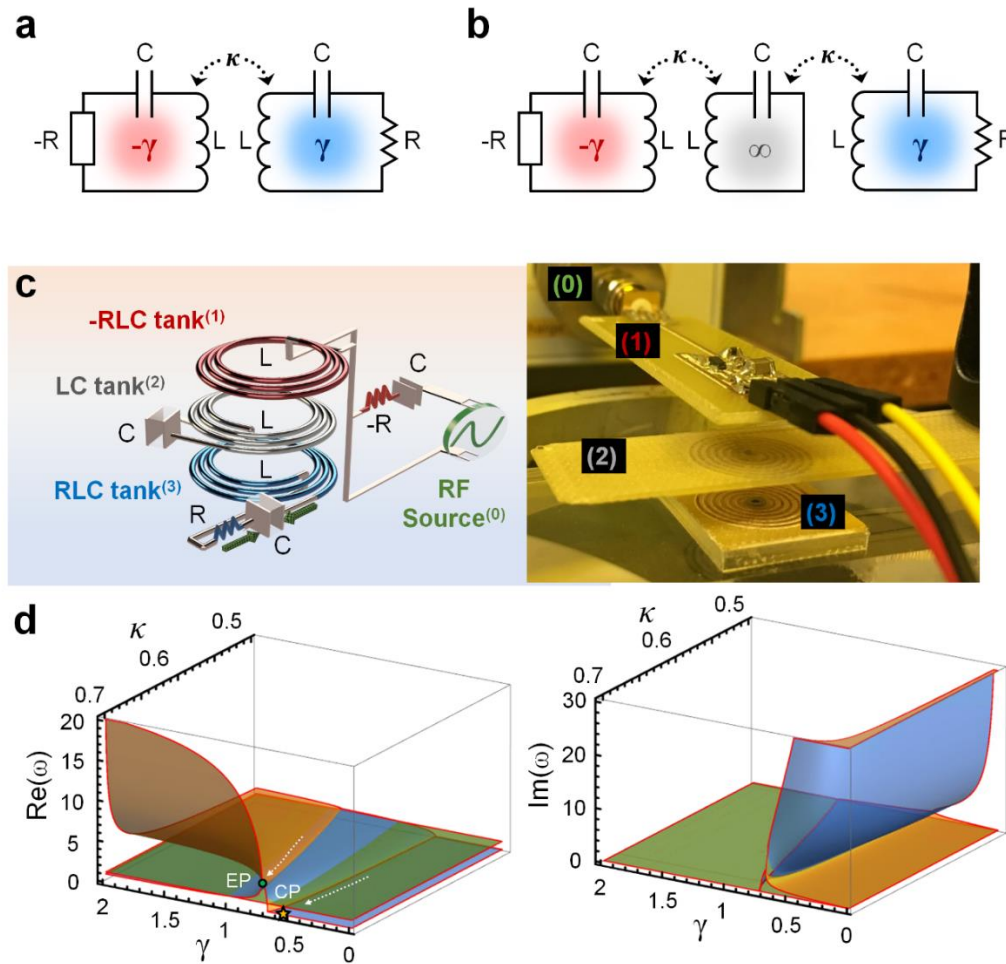


Figure 5-1 Non-Hermitian PT -symmetric telemetric electronic systems. (a, b) Schematics of (a) the standard PT -symmetric telemetric system and (b) the three-elements PT -symmetric system formed by electronic oscillators. (c) Experimental setup of the three-elements PT -symmetric telemetric system. (d) Evolution of complex eigenfrequencies as a function of the non-Hermiticity parameter γ and the coupling strength κ for the third-order PT -symmetric system in b and c. Here, the system's exceptional point (EP) and critical point (CP) are highlighted.

Besides optics, another important platform where PT symmetry and EPs were experimentally investigated is electronics²³. Within the realm of electronics, coupled RLC and $-RLC$ oscillators (Fig. 5-1a) are used to implement a discrete Hamiltonian that obeys PT symmetry and exhibits a transition between the exact and broken phases. Recently, applications of PT -symmetric electronics in wireless power transfer [24] and sensor telemetry [25] have been proposed and experimentally demonstrated. In all the previous work (both in optics and electronics), the studied systems involved only the standard EP described above. Here, I introduce the notion of divergent exceptional points (DEPs) and experimentally demonstrate their feasibility in telemetry applications. Particularly, I show that multi-element PT -symmetric electronic systems can be engineered to exhibit a unique spectral feature, namely a standard EP in the vicinity of a pole singularity, which I denote as a divergent EP (or DEP). Importantly, I show that the eigenvalue bifurcation associated with a DEP is much stronger than the case with a standard EP, thereby paving the way towards building ultra-responsive sensors with superior performance beyond what reported so far [25].

5.2 Divergent exceptional points in PT -symmetric electronic circuit

To this end, I consider a PT -symmetric electronic circuit that consists of three different coupled oscillators (see Figs. 5-1b and 5-1c): $-RLC$, LC and RLC (we also extend this analysis to N -elements in section 5.5). By applying the Kirchhoff's circuit laws as expressed using the Liouvillian formalism²³, I obtain:

$$\mathcal{L}\Psi = \frac{d\Psi}{d\tau},$$

$$\mathcal{L} = \begin{pmatrix} 0 & 0 & 0 & 1 & 0 & 0 \\ 0 & 0 & 0 & 0 & 1 & 0 \\ 0 & 0 & 0 & 0 & 0 & 1 \\ -\frac{1-\kappa^2}{1-2\kappa^2} & \frac{\kappa}{1-2\kappa^2} & -\frac{\kappa^2}{1-2\kappa^2} & \frac{1}{\gamma} \frac{1-\kappa^2}{1-2\kappa^2} & 0 & -\frac{1}{\gamma} \frac{\kappa^2}{1-2\kappa^2} \\ \frac{\kappa}{1-2\kappa^2} & -\frac{1}{1-2\kappa^2} & \frac{\kappa}{1-2\kappa^2} & -\frac{1}{\gamma} \frac{\kappa}{1-2\kappa^2} & 0 & \frac{1}{\gamma} \frac{\kappa}{1-2\kappa^2} \\ -\frac{\kappa^2}{1-2\kappa^2} & \frac{\kappa}{1-2\kappa^2} & -\frac{1-\kappa^2}{1-2\kappa^2} & \frac{1}{\gamma} \frac{\kappa^2}{1-2\kappa^2} & 0 & -\frac{1}{\gamma} \frac{1-\kappa^2}{1-2\kappa^2} \end{pmatrix}, \quad (5-1)$$

where $\Psi \equiv (q_1, q_2, q_3, \dot{q}_1, \dot{q}_2, \dot{q}_3)^T$, q_1 , q_2 , and q_3 are charges stored on the capacitor in the $-RLC$, LC , and RLC tanks, $\gamma = R^{-1}\sqrt{L/C}$ is the non-Hermiticity parameter (note that positive and negative γ respectively play the role of gain and loss), $\kappa = M/L$ is the normalized coupling strength ($0 \leq \kappa \leq 1$) and M is the mutual inductance between two neighboring electronic oscillators. Additionally, $\tau \equiv \omega_0 t$, $\omega_0 = 1/\sqrt{LC}$ is the natural frequency of the isolated neutral LC tank, and all frequencies are measured in units of ω_0 . From Eq. (5-1), I find that the Liouvillian expression remains the same under the combined parity P ($q_1 \leftrightarrow q_3$) and time-reversal T ($t \rightarrow -t$) transformation. Moreover, the effective Hamiltonian can be defined as $H_{eff} = i\mathcal{L}$, which is non-Hermitian ($H_{eff}^\dagger \neq H_{eff}$) and symmetric with respect to the PT transformation, i.e., $[PT, H_{eff}] = 0$, with

$$P = \begin{pmatrix} \mathbf{J} & 0 \\ 0 & \mathbf{J} \end{pmatrix}, \quad (5-2a)$$

$$\mathcal{T} = \begin{pmatrix} \mathbf{T} & 0 \\ 0 & \mathbf{T}' \end{pmatrix}, \mathbf{T} = \begin{pmatrix} \mathcal{K} & 0 & 0 \\ 0 & 1 & 0 \\ 0 & 0 & \mathcal{K} \end{pmatrix}, \mathbf{T}' = \begin{pmatrix} -\mathcal{K} & 0 & 0 \\ 0 & 1 & 0 \\ 0 & 0 & -\mathcal{K} \end{pmatrix}, \quad (5-2b)$$

where \mathbf{J} is the 3×3 anti-diagonal identity matrix, and \mathcal{K} conducts the operation of complex conjugation. These operations in conjunction leave the system unaltered. The eigenfrequencies of the above system, as expressed in the bases $e^{i\omega\tau}$, can be derived from the secular equation

$(H_{eff} - \omega_n \mathbf{I})\Psi = 0$ with $n = 1, 2, \dots, 6$, which in turn gives:

$$\omega_n = \pm 1, \pm \sqrt{\frac{2\gamma^2 - 1 \pm \sqrt{1 - 4\gamma^2 + 8\gamma^4 \kappa^2}}{2\gamma^2(1 - 2\kappa^2)}}. \quad (5-3)$$

Note that the positive and negative frequency solutions of Eq. (5-3) are essentially the same. I will remove this redundancy by considering only the positive signs (this does not include the signs inside the square root functions). By inspecting Eq. (5-3), I can identify three different regimes, separated by the exceptional point γ_{EP} and the critical point γ_c (defined as the point of critical damping, as I will discuss later in more details):

$$\gamma_{EP} = \frac{\sqrt{1 + \sqrt{1 - 2\kappa^2}}}{2\kappa} \quad \text{and} \quad \gamma_c = \frac{\sqrt{1 - \sqrt{1 - 2\kappa^2}}}{2\kappa}. \quad (5-4)$$

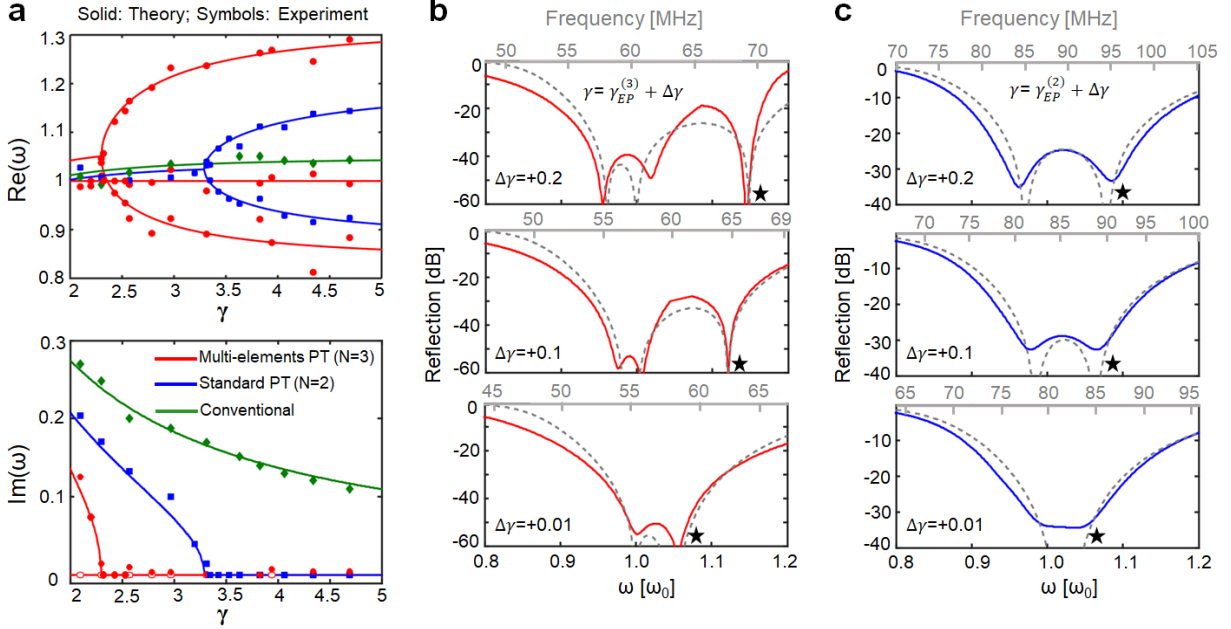


Figure 5-2 Evolution of eigenfrequencies and reflection spectra as a function of the non-Hermiticity parameter γ for the standard (two-elements) and three-elements PT -symmetric telemetric systems. a. Experimental and theoretical complex eigenfrequencies, varying a function of non-Hermiticity parameter γ , for the three-elements PT -symmetric system (red circles), the standard PT -symmetric system (blue squares), and the conventional telemetric system using a micro-coil reader (green diamonds). In all telemetric systems, the coupling strength κ is fixed to 0.3. **(b, c)** Magnitude of the reflection coefficient versus frequency for the three-elements PT -symmetric system and the standard PT -symmetric system. Both systems are controlled to operate around the exceptional point (EP), under the coupling strength $\kappa = 0.3$. Solid and dashed lines denote experimental and theoretical results, respectively.

In particular, when $\gamma \in [\gamma_{EP}, \infty]$, the eigenfrequencies are purely real ($\omega_n \in \mathbb{R}$) and $\mathcal{PT} \Psi = \Psi$, indicating that the PT -symmetry is exact. In this exact PT -symmetric phase, oscillatory motions can be obtained at the eigenfrequencies or resonance frequencies. On the other hand, when $\gamma \in [\gamma_c, \gamma_{EP}]$ the eigenfrequencies become complex conjugate pairs ($\omega_n \in \mathbb{C}$), signaling a transition to the broken phase where $\mathcal{PT} \Psi \neq \Psi$. This corresponds to an underdamped mode, and

it could be unstable (if the system has a net gain) due to the exponentially growing mode related to the imaginary part of ω_n . Finally, when $\gamma < \gamma_c$, all eigenfrequencies become purely imaginary, corresponding to the overdamped mode. The point γ_c thus corresponds to the critical damping. Importantly, a unique feature of the solution (3), which does not have analogy in optical systems, is the existence of an unremovable pole singularity at $2\kappa^2 = 1$. At this point, $\gamma_{EP} = \gamma_c$ and the system exhibits a DEP. In the vicinity of this point, the critical and exceptional points are different, but both are close to the pole singularity, which significantly impacts the frequency splitting associated with the EP. Figure 5-1d demonstrates this behavior. I should note that, in theory, this pole singularity exists in the standard PT symmetric circuit consisting of only two elements, but it occurs when $\kappa^2 = 1$, which is impossible to achieve because it implies a perfect magnetic coupling, with zero magnetic flux leakage. On the other hand, adding the central LC circuit relaxes this condition and provides access to this operating point for the first time.

In order to confirm these predictions, I built an onboard tunable RLC tank to mimic a wireless capacitive sensor. This pseudo-sensor consists of a variable capacitor, connected in series to a planar spiral inductor and a resistor (which accounts for the effective resistance of the sensor), such that its equivalent circuit is identical to that of a realistic wireless sensor. The information provided by the sensor is then read by an onboard $-RLC$ tank connected to the vector network analyzer (VNA) for measuring the reflection spectrum (see Method for more details). While the standard PT -symmetric telemetric system is made by paring the $-RLC$ and RLC oscillators via the magnetic coupling [Fig. 5-1a], the three-elements PT -symmetric system is constructed by inserting a neutral LC tank between the $-RLC$ and RLC oscillators (Fig. 5-1b). In the RLC and $-RLC$ resonators, the inductance of microstrip coils is $L = 330$ nH and the absolute value of resistance

$| -R | = R = 50 \, \Omega$. In order to emulate behaviors of a wireless capacitive sensor, the capacitance of tank circuits is tuned from 10 pF to 220 pF (SMA CER ± 0.05 pF), which in turn varies the non-Hermiticity parameter of the system ($\gamma \propto 1/\sqrt{C}$). The setup of the wireless experiment is shown in Fig. 5-1c. Figure 5-2a shows the theoretical (solid lines) and experimental (dots) results for complex eigenfrequencies as a function of γ for the standard and three-elements *PT*-symmetric telemetric systems; here, the coupling strength between two nearby resonant tanks is weak and fixed to $\kappa = 0.3$. Excellent results between theory and experiment is observed, indicating an enhanced frequency splitting even for a relatively small value of κ . When $\gamma \gg \gamma_{EP}$, positive eigenfrequencies of an electronic *PT*-symmetric dimer will diverge asymptotically to $\omega_n \approx 1/\sqrt{1 \pm \kappa^2}$, while those become $\omega_n = 1, 1/\sqrt{1 \pm \sqrt{2}\kappa}$ in an electronic *PT*-symmetric trimer. The level of bifurcation is proportional to the coupling strength and can be quite drastic in the vicinity of a DEP. I note that the exceptional point γ_{EP} is downshifted for the three-elements circuit, as predicted by theory. This in turn allows a lossy sensor with a small γ ($\gamma \propto 1/R$) to operate right beyond the exceptional point and in the exact *PT*-symmetric phase.

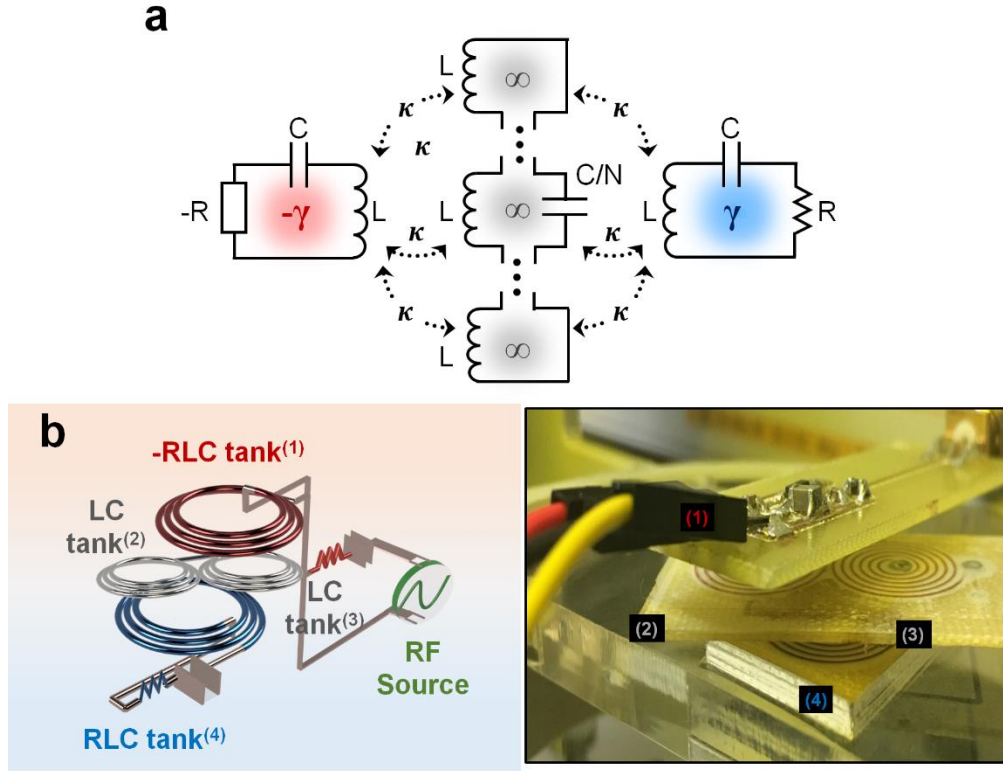


Figure 5-3 Multi-links multi-stages PT -symmetric electronic system. **a.** Schematics of a multi-links three-elements PT -symmetric system with N' coplanar spiral inductors in the intermediary. **b.** Experimental setup for the PT -symmetric telemetric system in **a**, with $N' = 2$ (four links).

Figure 5-2b presents evolutions of reflection spectrum for the three-elements PT -symmetric telemetric systems described above. For comparison, Fig. 5-2c presents the standard PT -symmetric telemetric system formed by only two elements (Fig. 5-1a) having $L = 330$ nH and $\kappa = 0.3$. I find that under the same coupling strength, the electronic PT -symmetric trimer exhibits larger resonance frequency shifts compared to the electronic PT -symmetric dimer. Overall, our

experimental results confirm the superior performance of the three-elements wireless sensor, since it could operate closer to a DEP.

Naturally, one can ask if it is possible to provide more access to a DEP (which translates into even more sensitivity) by modifying the intermediating element or adding more elements into the system. To answer this question, I experimentally investigate the effect of adding more inductive coils (which I will call links) in the neutral element, as shown in Fig. 5-3a. If I consider N' mutually uncoupled links, it is not difficult to show that the frequency splitting is given by:

$$\omega_n = \pm 1, \pm \sqrt{\frac{2\gamma^2 - 1 \pm \sqrt{1 - 4\gamma^2 + 8N'\gamma^4\kappa^2}}{2\gamma^2(1 - 2N'\kappa^2)}}, \quad (5-6)$$

which clearly shows that the pole singularity is further downshifted. From an experimental perspective, this means that stronger splitting can be achieved even by using a smaller κ (which is reduced by a factor of $\sqrt{1/N'}$, compared to the previous dual-links third-elements system with $N = 3$ and $N' = 1$). In order to test these predictions, I have experimentally implemented a multi-coupled PT -symmetric circuit having and $N = 3$ and $N' = 2$ (see Fig. 5-3b), eventually leading to a reduced critical coupling strength $\kappa_c = 1/2$. Figure 5-4a presents theoretical (solid lines) and experimental (dots) results for eigenfrequencies as a function of γ for the four-links three-elements PT -symmetric system with $\kappa = 0.49$ (Fig. 5-3b) and the standard PT -symmetric system with $\kappa = 0.7$ (Fig. 5-1a). As expected, adding more links lead to even more enhancement in the eigenfrequency bifurcation. Such intriguing properties can be utilized for ultra-sensitively telemetering information of various RF sensors. The gigantic bifurcation effect can be attributed to the fact that the system now operates in a region very close to singular points, as κ_c is reduced by a factor of $1/\sqrt{N'}$ (here $\kappa_c = 1/2$) and the exceptional point is even further downshifted to

$\gamma_{\text{EP}} = \frac{\sqrt{1 + \sqrt{1 - 2N'\kappa^2}}}{2\kappa\sqrt{N'}}$ (here $\gamma_{\text{EP}} = 0.79$). For the sake of completeness, Fig. 5-4a also presents

results for the conventional telemetric system with a coil-antenna reader (whose self-inductance $L = 330$ nH). In this case, the eigenfrequency always has a complex value and its real part is rather insensitive to changes in γ ($\Delta\gamma$). Hence, a weak resonance and a scarcely detectable resonance frequency shift were observed in the reflection spectrum (not shown here). Figure 5-4b reports the theoretical and measured reflection spectra for the four-links three-elements PT -symmetric telemetric system in Fig. 5-3b, with $\kappa = 0.49$ and γ being varied from 0.77 to 2.1. There exists certain discrepancy between theoretical and measurement results, mainly due to stray fields and unexpected parasitic elements. Figure 5-4c reports the reflection spectra for the standard PT -symmetric telemetric systems in Fig. 5-1a. From Fig. 5-4, I find that with the same range of $\Delta\gamma$, the resonance frequency shift in the four-links three-elements PT -symmetric system is much greater than in the standard (single-link two-elements) PT -symmetric setup. Moreover, thanks to the downshifted exceptional point in the multi-links multi-elements PT -symmetric system, even a relatively lossy sensor could experience largely bifurcating resonance frequencies. Finally, I note that intermediators in the multi-stages PT -symmetric telemetric system can also have arranged into a series configuration (e.g., a sequence of coupled neutral elements or alternating gain-loss elements) for elongating the interrogation distance. I have theoretically demonstrated that the critical coupling strength of such systems has a lower bounded $\kappa_c = 1/2$ (see section 5.4).

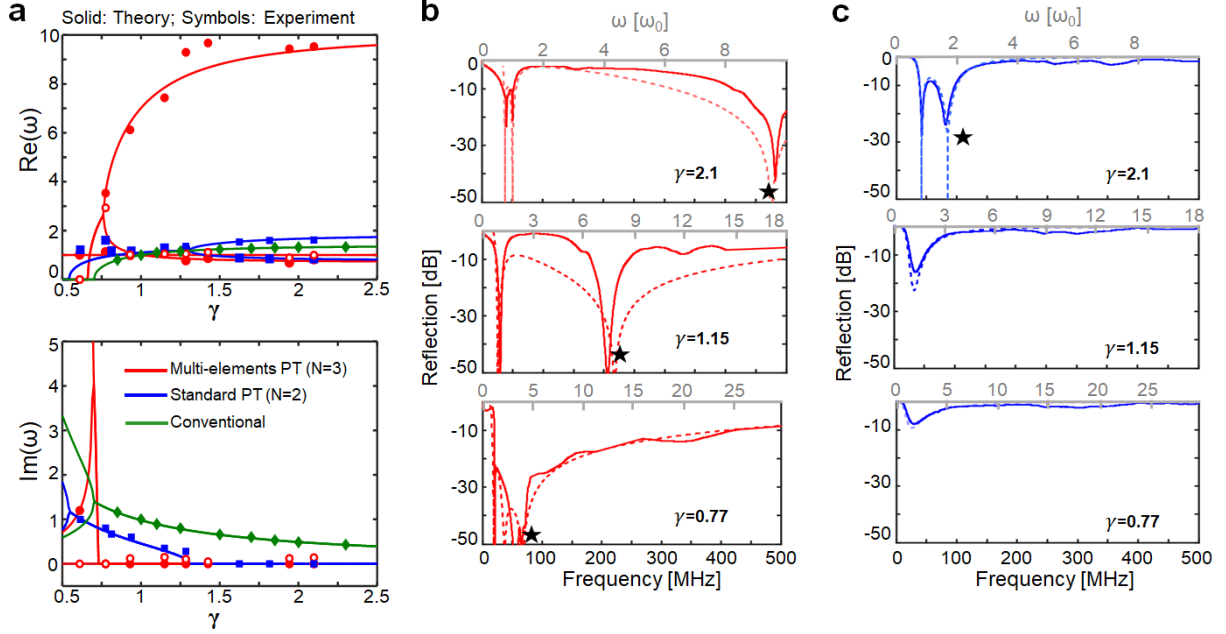


Figure 5-4 Evolution of eigenfrequencies and reflection spectra as a function of the non-Hermiticity parameter γ for the four-links three-elements PT -symmetric telemetric system. **a.** Experimental and theoretical complex eigenfrequencies, varying a function of non-Hermiticity parameter, for the dual-links three-stages PT -symmetric telemetric system in Fig. 5-3b with $\kappa_c = 0.49$ (red circles), the standard PT -symmetric telemetric system in Fig. 5-1a with $\kappa_c = 0.7$ (blue squares), and the conventional one using a micro-coil reader with $\kappa_c = 0.7$ (green diamonds). **(b, c)** Magnitude of the reflection coefficient versus frequency for the four-links third-stages PT -symmetric telemetric system in **a**, in comparison with the standard PT -symmetric telemetric system; here, the non-Hermiticity parameters γ is varied from 0.77 to 2.1. Note that if $\gamma < 1.3$, the standard PT -symmetric system ($\gamma_{EP} = 1.3$) operates in the broken phase, which exhibits a weak resonance with a low quality factor. Solid and dashed lines denote experimental and theoretical results, respectively.

5.3 RF reader designs and wireless measurement setups

In our measurements, the reader ($-RLC$ tank) was connected to the vector network analyzer or VNA (Agilent E5061B; $Z_0 = 50 \Omega$), and the intermediary (LC tank) and the pseudo-sensor (RLC tank) were fixed on the XYZ linear translation stage. In the $-RLC$ tank, the equivalent negative

resistance can be realized with a negative impedance converter, such as a Colpitts-type circuit with a positive feedback. In addition, while a resistor accounts for power dissipation, a negative resistor means a source of energy in the closed-loop analysis. Hence, a RF signal generator with source impedance Z_0 (e.g., a VNA that feeds the reader) is described by a negative impedance $-Z_0$. In the one-port measurement, the information is encoded in the reflection coefficient. For example, if the physical quantity of interest varies the capacitance of a passive wireless capacitive sensor (equivalent to a RLC oscillator), it can be characterized by tracking the resonance frequency shift. For the standard PT -symmetric system (Fig. 5-1a), the reflection coefficient can be derived as:

$$\Gamma = \frac{\sum_{n=1}^4 \omega - \omega_n}{\frac{2\omega \left[\omega + i\gamma(\omega^2 - 1) \right]}{\eta\gamma^2(\kappa^2 - 1)} + \sum_{n=1}^4 \omega - \omega_n}, \quad (5-7)$$

where $\eta = R / Z_0$ and ω_n is the n -th eigenfrequency of the system. For the third-order PT -symmetric system (Fig. 5-1b), the reflection coefficient is:

$$\Gamma = \frac{\sum_{n=1}^6 \omega - \omega_n}{\frac{2\omega \left[\omega(\omega^2 - 1) + i\gamma \left(1 - 2\omega^2 - (\kappa^2 - 1)\omega^4 \right) \right]}{\eta\gamma^2(2\kappa^2 - 1)} + \sum_{n=1}^6 \omega - \omega_n}. \quad (5-8)$$

From Eqs. (5-7)-(5-8), reflection dips are obtained at ω_n (in the unit of ω_0). In the exact PT -symmetric phase ($\omega_n \in \mathbb{R}$), zero reflection can be achieved when $\omega = \omega_n$.

5.4 Physical Bounds of the Bifurcation Effect in PT -Symmetric Telemetry Systems

It is of importance to understand the fundamental limit of the eigenfrequency bifurcation in PT -symmetric electronic systems. In the standard PT -symmetric electronic system (i.e., coupled $-RLC$ and RLC oscillators [Fig. 5-1a]), if $\gamma \gg \gamma_{EP}$, the two positive eigenfrequencies would diverge

asymptotically to $\omega_n \approx 1/\sqrt{1 \pm \kappa^2}$. In this case, when the exceptional point ($\omega_{EP} = (1 - \kappa^2)^{-1/4}$) is taken as a reference, ranges of eigenfrequency splitting for the upper and lower branches are:

$$\Delta\omega_+ \in \left[0, (1 - \kappa)^{-1/2} - (1 - \kappa^2)^{-1/4} \right] \xrightarrow{\kappa \rightarrow 1} \Delta\omega_+ \in [0, \infty]; \quad (5-9a)$$

$$\Delta\omega_- \in \left[(1 + \kappa)^{-1/2} - (1 - \kappa^2)^{-1/4}, 0 \right] \xrightarrow{\kappa \rightarrow 1} \Delta\omega_- \in [-\infty, 0]. \quad (5-9b)$$

In the case of perfect coupling ($\kappa = 1$), the critical point overlaps with the exceptional points ($\gamma_c = \gamma_{EP} = 1/\sqrt{2}$) and the degenerate eigenfrequencies become $\pm i\infty$. Assuming the coupling strength is close to (but slightly less than) unity, the two eigenfrequencies would rapidly diverge toward ∞ and $1/\sqrt{2}$, leading to $\Delta\omega_+ \in [0, \infty]$ and $\Delta\omega_- \in [-\infty, 0]$. In principle, the degree of bifurcation increases with increasing κ , and it is possible to achieve huge $\Delta\omega_+$ and $\Delta\omega_-$ within a small range of $\Delta\gamma$.

In the third-order system (Fig. 5-1b), the critical coupling strength that leads to the divergent exceptional point (DEP) is reduced to $\kappa_c = 1/\sqrt{2}$, which is practically reasonable for coil-based inductive links. If $\gamma_c \gg \gamma_{EP}$, eigenfrequencies of the system are $\omega_n = \pm 1, \pm 1/\sqrt{1 \pm \sqrt{2}\kappa}$, which merge at the exceptional point ($\omega_{EP} = \pm 1/(1 - 2\kappa^2)^{1/4}$), leading to:

$$\Delta\omega_+ \in \left[0, (1 - \sqrt{2}\kappa)^{-1/2} - (1 - 2\kappa^2)^{-1/4} \right] \xrightarrow{\kappa \rightarrow 1/\sqrt{2}} \Delta\omega_+ \in [0, \infty]; \quad (5-10a)$$

$$\Delta\omega_- \in \left[0, (1 + \sqrt{2}\kappa)^{-1/2} - (1 - 2\kappa^2)^{-1/4} \right] \xrightarrow{\kappa \rightarrow 1/\sqrt{2}} \Delta\omega_- \in [-\infty, 0]. \quad (5-10b)$$

In another extreme case, if $\kappa=0$, the critical and exceptional points are far apart from each other (i.e., $\gamma_c = 1/2$ and $\gamma_{EP} \rightarrow \infty$). If $\kappa \sim 0$ and $\gamma \gg \gamma_{EP}$, eigenfrequencies of the standard PT -symmetric electronic system are $\omega_n \simeq \pm\sqrt{1 \pm \kappa} \approx \pm(1 \pm \kappa/2)$ and those of the third-order PT -symmetric system are $\omega_n \simeq \pm 1, \pm(1 \pm \kappa/\sqrt{2})$. If the exceptional point ($\omega_{EP} \simeq \pm 1$) is taken as a reference point, bifurcating ranges for the standard PT -symmetric system are:

$$\Delta\omega_+ \in [0, \kappa/2]; \quad (5-11a)$$

$$\Delta\omega_- \in [-\kappa/2, 0]. \quad (5-11b)$$

Under the same weak-coupling condition, the bifurcating ranges for the third-order PT -symmetric system are:

$$\Delta\omega_+ \in [0, \kappa/\sqrt{2}]; \quad (5-12a)$$

$$\Delta\omega_- \in [-\kappa/\sqrt{2}, 0]. \quad (5-12b)$$

In the weak coupling regime, there is no distinct eigenfrequency splitting (or resonance frequency shift), which is of little interest for sensing applications. Overall, the bifurcating range is proportional to the coupling strength. In the strong coupling regime, the sensitivity enhancement enabled by the non-Hermiticity degeneracy is particularly obvious.

5.5 Generalized N th-Order PT -Symmetric Electronic Systems

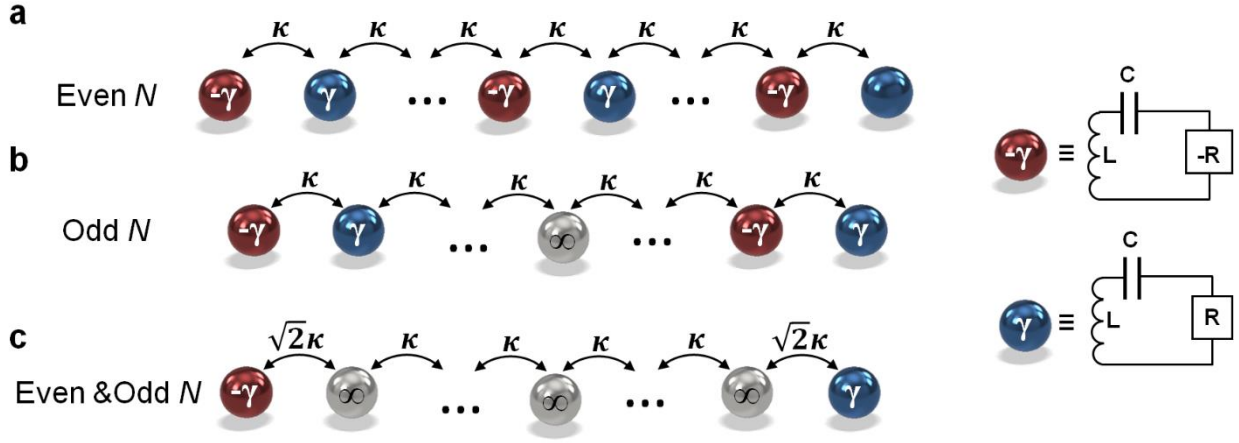


Figure 5-5 Generalized N th-order PT -symmetric electronic systems. Schematic illustration for the PT -symmetric telemetric system comprising (a) even-numbered and (b) odd-numbered oscillators, as well as (c) a pair of $-RLC$ and RLC oscillators that are coupled via one or multiple neutral intermediators.

In general, there could be more than one intermediary between the reader and sensor/tag in a telemetry system. **Figure 5-5** shows the generalized PT -symmetric electronic system formed by even-numbered oscillators (i.e., $N/2$ pairs of $-RLC$ and RLC tanks shown in Fig. 5-9a) and odd-numbered oscillators (i.e., $(N-1)/2$ pairs of $-RLC$ and RLC tanks and one neutral tank shown in Fig. 5-9b). These higher-order PT -symmetric systems can still be described by the Liouvillian formalism $d\Psi/d\tau = i\mathbf{H}_{eff}\Psi$, where Ψ is the modal column vector of dimensionality N and \mathbf{H}_{eff} is the effective non-Hermitian Hamiltonian of dimensionality $N \times N$. The eigenfrequencies of these systems can be derived from the eigenproblem: $(\mathbf{H}_{eff} - \omega_n \mathbf{I})\Psi = 0$.

The eigenfrequencies of the even-order PT -symmetric electronic system shown in Fig. 5-5a can be derived from the eigenvalue equation. They are found to be roots of the transcendental equation $U_\alpha^{\text{even}} = 0$, where $\alpha = N/2$ and U_α^{even} is a sequence of orthogonal polynomials that can be defined by the recurrence relation:

$$\begin{aligned} U_0^{\text{even}} &= 1 \\ U_1^{\text{even}} &= x - \kappa^2 \\ U_{\alpha+1}^{\text{even}} &= (x - 2\kappa^2)U_\alpha^{\text{even}} - \kappa^4 U_{\alpha-1}^{\text{even}} \end{aligned}$$

or

$$U_\alpha^{\text{even}} = \prod_{\beta=0}^{\alpha-1} x - (2\kappa A_{\alpha\beta})^2, \quad (5-13)$$

where

$$A_{\alpha\beta} = \sin\left(\frac{\pi}{2} \frac{2\beta+1}{2\alpha+1}\right), \quad (5-14)$$

and $x = \left(\frac{\omega^2 - 1}{\omega^2}\right)^2 + \left(\frac{1}{\gamma\omega}\right)^2$. From Eqs. (5-13) and (5-14), $2N$ eigenfrequencies of the system are given by:

$$\omega_n = \pm \sqrt{\frac{2\gamma^2 - 1 \pm \sqrt{1 - 4\gamma^2 + 16\gamma^4 \kappa^2 A_{\alpha\beta}^2}}{2\gamma^2 [1 - 4\kappa^2 A_{\alpha\beta}^2]}}. \quad (5-15)$$

where $\beta = 0, 1, 2, \dots, \alpha - 1$. In these systems, there may be $N/2$ exceptional points and $N/2$ critical points, and more than one critical coupling strength, whose values can be derived from the above equation as:

$$\gamma_c = \frac{1}{2\kappa} \sqrt{\frac{1 - \sqrt{1 - 4\kappa^2 A_{\alpha\beta}^2}}{2A_{\alpha\beta}^2}}, \quad \gamma_{EP} = \frac{1}{2\kappa} \sqrt{\frac{1 + \sqrt{1 - 4\kappa^2 A_{\alpha\beta}^2}}{2A_{\alpha\beta}^2}}, \quad (5-16a)$$

and

$$\kappa_c = \frac{1}{2A_{\alpha\beta}}. \quad (5-16b)$$

As examples, the eigenspectra for the N th-order PT -symmetric electronic systems are shown in Fig. 5-10.

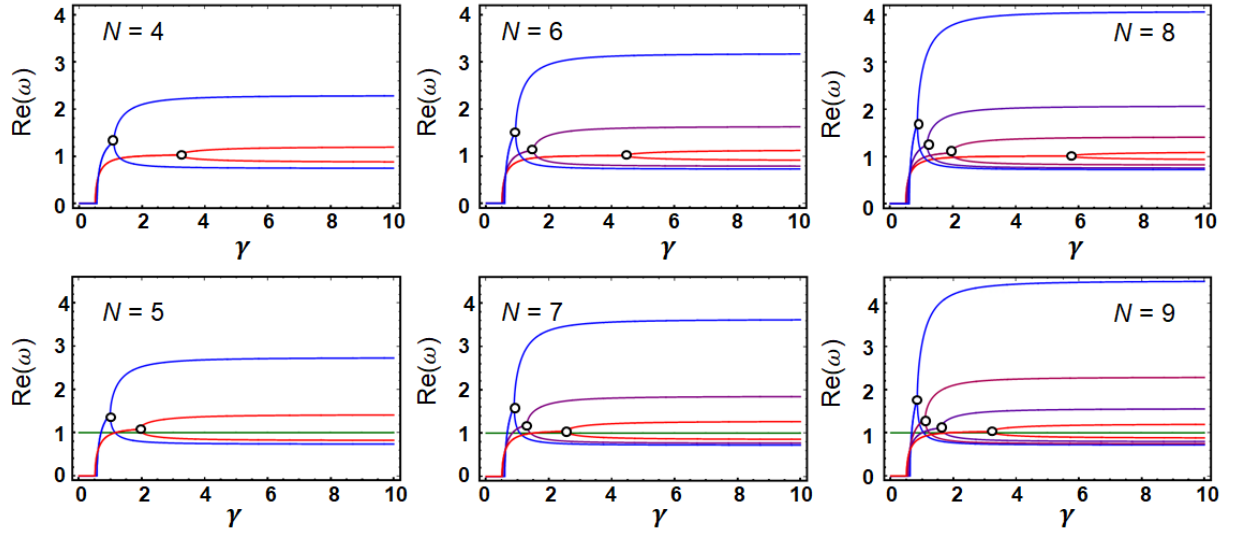


Figure 5-6 Evolutions of eigenspectra for PT -symmetric electronic systems in Fig. 5-9, with different orders ($N = 4, 5, 6, 7, 8, 9$); here, the coupling strength is fixed to $\kappa = 0.5$.

For the odd-order PT -symmetric electronic systems shown in Fig. 5-6b, eigenfrequencies are found to be roots of the transcendental equation $(\omega^2 - 1)U_\alpha^{\text{odd}} = 0$, where $\alpha = (N-1)/2$ and U_α^{odd} is a sequence of orthogonal polynomials that can be defined by the recurrence relation:

$$\begin{aligned} U_0^{\text{odd}} &= 1 \\ U_1^{\text{odd}} &= x - 2\kappa^2 \\ U_{\alpha+1}^{\text{odd}} &= (x - 2\kappa^2)U_\alpha^{\text{odd}} - \kappa^4 U_{\alpha-1}^{\text{odd}} \end{aligned}$$

or

$$U_\alpha^{\text{odd}} = \prod_{\beta=0}^{\alpha-1} x - (2\kappa B_{\alpha\beta})^2, \quad (5-17)$$

where

$$B_{\alpha\beta} = \sin\left(\frac{\pi}{2} \frac{\beta+1}{\alpha+1}\right). \quad (5-18)$$

From the Eqs. (5-17) and (5-90), $2N$ eigenfrequencies of the system can be explicitly written as:

$$\omega_n = \pm 1, \pm \sqrt{\frac{2\gamma^2 - 1 \pm \sqrt{1 - 4\gamma^2 + 16\gamma^4 \kappa^2 B_{\alpha\beta}^2}}{2\gamma^2 [1 - 4\kappa^2 B_{\alpha\beta}^2]}}. \quad (5-19)$$

where $\beta = 0, 1, 2, \dots, \alpha - 1$. From the above equation, expressions for $(N-1)/2$ exceptional and critical points, and critical coupling strengths can be obtained in the same forms as:

$$\gamma_c = \frac{1}{2\kappa} \sqrt{\frac{1 - \sqrt{1 - 4\kappa^2 B_{\alpha\beta}^2}}{2B_{\alpha\beta}^2}}, \quad \gamma_{EP} = \frac{1}{2\kappa} \sqrt{\frac{1 + \sqrt{1 - 4B_{\alpha\beta}^2 \kappa^2}}{2B_{\alpha\beta}^2}}, \quad (5-20a)$$

and

$$\kappa_c = \frac{1}{2B_{\alpha\beta}}. \quad (5-20b)$$

Since $0 \leq A_{\alpha\beta}, B_{\alpha\beta} \leq 1$, Eqs. (5-16b) and (5-92b) indicate a lower bound on κ_c ; namely, κ_c cannot be lower than $1/2$, regardless of the order of the PT -symmetric electronic system. Besides, if $\kappa_c > 1$, the system is not physically feasible, which sets an upper physical bound.

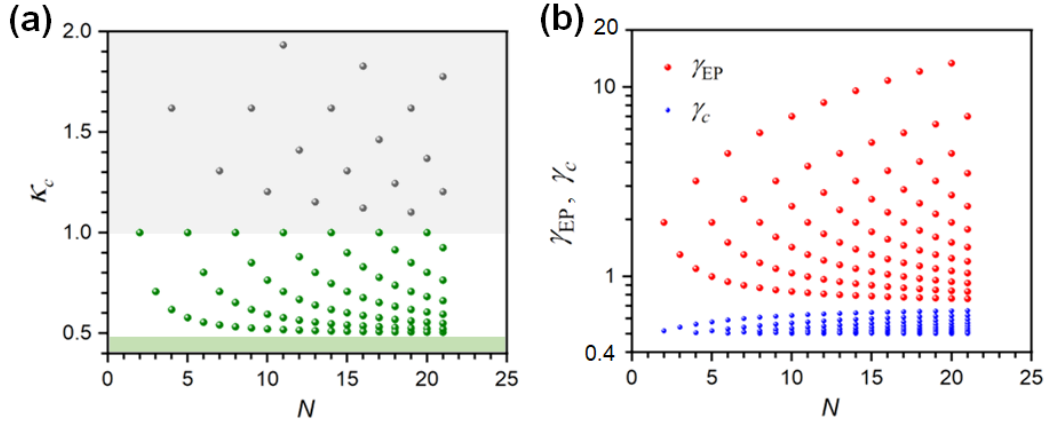


Figure 5-7 (a) Coupling strength κ_c for different PT -symmetric electronic systems in Fig. 5-9. κ_c has an upper bound of 1 (gray area is invalid) and a lower bound of 0.5. (b) Exceptional and critical points (γ_{EP} and γ_c) for different PT -symmetric electronic systems in Fig. 5-9, under a fixed coupling strength $\kappa = 0.5$

Figure 5-7a reports critical coupling strengths for standard ($N = 2$) and higher-order ($2 < N < 21$) PT -symmetric electronic systems in Fig. 5-5, showing that κ_c is, indeed, bounded between $1/2$ and 1 . The region where $\kappa_c > 1$ (gray dots) is forbidden. When κ is close to a specific κ_c (green dots), a sharp bifurcation effect can be observed in the eigenspectrum. Figure 5-7b reports γ_{EP} (red dots) and γ_c (blue dots) for standard and higher-order PT -symmetric systems with $\kappa = 1/2$. I find that the γ_{EP} decreases with increasing the order of the PT -symmetric system, whereas γ_c exhibits an opposite trend. As a result, if a large number of active and passive oscillators are used, γ_{EP} and γ_c will merge, which leads to a drastic bifurcation effect in the vicinity of DEP.

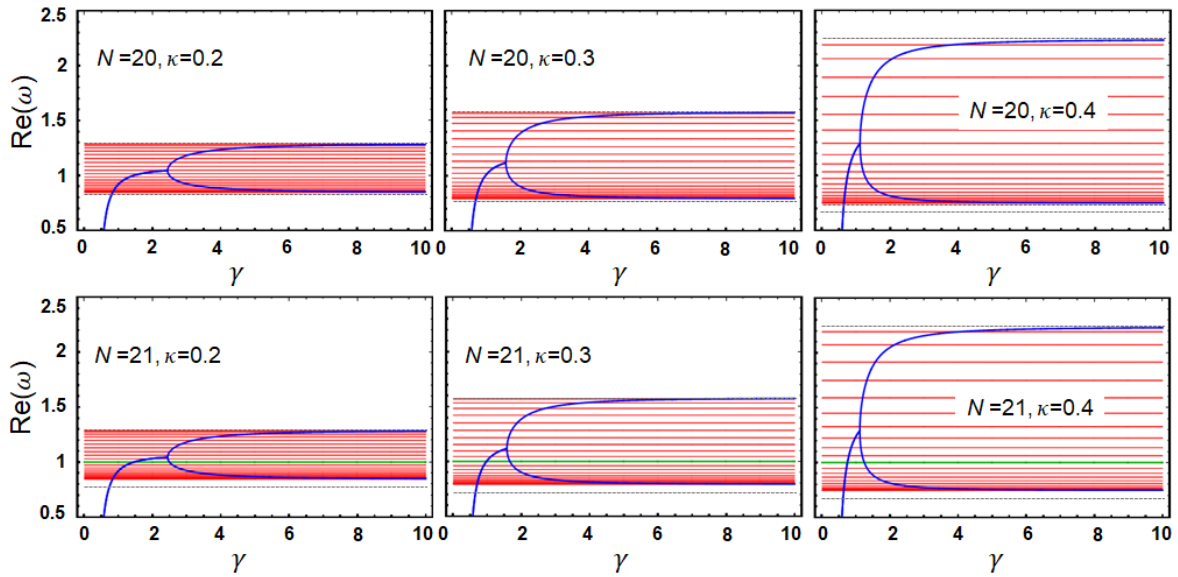


Figure 5-8 Eigenfrequencies versus the non-Hermiticity parameter for the PT -symmetric electronic system in figures 5-9c, with different numbers of intermediary and coupling strengths.

Finally, I consider another higher-order PT -symmetric electronic system, comprising a – RLC oscillator and a RLC oscillator that are remotely coupled via $N-2$ neutral intermediators ($N > 3$), as shown in Fig. 5-5c. Such a telemetry system with multiple neutral intermediators is quite common in practical RF applications, such as sensing and wireless power transfer. Specifically, by setting the coupling strength between two neutral intermediators to be κ , and that between the gain (loss) oscillator and its neighboring intermedicator to be $\kappa' = \kappa\sqrt{2}$, as shown in Fig. 5-9c, eigenfrequencies of this system are found to be roots of the following transcendental equation:

$$\begin{cases} (x^2 - 4\kappa^2)V_{\alpha}^{\text{even}} = 0 \text{ and } \alpha = \frac{N-2}{2}, & \text{for } N = 4, 6, 8, \dots \\ (\omega^2 - 1)(x^2 - 4\kappa^2)V_{\alpha}^{\text{odd}} = 0 \text{ and } \alpha = \frac{N-3}{2}, & \text{for } N = 5, 7, 9, \dots \end{cases}$$

where

$$V_{\alpha}^{\text{even}} = \prod_{\beta=0}^{\alpha-1} x' - (2\kappa A_{\alpha\beta})^2,$$

$$V_{\alpha}^{\text{odd}} = \prod_{\beta=0}^{\alpha-1} x' - (2\kappa B_{\alpha\beta})^2,$$

$$x' = \left(1 - \frac{1}{\omega^2}\right)^2,$$

and expressions for $A_{\alpha\beta}$ and $B_{\alpha\beta}$ can be found in Eqs. (5-14) and (5-90).

If N is an odd number, eigenfrequencies are given by:

$$\omega_n = \pm 1, \pm \sqrt{\frac{2\gamma^2 - 1 \pm \sqrt{1 - 4\gamma^2 + 16\gamma^4 \kappa^2}}{2\gamma^2 [1 - 4\kappa^2]}}, \pm \frac{1}{\sqrt{1 \pm 2\kappa A_{\alpha\beta}}}. \quad (5-21)$$

If N is an even number, eigenfrequencies are given by:

$$\omega_n = \pm \sqrt{\frac{2\gamma^2 - 1 \pm \sqrt{1 - 4\gamma^2 + 16\gamma^4 \kappa^2}}{2\gamma^2 [1 - 4\kappa^2]}}, \pm \frac{1}{\sqrt{1 \pm 2\kappa B_{\alpha\beta}}}. \quad (5-22)$$

From Eqs. (5-93) and (5-94), I find that the higher-order PT -symmetric electronic systems with multiple neutral intermediators exhibit four γ -dependent eigenfrequencies, which are identical to those of the third-order PT -symmetric setup [Eq. (5-3)]. In addition, there are $2(N-2)$ eigenfrequencies that are independent of γ (i.e., flat lines in the eigenspectrum), of little interest to sensing applications. All positive eigenvalues are bounded in the range: $\omega_n \in [1/\sqrt{1+2\kappa}, 1/\sqrt{1-2\kappa}]$. An exemplified eigenspectrum is shown in Fig. 5-12. This system only has one exceptional point and one critical point, and thus one critical coupling strength. From Eqs. (5-93) and (5-94), their values are given by:

$$\gamma_c = \frac{1}{2\kappa} \sqrt{\frac{1 - \sqrt{1 + 4\kappa^2}}{2}}, \quad \gamma_{EP} = \frac{1}{2\kappa} \sqrt{\frac{1 + \sqrt{1 + 4\kappa^2}}{2}}, \quad (5-23a)$$

and

$$\kappa_c = \frac{1}{2}. \quad (5-23b)$$

We find that γ_c and γ_{EP} are independent of the order of the system and are a strong function of the coupling strength. Increasing the order, however, may elongate the total interrogation distance.

5.6 Conclusion

In summary, I have introduced the notion of divergent exceptional points in multi-elements PT -symmetric electronic systems and shown that it can lead to gigantic eigenfrequency splitting. I have tested our predictions experimentally in a PT -symmetric “gain-neural-loss” electronic trimer

and have demonstrated that, indeed, the eigenfrequency bifurcation around the divergent exceptional point can be quite dramatic, with a physical upper bound approaching infinity (see section 5.4). I envision that such new non-Hermitian electronic systems, when applied to wireless probing and telemetering (e.g., a set of coupled oscillators including the $-RLC$ reader, LC intermediary, and RLC sensor), will enable a superior sensing capability, as any tiny impedance change on the sensor could cause a wide range tuning of resonance frequencies. Similar performance was not found in the standard PT -symmetric electronic system [6],[7] or the multi-coupled PT -symmetric optical systems [1]. This work may not only open new avenues for high-performance RF sensors, but also be extendable to other microwave, millimeter-wave and terahertz wireless sensing and telemetering systems.

REFERENCES

- [1] Rüter, C. E. *et al.* Observation of parity–time symmetry in optics. **6**, 192–195 (2010).
- [2] Ramezani, H., Kottos, T., El-Ganainy, R. & Christodoulides, D. N. Unidirectional nonlinear PT-symmetric optical structures. **82**, 43803 (2010).
- [3] Hodaei, H., Miri, M.-A., Heinrich, M., Christodoulides, D. N. & Khajavikhan, M. Parity-time–symmetric microring lasers. *Science* **346**, 975–978 (2014).
- [4] Feng, L., Wong, Z. J., Ma, R.-M., Wang, Y. & Zhang, X. Single-mode laser by parity-time symmetry breaking. *Science* **346**, 972–975 (2014).
- [5] Hodaei, H. *et al.* Enhanced sensitivity in photonic molecule systems using higher order non-Hermitian exceptional points. *Submitt. Nat.* (2017).
- [6] Chen, W., Kaya Özdemir, Ş., Zhao, G., Wiersig, J. & Yang, L. Exceptional points enhance sensing in an optical microcavity. *Nature* **548**, 192–196 (2017).
- [7] El-Ganainy, R., Dadap, J. I. & Osgood, R. M. Optical parametric amplification via non-Hermitian phase matching. *Opt. Lett.* **40**, 5086–5089 (2015).
- [8] Zhong, Q., Ahmed, A., Dadap, J. I., JR, R. M. O. & El-Ganainy, R. Parametric amplification in quasi-PT symmetric coupled waveguide structures. *New J. Phys.* **18**, 125006 (2016).
- [9] Feng, L., El-Ganainy, R. & Ge, L. Non-Hermitian photonics based on parity–time symmetry. *Nat. Photonics* **11**, 752–762 (2017).
- [10] El-Ganainy, R. *et al.* Non-Hermitian physics and PT symmetry. *Nat. Phys.* **14**, 11–19 (2018).
- [11] Heiss, W. D. Exceptional points of non-Hermitian operators. *J. Phys. Math. Gen.* **37**, 2455 (2004).
- [12] Rotter, I. A non-Hermitian Hamilton operator and the physics of open quantum systems. *J. Phys. Math. Theor.* **42**, 153001 (2009).

- [13] Lin, Z. *et al.* Unidirectional Invisibility Induced by PT-Symmetric Periodic Structures. *Phys. Rev. Lett.* **106**, 213901 (2011).
- [14] Longhi, S. Invisibility in PT-symmetric complex crystals. **44**, 485302 (2011).
- [15] Fleury, R., Sounas, D. & Alù, A. An invisible acoustic sensor based on parity-time symmetry. *Nat. Commun.* **6**, 5905 (2015).
- [16] Liertzer, M. *et al.* Pump-Induced Exceptional Points in Lasers. *Phys. Rev. Lett.* **108**, 173901 (2012).
- [17] Brandstetter, M. *et al.* Reversing the pump dependence of a laser at an exceptional point. *Nat. Commun.* **5**, (2014).
- [18] Peng, B. *et al.* Loss-induced suppression and revival of lasing. *Science* **346**, 328–332 (2014).
- [19] El-Ganainy, R., Khajavikhan, M. & Ge, L. Exceptional points and lasing self-termination in photonic molecules. *Phys Rev A* **90**, 13802 (2014).
- [20] Doppler, J. *et al.* Dynamically encircling an exceptional point for asymmetric mode switching. **537**, 76–79 (2016).
- [21] Xu, H., Mason, D., Jiang, L. & Harris, J. G. E. Topological energy transfer in an optomechanical system with exceptional points. *Nature* **537**, 80–83 (2016).
- [22] Needham, T. *Visual complex analysis*. (Clarendon, 2001).
- [23] Schindler, J., Li, A., Zheng, M. C., Ellis, F. M. & Kottos, T. Experimental study of active LRC circuits with PT symmetries. *Phys. Rev. A* **84**, 40101 (2011).
- [24] Assawaworrarit, S., Yu, X. & Fan, S. Robust wireless power transfer using a nonlinear parity–time-symmetric circuit. *Nature* **546**, 387–390 (2017).
- [25] Chen, P.-Y. *et al.* Generalized parity–time symmetry condition for enhanced sensor telemetry. *Nat. Electron.* **1**, 297–304 (2018).

VI. ROBUST EXTENDED-RANGE WIRELESS POWER TRANSFER USING A HIGHER-ORDER PT-SYMMETRIC PLATFORM

Parts of this chapter have been presented in (Sakhdari et al., 2020, PRR). Copyright©2020, PRR.

A fundamental challenge for the non-radiative wireless power transfer (WPT) resides in maintaining stable power transfer with a consistently high efficiency under dynamic conditions. Here, I propose and experimentally demonstrate that a frequency-locked WPT system satisfying higher-order parity-time (PT) symmetry can achieve a near-unity power transfer efficiency that is resilient to effects of distance variation and misalignment between coils, as well as impedance fluctuations in electric grids. In specific higher-order PT electronic systems, a purely real-valued and invariant (non-bifurcated) eigenfrequency would enable the robust and efficient wireless charging, even in the weak-coupling regime (mid-range operation). I envision that this WPT technique may provide reliable, fast and efficient power delivery for electric vehicles, consumer electronics, and medical devices.

6.1 wireless power transfer

Radio-frequency (RF) wireless power transfer (WPT) has experienced a rapid and widespread growth in recent years, as driven by the rising demand for wireless charging in consumer electronics, medical devices, sensors, and automotive applications [1-10]. The concept of transferring power without any physical contact was put forward soon after the proposition of Faraday's law of induction [11]. In late 1890s, Nikola Tesla conducted pioneering experiments with lighting electric bulbs wirelessly through electrodynamic induction (a.k.a. resonant *inductive* coupling) [12].

Although his efforts appear to have met with little success, nowadays, considerable progress in WPT has been made in the realm of non-radiative transfer that employs the near-field magnetic coupling to efficiently transmit electrical energy from a power source to electrical loads [3]. While the WPT technology has motivated considerable research and development in the past two decades [14-16], there are still several theoretical and technical issues which need further investigation to maximize the potential of this technology. Traditional WPT systems are not robust against alteration of distance and misalignment between coils [5, 17], and variations in the terminating impedance of an electric power grid or battery over time [1]. To date, several techniques have been proposed to optimize the efficiency of power transfer, which include dynamic adjustment of operating frequency (resonant-frequency tracking) [18, 19], *combination of multiple receivers* and repeaters for adaptive impedance matching [20], and adding nonlinear tuning elements in circuits [7, 10]. For these often used WPT schemes, when the coupling factor (as a function of distance and alignment between coils) changes, the operating frequency must be adjusted accordingly to maintain a high transfer efficiency [21, 22]. Besides, the range of inductive power transfer remains a principal challenge. In spite of recent advances in various coil designs and the capability to create spatial Bessel beams [23], it remains difficult to overcome the performance deterioration due to the poor tolerance in coil misalignment, especially in the weak-coupling regime [24, 25].

Very recently, a new WPT mechanism based on the concept of parity-time (PT) symmetry incorporating a nonlinear gain-saturation element has been projected to address this long-existing challenge [7]. Specifically, this system is engineered to have a subtle balance of energy flowing in (i.e., gain) and out (i.e., loss), and in its exact PT-symmetric phase, a nearly perfect transfer efficiency that is independent of the coupling strength can be achieved throughout the short-range operation. This PT WPT system does not need dynamic reconfiguration and sweeping of operating

frequency. However, in the standard (second-order) PT-symmetric electronic systems [26-30], the exact PT-symmetric phase requires a moderately strong coupling strength [26, 29], and this makes the system fail to maintain a satisfactory efficiency at weak/loose coupling (e.g., mid-range power transfer). In addition, perturbing the load resistance of receiver could lead to a symmetry-breaking phase transition [30] and a low efficiency is obtained in such broken PT-symmetric phases.

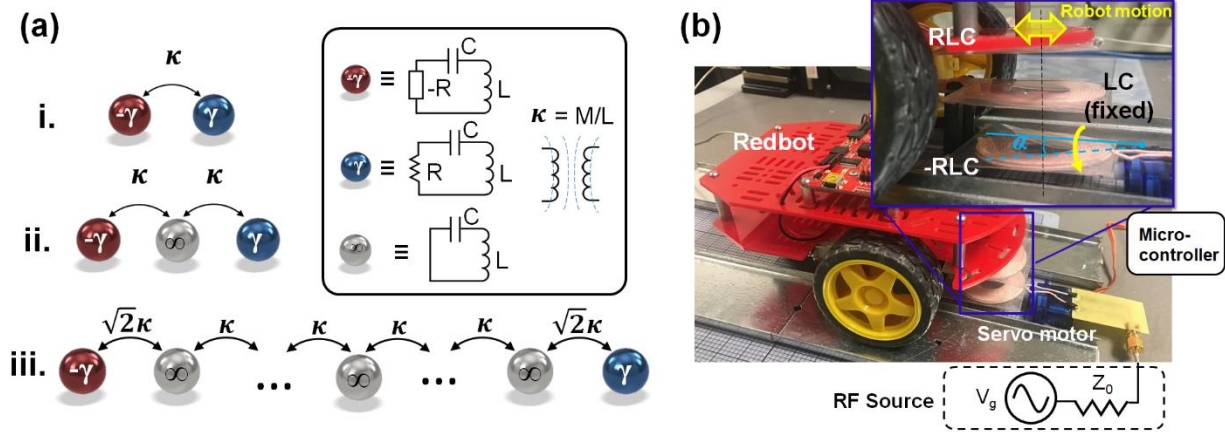


Figure 6-1. **a** Schematics for standard (i), third-order (ii), and other higher-order (iii) PT-symmetric electronic systems consisting of electronic molecules with gain (red), neutral (gray) and loss (blue) properties. **b** Third-order PT-symmetric wireless power transfer system, where a robot car (loss) is wirelessly charged by a platform consisting of a repeater (neutral) and an active transmitter (gain). The inductive coupling strength between the intermediate and receiver coils (κ) is random, and that between the transmitter and intermediate coils (κ') is tuned by rotating the transmitter coil and a feedback algorithm, such that $\kappa = \kappa'$ and PT symmetry is preserved.

In the following, I will present a new non-radiative WPT system with high-order PT symmetry, as shown in Fig. 6-1, which can further overcome the drawback of the standard PT-symmetric WPT system. Higher-order PT-symmetric electronic systems in Fig. 6-1(a) exhibit a unique eigenspectral feature: a purely real eigenfrequency that is insensitive to variations in the coupling strength and the gain-loss parameter (related to the receiver's load resistance or reactance). Such a property can ensure a transfer efficiency approaching 100 % over a wide range of distances and misalignment levels, thereby offering an unprecedented robustness and freedom in wireless charging.

6.2 Higher-order PT-symmetric wireless powering

In 1998, Bender and Boettcher introduced a class of non-Hermitian Hamiltonians [31] satisfying PT symmetry. Counterintuitively, if a quantum system is invariant under the combined action of space inversion (P) and time reversal (T), it exhibits either entirely real eigenspectra or complex conjugate eigenvalue pairs. Although PT-symmetry was originally considered as one of interesting theoretical findings, it has been experimentally demonstrated in optical [32, 33], acoustic [34] and electronic [26] platforms, and has aroused intense interest for real-life applications, such as lasers [35], sensors [29], cloaks [36], and non-reciprocal devices [37]. In electronics, the lumped-element circuitry could be the simplest possible configuration for observation of exotic physics of PT-symmetric Hamiltonian [38]. In analogy to optical cases, spatially-distributed balanced gain and loss can be readily realized with an active negative-resistance converter [39, 40] and a resistor, which are connected through either capacitive or inductive links, as illustrated in Fig. 6-1(a). Figure 6-1(b) presents the proposed third-order (TO) PT-symmetric WPT systems with an equivalent circuit model shown in Fig. 6-1(a) (type **ii**). In this case, the transmitter, repeater, and receiver are represented by the $-RLC$, LC , and RLC oscillators, respectively. Here, inductive couplings between

the neighboring oscillators are the identical, and coupling between the transmitter and receiver is ignorable. These coupled the $-RLC$, LC , and RLC oscillators are analogous to “electronic” molecules with gain, neutral and loss characteristics, obeying a PT -symmetric Hamiltonian. Applying Kirchhoff’s laws to this circuit, the system can be described by Liouvillian formalism:

$$\mathcal{L}\Psi = \frac{d\Psi}{d\tau}, \quad (6-1)$$

$$\mathcal{L} = \begin{pmatrix} 0 & 0 & 0 & 1 & 0 & 0 \\ 0 & 0 & 0 & 0 & 1 & 0 \\ 0 & 0 & 0 & 0 & 0 & 1 \\ -\frac{1-\kappa^2}{1-2\kappa^2} & \frac{\kappa}{1-2\kappa^2} & -\frac{\kappa^2}{1-2\kappa^2} & \frac{1}{\gamma} \frac{1-\kappa^2}{1-2\kappa^2} & 0 & -\frac{1}{\gamma} \frac{\kappa^2}{1-2\kappa^2} \\ \frac{\kappa}{1-2\kappa^2} & -\frac{1}{1-2\kappa^2} & \frac{\kappa}{1-2\kappa^2} & -\frac{1}{\gamma} \frac{\kappa}{1-2\kappa^2} & 0 & \frac{1}{\gamma} \frac{\kappa}{1-2\kappa^2} \\ -\frac{\kappa^2}{1-2\kappa^2} & \frac{\kappa}{1-2\kappa^2} & -\frac{1-\kappa^2}{1-2\kappa^2} & \frac{1}{\gamma} \frac{\kappa^2}{1-2\kappa^2} & 0 & -\frac{1}{\gamma} \frac{1-\kappa^2}{1-2\kappa^2} \end{pmatrix},$$

where $\Psi \equiv (q_1, q_2, q_3, \dot{q}_1, \dot{q}_2, \dot{q}_3)^T$, q_k and \dot{q}_k correspond to the charge stored on the capacitor and the displacement current in the k -th oscillator (the subscripts, 1, 2 and 3 denote the active, neutral and passive tanks), $\tau \equiv \omega_0 t$, the natural frequency of the neutral LC tank, the gain-loss parameter (or non-Hermiticity) $\gamma = R^{-1} \sqrt{L/C}$, the coupling strength characterized by the rescaled mutual inductance $\kappa = M/L$, $\omega_0 = 1/\sqrt{LC}$ and all (angular) frequencies are measured in units of ω_0 .

The effective Hamiltonian can be written as $H_{eff} = i\mathcal{L} (H_{eff}\Psi = i\partial_\tau \Psi)$, which is non-Hermitian ($H_{eff}^\dagger \neq H_{eff}$) and symmetric with respect to the PT transformation, namely $[\mathcal{PT}, H_{eff}] = 0$, with

$$\mathcal{P} = \begin{pmatrix} \mathbf{J} & 0 \\ 0 & \mathbf{J} \end{pmatrix} \text{ and } \mathcal{T} = \begin{pmatrix} \mathbf{I} & 0 \\ 0 & -\mathbf{I} \end{pmatrix} \mathcal{K}, \quad (6-2)$$

where \mathbf{J} is an 3×3 anti-diagonal identity matrix, and \mathcal{K} conducts the operation of complex conjugation. These operations in conjunction leave the system unaltered. The system has six eigenvalues or eigenfrequencies, which can be derived from the secular equation as (in units of ω_0):

$$\omega_{1,2} = \pm 1, \quad \omega_{3,4} = \pm \sqrt{\frac{2\gamma^2 - 1 - \sqrt{1 - 4\gamma^2 + 8\gamma^4 \kappa^2}}{2\gamma^2(1 - 2\kappa^2)}}, \quad \text{and} \quad \omega_{5,6} = \pm \sqrt{\frac{2\gamma^2 - 1 + \sqrt{1 - 4\gamma^2 + 8\gamma^4 \kappa^2}}{2\gamma^2(1 - 2\kappa^2)}}. \quad (6-3)$$

The corresponding eigenmodes can be expressed in the form of

$$\Phi_n = \left(a_n e^{-i\phi_n}, b_n e^{i\phi'_n}, a_n e^{i\phi_n}, -i\omega a_n e^{-i\phi_n}, -i\omega b_n e^{i\phi'_n}, -i\omega a_n e^{i\phi_n} \right)^T, \quad \text{where} \quad a_n, b_n \in \mathbb{R}.$$

The dynamics (temporal response) of the PT system are the linear combination of all eigenmodes of the system,

yielding $\Psi(\tau) = \sum_{n=1}^6 c_n \Phi_n e^{-i\omega_n \tau}$ where the coefficient c_n depends on initial conditions. By inspecting

Eq. (6-3), one can identify three different regimes, separated by the exceptional points

$\gamma_{EP,\pm} = \sqrt{1 \pm \sqrt{1 - 2\kappa^2}} / (2\kappa)$. First, when $\gamma \in [\gamma_{EP,+}, \infty]$, the eigenfrequencies are real ($\omega_n \in \mathbb{R}$) and

$\mathcal{PT} \Phi_n = \Phi_n$ such that the PT -symmetry is exact. When $\gamma \in [\gamma_{EP,-}, \gamma_{EP,+}]$, the eigenfrequencies

become complex conjugate pairs ($\omega_n \in \mathbb{C}$), signaling a transition to the broken phase where

$\mathcal{PT} \Phi_n \neq \Phi_n$. Finally, when $\gamma < \gamma_{EP,-}$, all eigenfrequencies are imaginary. In time-transient

responses [see section 6-5], one may observe an oscillatory motion that consists of the

superposition of all harmonics. In the broken phase, due to the positive imaginary part of complex

eigenfrequencies, the eigenmodes grow exponentially in time, and, thus, the system exhibits an

unstable, underdamped behavior. Beyond the point of critical damping ($\gamma_{EP,-}$), modes are either exponentially growing or decaying eigenmodes in time. Such a phase is referred to an overdamped mode, with exponential responses arising in the temporal dynamics of charges and displacement currents.

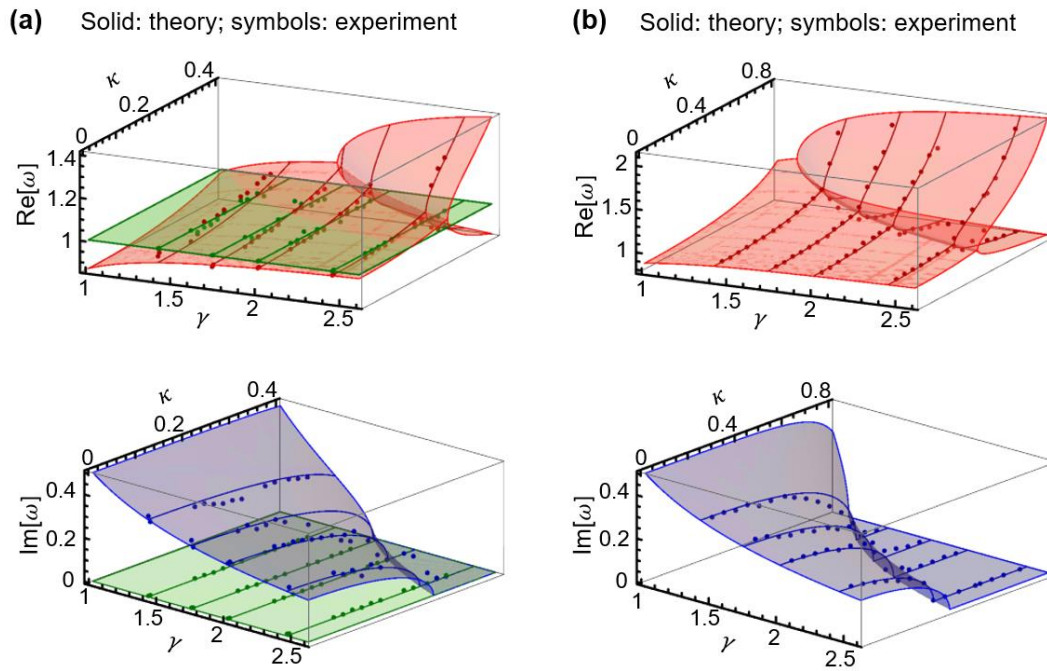


Figure 6-2. Evolution of the real (top) and imaginary (bottom) parts of eigenfrequencies as a function the gain-loss parameter γ and the coupling strength κ , for the **a** third-order and **b** standard PT-symmetric electronic systems in Fig. 6-1(a) (see type i and ii).

We note that the eigenfrequencies, $\omega_{1,2} = \pm 1$, are locked to the natural frequency of the LC tank and are independent of K and γ in the eigenspectrum, as can be seen in Fig. 6-2(a); the corresponding eigenmodes also do not experience the PT phase transition. If a TO-PT circuit is exploited to build a WPT system, the invariant and real eigenfrequency ensures that wireless powering is a robust and stable. In this system, high-efficiency power transfer takes place at ω_0 , and the performance is rather insensitive to the transverse offset between the receiver and the transmitting module (i.e., K variations) and to changes in the receiver's load impedance (i.e., γ variations). I note that such a dark-mode behavior is not found in the standard PT-symmetric system, as can be seen in Fig. 6-2(b), as its eigenfrequencies are always a strong function of K and γ [29, 41].

If a signal generator with periodically varying electromotive force is connected to the TO-PT circuit, the forced oscillations arise in the system. In the WPT case, a continuous-wave RF source (steady-state time-harmonic excitation) is connected to the $-RLC$ oscillator (transmitter). In the normal-mode analysis, an AC source with generator impedance Z_0 [Ω] can be seen as a negative resistance $-Z_0$. This is because while a positive resistor causes energy dissipations, a negative resistor represents an energy source. Therefore, if the signal generator is connected to a series $-RLC$ tank, a negative-resistance converter (NRC) with an equivalent resistance of $-(R - Z_0)$ must be used to maintain the gain and loss balance, necessary for PT physical systems. After the substitution of time-harmonic charge distributions in each oscillator, $q_k = A_k e^{i\omega\tau}$, the eigenfrequencies (resonant frequencies found in the circuit's spectral response) are zeros of the polynomial equation $|H_{eff} - \omega_n \mathbf{I}|$. I should note that the positive and negative frequency solutions are essentially identical. I must remove this redundancy by considering only the positive signs.

From the circuit viewpoint, the input impedance looking into the $-RLC$ tank from the signal generator is given by:

$$Z_{in} = Z_0 \left\{ 1 - \eta + i \frac{\gamma \eta}{\omega} (\omega^2 - 1) - i \frac{\gamma \eta \kappa^2 \omega^3 [\omega + i \gamma (\omega^2 - 1)]}{\omega (\omega^2 - 1) - i \gamma [\omega^4 (\kappa^2 - 1) + 2\omega^2 - 1]} \right\} \quad (6-4)$$

where $\eta = R/Z_0$. The reflection coefficient Γ measured at the input of the generator can be written as:

$$\begin{aligned} \Gamma &= \frac{Z_{in} - Z_0}{Z_{in} + Z_0} \\ &= \frac{\prod_{n=1}^6 \omega - \omega_n}{2\omega \left[\omega (\omega^2 - 1) + i \gamma (1 - 2\omega^2 - (\kappa^2 - 1)\omega^4) \right] + \prod_{n=1}^6 \omega - \omega_n}. \end{aligned} \quad (6-5)$$

where ω_n is the n -th eigenfrequency of the system in Eq. (6-3). In the exact PT-symmetric phase, three sharp reflection dips are obtained at the real eigenfrequencies. The reflectionless property is attributed to the impedance matching, namely, $Z_{in} = Z_0$, that is achieved at the resonant frequencies ($\omega = \omega_n$). In the broken phase, there is only one dip in the reflection spectrum, as the $\omega_n = \pm 1$ modes always exist in the TO-PT system.

The energy balance at the resonant frequency clarifies the spectral behavior of the TO-PT electronic system. At ω_n (corresponding to a specific eigenmode ϕ_n), the real power produced by the signal generator is given by $P_s = \frac{1}{2} |\dot{q}_1|^2 (-Z_0)$. The complex power delivered to the PT circuit is

$$P_{in} = -P_{gain} + P_{loss} + 2j\tilde{\omega} \left[\left(\sum_{k=1}^3 W_{m,k} - W_{e,k} \right) + W'_m \right] \text{ where } \tilde{\omega} = \omega_n \omega_0, \text{ the powers gained from the negative-}$$

resistance element and dissipated by the resistor are $P_{\text{gain}} = -\frac{1}{2} |\dot{q}_1|^2 (R - Z_0)$ and $P_{\text{loss}} = \frac{1}{2} |\dot{q}_3|^2 R$, respectively, the average electric energy stored in each capacitor $W_{e,k} = \frac{1}{4} \frac{|\dot{q}_k|^2}{C} = \frac{1}{4} \frac{|\dot{q}_k|^2}{\tilde{\omega}^2 C}$, the average magnetic energy stored in each inductor $W_{m,k} = \frac{1}{4} |\dot{q}_k|^2 L$, and the average magnetic energy stored in the coupled magnetic flux $W'_m = \frac{1}{2} M \dot{q}_1 \dot{q}_2^* + \frac{1}{2} M \dot{q}_2^* \dot{q}_3$. At the resonant frequencies, the average magnetic and electric stored energies are equal, i.e., $\sum_{k=1}^3 W_{e,k} = \sum_{k=1}^3 W_{m,k} + W'$, and the power delivered to the load resistance is real, i.e. $P_{\text{in}} = \frac{1}{2} |\dot{q}_1|^2 Z_0^2 = \frac{1}{2} a_n^2 Z_0^2$. Here, the net transfer of energy from gain to loss reach a balance condition, as $P_{\text{in}} + P_s = 0$. Further, the zero reflection at resonant frequencies can be explained by the fact that power extracted from an external source P_s is equal to that dissipated in the PT circuit P_{in} . This case is analogous to the conjugate matching condition with zero return loss (reflection), for which under a fixed generator impedance, the maximum power transfer occurs when the power lost in the source $|P_s|$ (which is considered as "gain" in the non-Hermitian open electronic system) is equal to a load in electronic circuits. At the resonant frequencies $(\omega_1, \dots, \omega_g)$, the power transfer efficiency defined as $\eta_{\text{T}} = P_{\text{loss}} / (P_s + P_{\text{gain}})$ is equal to 100 %.

In practical WPT applications, a multi-coil scheme shown in Fig. 6-1(a) (type iii) is usually used, in attempt to increase the total transfer distance. Here, I also study specific higher-order PT-symmetric electronic systems composed of an $-RLC$ oscillator and an RLC oscillator, which are remotely coupled via $N-2$ neutral intermediators ($N > 3$), as shown in Fig. 6-1(a) (type iii). This multi-element PT-symmetric system can still be described by the Liouvillian formalism

$d\Psi/d\tau = i\mathbf{H}_{eff}\Psi$, where Ψ is the modal column vector of dimensionality N and \mathbf{H}_{eff} is the effective non-Hermitian Hamiltonian of dimensionality $N \times N$. I find that the multi-stage PT-symmetric circuits with an array of neutral repeaters (type iii in Fig. 6-1(a)) share the same eigenfrequencies as those in Eq. (6-3) [see Method]. In addition, there are $2(N-2)$ eigenfrequencies that are independent of γ and κ (i.e., flat lines in the eigenspectrum) [see Method], which could also be of interest for WPT applications.

6.3 Experimental demonstration of WPT system with third-order PT symmetry

As a proof-of-concept demonstration, a TO-PT-symmetric WPT system was designed to wirelessly charge a robot car (Sparkfun Redbot-Arduino IDE) having a receiver mounted underneath it, as shown in Fig. 6-1(b) [see also Method]. The receiver is equivalent to an RLC resonator, of which the power taken by the AC-to-DC rectifier and battery (NH22NBP-NiMH 9V) is represented by a load resistance ($50\ \Omega$). The transmitter comprising an LC tank connected to an RF source with generator impedance $Z_0 = 50\ \Omega$. In the Hamiltonian analysis, since the RF source is represented by $-Z_0$ (gain), the transmitter can be seen as an $-RLC$ resonator. If the load impedance is greater (smaller) than Z_0 , a negative resistance element [39, 40] (resistor) must be used. As shown in Fig. 6-1(b), the receiver and transmitter were wirelessly linked via an intermediate LC resonator. These three active, neutral and passive resonators form the TO-PT-symmetric electronic system in Fig. 6-1(a). The transmitter was positioned on a linear translation stage with rotating platform, of which the tilt angle can be precisely controlled by a linear actuator (servomotor SG90). In our experiment, the repeater was stationary and separated from the receiver (transmitter) coil by a center-to-center distance d_R (d_T). The DC servomotor controlled by the LabVIEW-programmed provided a real-time positioning function to adjust the coupling strength

between the transmitter and repeater coils, such that it is equal to the coupling strength between the receiver and repeater coils. This action ensures that PT symmetry is preserved. I also used a control algorithm based on the pulse width modulation (PWM) for determining the required tilt angle of the transmitter coil, in response to deviation in the alignment of receiver and repeater coils [see Method].

We first study the evaluation of complex eigenfrequencies as a function of γ and κ for the TO-PT and standard-PT (without the neutral LC repeater) circuits. Experimental and theoretical results shown in Fig. 6-2 are represented by the dots and isosurfaces, respectively. Here, in all three resonators, the coil inductance $L = 15 \mu\text{H}$, the coupling strength κ varies from 0.01 to 0.77 and the capacitance of ceramic capacitors (SMA-GRM022XX series) C varies from 100 pF to 3 μF (which tunes γ from 1 to 2.5). In the receiver, the load resistance $R = 50 \Omega$. I note that the green isosurface in Fig. 6-2(a) representing $\omega_1 = 1[\omega_0]$ ($\omega_0 / 2\pi \approx 1.3 \text{ MHz}$) is a flat plain in the real domain, which reveals that in the spectral response there exists a resonance which is independent of γ and κ . Such an interesting characteristics is ideal for making robust and efficient WPT systems. This non-bifurcated dark-mode is, however, not allowed in the standard PT-symmetric system [Fig. 6-2(b)] and other currently existing WPT systems [6, 22]. The bifurcation effect is observed in both standard- and TO-PT systems, which, although can be exploited to realize γ, κ -ultrasensitive wireless sensors [27-30, 42], may not be suitable for wireless powering applications, since the bifurcation effect demands sophisticated frequency-tracking and/or adaptive impedance matching algorithms.

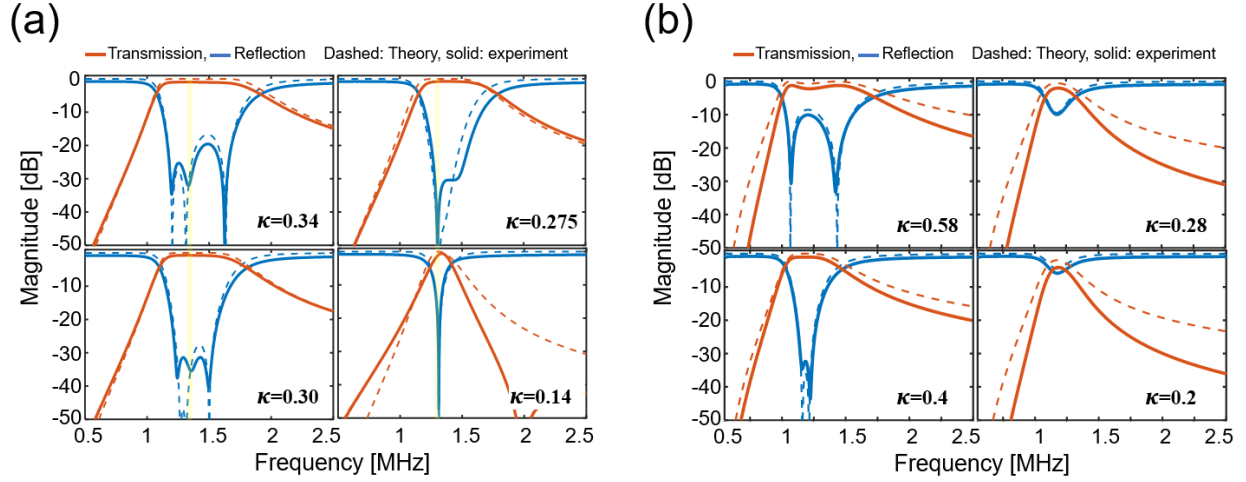


Figure 6-3 Evolution of reflection and transmission spectra for the **a** third-order with the coupling strength κ varied from 0.14 to 0.34 and **b** standard PT-symmetric WPT systems with the coupling strength κ varied from 0.2 to 0.58. Experimental and theoretical results are denoted by solid and dashed lines, respectively.

Figure 6- 3(a) and (b) report reflection and transmission coefficient versus frequency for the TO-PT and standard-PT WPT systems, respectively; here, the capacitance is fixed to 980 PF ($\gamma = 2.47$) and the coupling strenght is varied from 0.58 to 0.14 (corresponding to a change in d_R from 20 mm to 90 mm, caused by the software-controlled motion of the robot car). In order to characterize the transmission spectrum, the *LC* tank in the receiver was connected to a cable attached to the vector network analyzer. From Fig. 6-3, I find a good agreement between theoretical (obtained with Eq. (6-5)) and measurement results. The experimental results show that at any arbitrary coupling strength, the transmittance (power transfer efficiency here) can be greater than 90 % at frequency $\omega_0 / 2\pi \approx 1.3$ MHz . In contrast, the transmittance of the standard-PT WPT system drops in the weak coupling condition, as can be seen in Fig. 6-3(b), due to the bifurcation effect observed in Fig. 6-2(b).

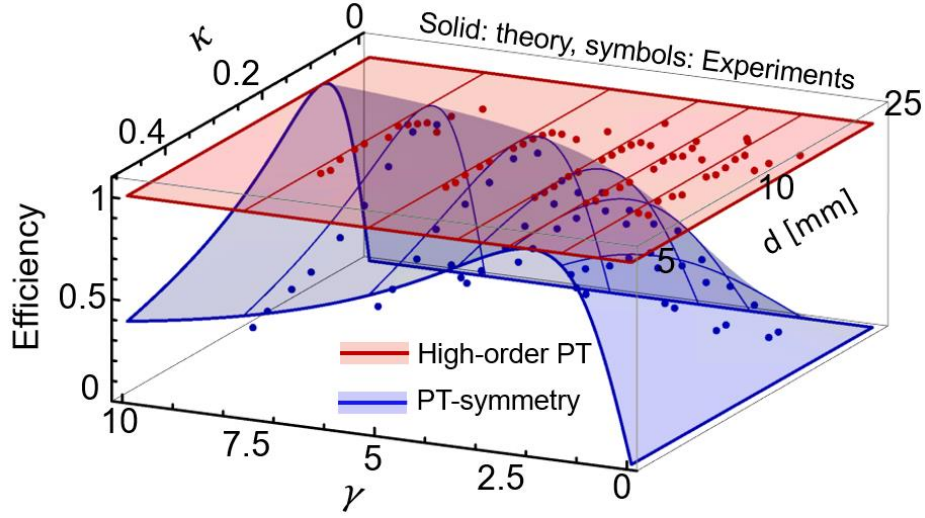


Figure 6-4 Efficiency of power transfer as a function of the gain-loss parameter γ and the coupling strength κ , for the frequency-locked (1.3 MHz) standard and third-order PT-symmetric WPT systems, here d is the center to center distance between two neighbor coil.

Finally, I compare the transfer efficiency ($\eta_T = |T|^2$) as a function of the coupling strength and the gain-loss parameter for the TO-PT and standard-PT WPT systems, whose theoretical efficiencies are shown as red and blue isosurfaces in Fig. 6-4. The measurement results represented by dots in Fig. 6-4 agree excellently with theoretical dependency. In our experiments, the receiver capacitor was varied ($C = 100 \text{ pF} - 3 \text{ }\mu\text{F}$) and the coupling strength is tuned with respect to d_R ($\kappa = 0.01 - 0.6$). For the TO-PT WPT system, the resonance at $\omega_0 / 2\pi \approx 1.3 \text{ MHz}$ is invariant with respect to different PT phases. On the other hand, a frequency-locked standard-PT WPT system fails to sustain a consistently high efficiency due to the bifurcation effect. In fact, the standard-PT

WPT system exhibits a high transfer efficiency only when an optimal set up of κ and γ is used (which renders an eigenfrequency equal to the operating frequency). Besides, the standard-PT setup does not function well at weak coupling because of symmetry breaking which results in complex eigenfrequencies and relevant reflection (return loss). As evident from Fig. 6-4, our experimental results provide clear evidence that the TO-PT-symmetric arrangement can provide superior performance and robustness compared to existing WPT systems, without any need of sweeping frequency or multiple adaptive matching stages. Last but not least, the TO-PT WPT systems could be robust against changes in γ , associate with fluctuations in the receiver's load impedance. For example, the electrochemical fatigue or the heat damage of battery could change the load resistance or capacitance. In this case, the two bifurcating eigenfrequencies in the TO-PT circuit [see Fig. 6-2(a)] can be exploited for monitoring the receiver's status and the battery lifetime. This unique feature combining simultaneous wireless charging and sensing may pave a promising new route towards the next generation of WPT systems. This technique could also benefit various industrial and medical applications, such as microwave ablation, hyperthermia, and cancer therapy, in which knowing the time-varying γ caused by physical forces (e.g., temperature or pressure) or chemical reaction during the transmission of electrical power would be very important.

6.4 Method

Generalized theory for higher-order PT WPT systems

Here, I consider the generalized higher-order PT-symmetric electronic system, which comprises an $-RLC$ oscillator and an RLC oscillator that are remotely coupled via $N-2$ neutral intermediators ($N > 3$), as shown in Fig. 6-1(a) (type iii). Such a multi-state scheme is also commonly seen in practical WPT applications, attempting to increase

the transfer distance between the power supplier and receiver. This multi-element PT-symmetric system can still be described by the Liouvillian formalism $d\Psi/d\tau = i\mathbf{H}_{eff}\Psi$, where Ψ is the modal column vector of dimensionality N and \mathbf{H}_{eff} is the effective non-Hermitian Hamiltonian of dimensionality $N \times N$. Specifically, by setting the coupling strength between two neutral intermediators as κ , and that between the gain (loss) oscillator and its neighboring repeater as $\kappa' = \kappa\sqrt{2}$, the eigenfrequencies of \mathbf{H}_{eff} are found to be roots of the following transcendental equations:

$$\begin{cases} (x^2 - 4\kappa^2)V_{\alpha}^{\text{even}} = 0 \text{ and } \alpha = \frac{N-2}{2}, \text{ for } N = 4, 6, 8, \dots \\ (\omega^2 - 1)(x^2 - 4\kappa^2)V_{\alpha}^{\text{odd}} = 0 \text{ and } \alpha = \frac{N-3}{2}, \text{ for } N = 5, 7, 9, \dots \end{cases} \quad (6-6)$$

where

$$\begin{aligned} V_{\alpha}^{\text{even}} &= \prod_{\beta=0}^{\alpha-1} x' - (2\kappa A_{\alpha\beta})^2, \\ V_{\alpha}^{\text{odd}} &= \prod_{\beta=0}^{\alpha-1} x' - (2\kappa B_{\alpha\beta})^2, \\ , x &= \left(\frac{\omega^2 - 1}{\omega^2} \right)^2 + \left(\frac{1}{\gamma\omega} \right)^2, x' = \left(1 - \frac{1}{\omega^2} \right)^2, A_{\alpha\beta} = \sin\left(\frac{\pi}{2} \frac{2\beta+1}{2\alpha+1} \right), B_{\alpha\beta} = \sin\left(\frac{\pi}{2} \frac{\beta+1}{\alpha+1} \right), \end{aligned}$$

and $\beta = 0, 1, 2, \dots, \alpha-1$. If N is an odd number, eigenfrequencies are given by:

$$\omega_n = \pm 1, \pm \sqrt{\frac{2\gamma^2 - 1 \pm \sqrt{1 - 4\gamma^2 + 16\gamma^4\kappa^2}}{2\gamma^2[1 - 4\kappa^2]}}, \pm \frac{1}{\sqrt{1 \pm 2\kappa A_{\alpha\beta}}}. \quad (6-7)$$

If N is an even number, eigenfrequencies are given by:

$$\omega_n = \pm \sqrt{\frac{2\gamma^2 - 1 \pm \sqrt{1 - 4\gamma^2 + 16\gamma^4 \kappa^2}}{2\gamma^2 [1 - 4\kappa^2]}}, \pm \frac{1}{\sqrt{1 \pm 2\kappa B_{\alpha\beta}}}. \quad (6-8)$$

From Eqs. (6-7) and (6-8), I find that the multi-stage PT-symmetric circuits with an array of neutral repeaters exhibit the γ -dependent eigenfrequencies that are identical to those of the three-elements setup. In addition, there are $2(N-2)$ discrete eigenfrequencies that are independent of γ . All positive eigenfrequencies are bounded in the range: $\omega_n \in [1/\sqrt{1+2\kappa}, 1/\sqrt{1-2\kappa}]$. It is interesting to note that the γ - and κ -independent eigenfrequencies ± 1 exist only in higher odd-order PT-symmetric circuits, which could be of interest for wireless power transfer applications.

6.5 Dynamic control of PT symmetry in circuits

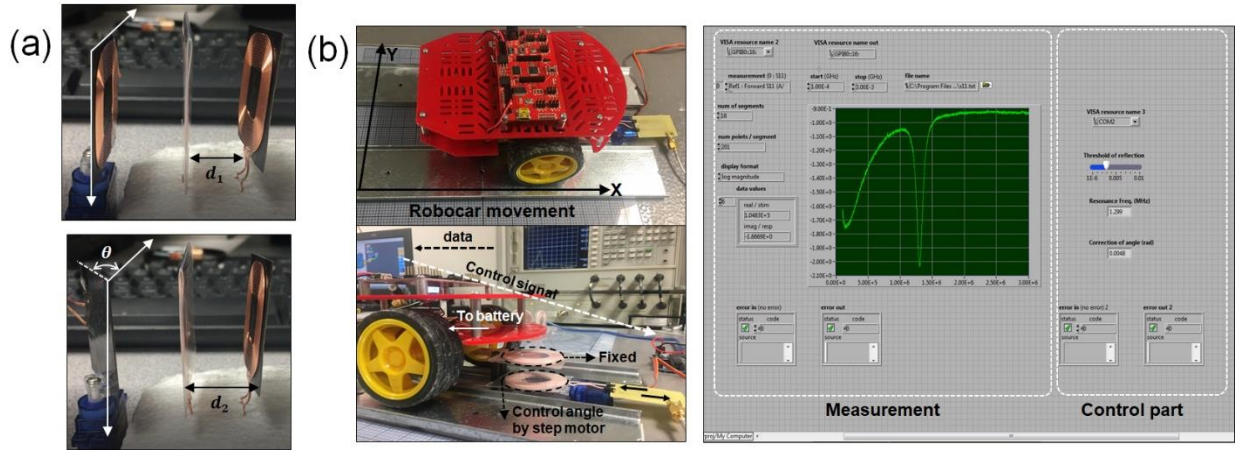


Figure 6-5 **a** Control of the tilt angle of the transmitter coil by a servo motor SG90. **b** Measurement setup for the TO-PT WPT system which wirelessly charges a robot car battery (left), and the LabVIEW interface for the feedback control of rotation of the transmitter coil (right).

The motion of the robot car (Redbot) was controlled by a pair of hobby Gearmotor-140 RPM (DG01D-A130GEARMOTOR) motorized by the H-bridge motor driver (TB6612FNG). The gearmotors was powered by a rechargeable Nickel-Metal Hydride battery (NH22NBP-NiMH 9V). The motion of robot car would change the coupling strength between the receiver coil (on the robot car) and the stationary intermediate coil [see Section 6.4]. Therefore, the coupling strength between the transmitter and intermediate coils must be dynamically adjusted to maintain the PT-symmetry condition. In this work, the real-time rotation control of the transmitter coil (which alters its magnetic coupling to the repeater) was done by a DC servo motor (SG90) linked to the LabVIEW program, as illustrated in Fig. 6-5(a). The angle of rotation (α) for the transmitter coil is determined by the measured reflection at the resonance frequency. To this end, the relationship between the coupling strength and the reflection coefficient was measured for different values of α . In practical test environments, I first send a PWM (Pulse Width Modulation) signal to the RF circuit and track the minimum reflection at the resonance frequency by continuously altering α . The detected reflection coefficient was used as the input of a PC-hosted peripheral LabVIEW program, which contains the measurement and control modes, as shown in Fig. 6-5(b). In the measurement mode, the vector network analyzer (Agilent HP-8753S) as an ultrafast-switching frequency synthesizer was connected to the General Purpose Interface Bus (GPIB). The archived reflection data was dumped into the control mode as a reference for adjusting the tilt angle of the transmitter coil.

6.6. Temporal responses of the third-order PT-symmetric circuit

The dynamics (time-transient response) of the TO-PT system is a linear combination of all eigenmodes $\Psi(\tau) = \sum_{n=1}^6 c_n \Phi_n e^{-i\omega_n \tau}$, where the coefficient c_n depends on initial condition, and eigenfrequencies and eigenmodes can be expressed in Eq. (6-3) and the following:

$$\Phi_n = \left(a_n e^{-i\phi_n}, b_n e^{i\phi'_n}, a_n e^{i\phi_n}, -i\omega a_n e^{-i\phi_n}, -i\omega b_n e^{i\phi'_n}, -i\omega a_n e^{i\phi_n} \right)^T, \quad (6-9)$$

where $a_n, b_n \in \mathbb{R}$,

$$\begin{aligned} \phi_{1,2} &= \pm \pi / 2, \\ \phi_{3,4} &= \pm \frac{1}{2i} \ln \left[\frac{\kappa^2 Y_1}{\sqrt{2}(1-2\kappa^2)(Y_1 + \Delta) / Z_1 + \kappa^2(Y_1 - 4) + 2} \right], \\ \phi_{5,6} &= \pm \frac{1}{2i} \ln \left[-\frac{\kappa^2 Z_2^2}{(1-2\kappa^2) \left[\sqrt{2}(Z_2 + \Delta / Z_2) - \kappa^2(Y_2 + 4) + 2 \right]} \right], \end{aligned} \quad (6-10)$$

$$X = \sqrt{1-4\gamma^2+8\gamma^4\kappa^2}, \quad \Delta = 2\gamma^2(1-2\kappa^2), \quad Y_{1,2} = \pm 1 \mp 2\gamma^2 + X, \quad \text{and} \quad Z_{1,2} = \sqrt{(\pm 1 \mp 2\kappa^2)Y_{1,2}}.$$

Considering for example a constant electromotive force (emf) at the initial moment $\Psi(\tau=0) = (1, 0, 0, 0, 0, 0)^T$, the evolution of charges stored on capacitors are presented in Fig. 6-9.

In the *PT*-symmetric phase, one may observe an oscillatory motion that consists of the superposition of three harmonics [Fig. 6-9]. In the broken phase, due to the positive imaginary part of complex eigenfrequencies, the eigenmodes grow exponentially in time, and, thus, the system exhibits an unstable, underdamped behavior [Fig. 6-10]. Beyond the point of critical damping ($\gamma_{EP,-}$), which leads to either exponentially growing or decaying eigenmodes in the temporal responses. Such a phase is referred to an overdamped mode, with exponential responses arising in the temporal dynamics of charges and displacement currents.

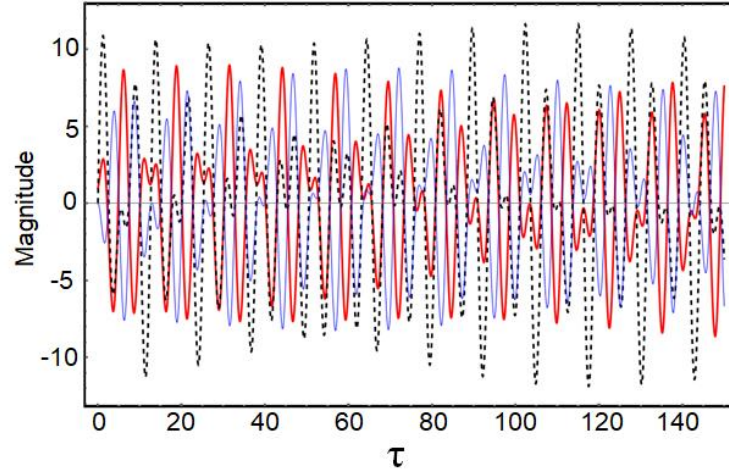


Figure 6-6 q v.s. τ . Temporal dynamics of the charge stored in the capacitor of the $-RLC$ tank (red line), LC tank (black dashed line), and RLC tank (blue line); here, $\gamma = 1.5$ and $\kappa = 0.5$, which lead to the exact phase with $\omega_{1,2,3,4,5,6} = \pm 1, \pm 1.4844$, and ± 0.9527 .

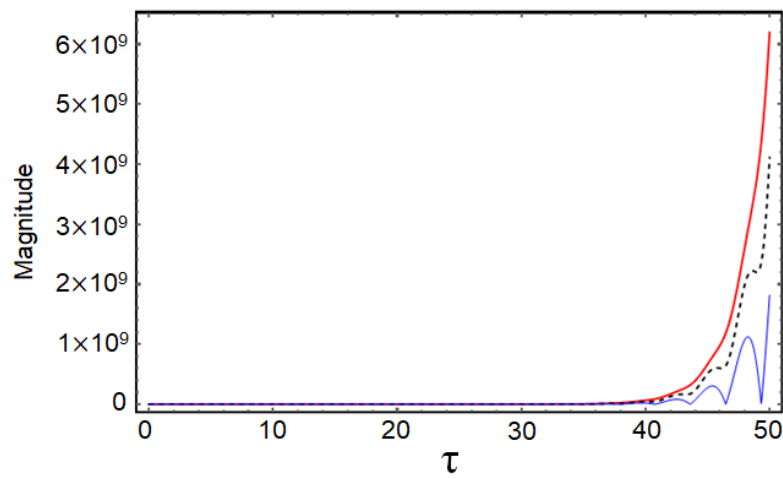


Figure 6-7 $|q|$ v.s. τ . Temporal dynamics of the absolute charge stored in the capacitor of the $-RLC$ tank (red line), LC tank (black dashed line), and RLC tank (blue line); here, $\gamma = 1$ and $\kappa = 0.5$, which lead to the broken phase.

6.7 Characterization of magnetic coupling strength

We have characterized effects of vertical and horizontal misalignments on the coupling strength between coils. In our experimental setups for higher-order PT-symmetric circuits, only adjacent coils are magnetically coupled, while the coupling between nonadjacent coils is negligible. The mutual inductance between two coils can be computed using Neumann formula [25]. Fig. 6-8 compares the theoretical and experimental results for the coupling strength (mutual inductance normalized by the coil's self-inductance). Both results are found to be in a good agreement.

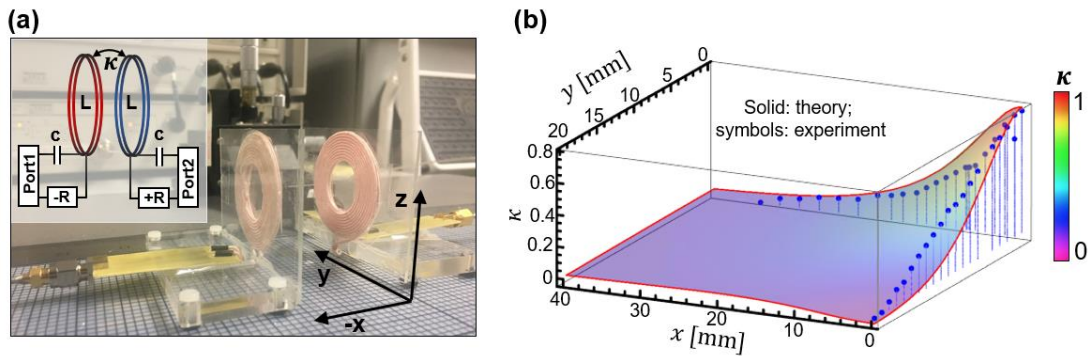


Figure 6-8 **a** Measurement setup for the coupling strength between two coils. **b** Coupling strength as a function of distance (x, y); theoretical and experimental results are denoted by the isosurface and symbols.

6.8 Evolvement of reflection as a function of magnetic coupling strength

In the exact symmetry phase of the TO-PT electronic system, $\kappa_{EP} = \sqrt{4\gamma^2 - 1} / (2\sqrt{2}\gamma^2)$ is a transition point between the exact and broken symmetry phases. Figs. 6-9(a) and S4(b) show the experimental setup, as well as the transmission coefficient for the standard-PT and TO-PT electronic systems. In the TO-PT system, when $\kappa > \kappa_{EP}$ (exact PT-symmetric phase), real eigenfrequencies leads to a transmission near unity, and, as expected, three resonant transmission peaks are found. When $\kappa < \kappa_{EP}$ (broken PT-symmetric phase), two transmission peaks associated with the bifurcating eigenfrequencies would disappear, whereas one peak locked at the same frequency is found in both exact and broken PT-symmetric phases. This effect is, however, missed in the standard-PT system.

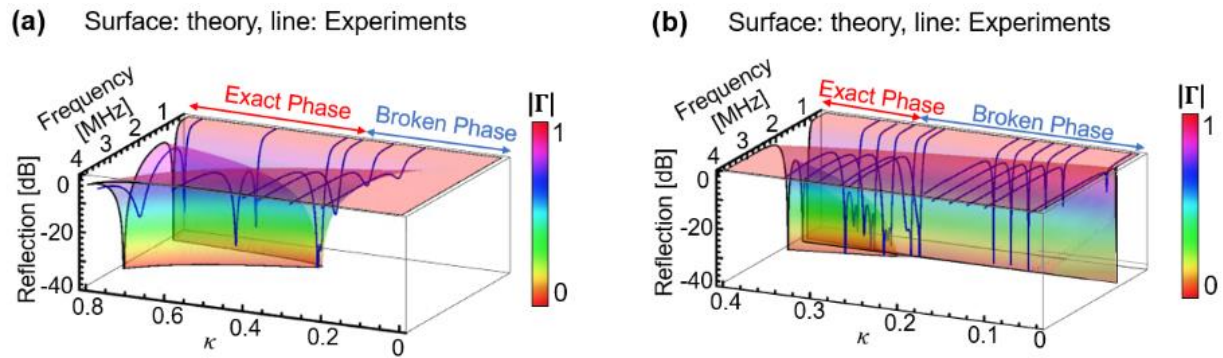


Figure 6-9 Magnitude of reflection coefficient as a function of frequency and coupling strength for the **a** standard and **b** third-order PT-symmetric circuits.

6.9 Evolvement of transmission coefficient as a function of intermediate coil loss

The concept of PT-symmetry requires a lossless resonator as an intermediate coil in the third order PT-symmetric system in order for the entire circuit system to be invariant under operations of spatial reflection P and time reversal T, this condition, however, is an unphysical assumption that a perfectly lossless resonator is available to serve as a neutral element. Figs. 6-10(a) and S5(b) show the effect of loss of the intermediate coil on the system response. Here, the intermediate coil loss, r , is normalized to the loss/gain resistance, R , of the loss/gain RLC tanks, $\varsigma = \frac{r}{R}$. Fig. 6-S5(a) presents the evaluation of the real parts of eigenfrequencies as a function of the coupling strength κ , for

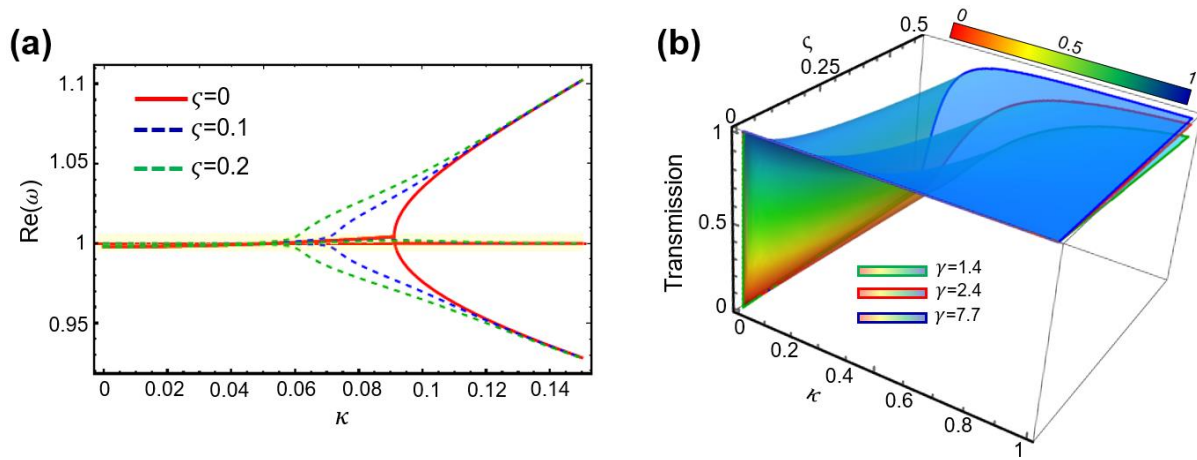


Figure 6-10 **a** Evolution of the real parts of eigenfrequencies as a function of the coupling strength κ , here, $\gamma=7.7$ and $\varsigma=0, 0.1$, and 0.2 , **b** Transmission coefficient at the resonance frequency $\omega=1$, as a function of the coupling strength κ , and loss in the intermediate coil for $\gamma=1.4, 2.4$, and 7.7 , for the third-order PT-symmetric circuits.

three different loss ratio of the intermediate coil, $\varsigma = 0, 0.1, \text{ and } 0.2$, here the non-hermiticity parameter is fixed to $\gamma = 7.7$. It is worth mentioned that note, the non-zero loss of the intermediate coil, breaks the PT-symmetry of the system, consequently the system eigen frequencies are not purely real even in exact PT phase, however, it is observed that one of the circuit system complex eigen frequency has a real part near unit, $\text{Re}(\omega) \approx 1$ which is γ, κ – independent similar to the PT-symmetric system, the imaginary part of the eigen frequency, however, is a function of γ, κ , and intermediate coil loss, this non-zero imaginary part of the eigen frequency means that the transmission coefficient reduces from unit at the resonance frequency, $\omega = 1$, as it is shown in Fig. 6-S5(b). I note that the imaginary part of the eigen frequency is larger for weak coupling regime compared with strong coupling which results reduction of efficiency in weak coupling strength and become worst as the intermediate coil loss is increased. This prediction is matched to the experimental results in Fig. 6-4.

6.10 Conclusion

We have shown that a real and constant eigenfrequency in specific higher-order PT-symmetric electronic systems can be exploited to realize a robust wireless power transfer platform locked to the frequency of operation. In this PT system, the two-dimensional eigenspectrum is flat with respect to changes in coupling strength and gain-loss parameter, thus ensuring a consistently-high efficiency that is not influenced by distance and alignment between the receiver and the power supplier (which include the transmitter and repeater(s)). Additionally, this effect is prominent even for the mid-range wireless power transfer with loose magnetic coupling. The third-order PT circuit

described here also exhibits bifurcating eigenfrequencies, which, together with the invariant and real one, may enable a multi-functional platform that provides wireless charging and sensing at the same time. Further studies may make a breakthrough in dynamic and alignment-free wireless charging technology with extended range.

REFERENCES

- [1] X. Lu, D. Niyato, P. Wang, D. I. Kim, and Z. Han, "Wireless charger networking for mobile devices: Fundamentals, standards, and applications," *IEEE Wireless Communications*, vol. 22, no. 2, pp. 126-135, 2015.
- [2] T. Campi, S. Cruciani, F. Palandrani, V. De Santis, A. Hirata, and M. Feliziani, "Wireless power transfer charging system for AIMDs and pacemakers," *IEEE transactions on microwave theory and techniques*, vol. 64, no. 2, pp. 633-642, 2016.
- [3] S. R. J. C. T. o. P. E. Hui and Applications, "Past, present and future trends of non-radiative wireless power transfer," vol. 1, no. 1, pp. 83-91, 2016.
- [4] C. C. Mi, G. Buja, S. Y. Choi, and C. T. Rim, "Modern advances in wireless power transfer systems for roadway powered electric vehicles," *IEEE Transactions on Industrial Electronics*, vol. 63, no. 10, pp. 6533-6545, 2016.
- [5] S. Zhang, Z. Qian, J. Wu, F. Kong, and S. Lu, "Wireless charger placement and power allocation for maximizing charging quality," *IEEE Transactions on Mobile Computing*, vol. 17, no. 6, pp. 1483-1496, 2017.
- [6] H. Dai *et al.*, "Safe charging for wireless power transfer," *IEEE/ACM Transactions on Networking (TON)*, vol. 25, no. 6, pp. 3531-3544, 2017.
- [7] S. Assawaworrarit, X. Yu, and S. Fan, "Robust wireless power transfer using a nonlinear parity-time-symmetric circuit," *Nature*, vol. 546, p. 387, 2017.
- [8] T. Kan, F. Lu, T.-D. Nguyen, P. P. Mercier, and C. C. Mi, "Integrated Coil Design for EV Wireless Charging Systems Using LCC Compensation Topology," *IEEE Transactions on Power Electronics*, vol. 33, no. 11, pp. 9231-9241, 2018.
- [9] A. Triviño- Cabrera and J. A. Aguado, "Wireless Charging for Electric Vehicles in the Smart Cities: Technology Review and Impact," *Transportation and Power Grid in Smart Cities: Communication Networks and Services*, pp. 411-426, 2018.
- [10] J. Zhou, B. Zhang, W. Xiao, D. Qiu, and Y. Chen, "Nonlinear parity-time-symmetric model for constant efficiency wireless power transfer: application to a drone-in-flight wireless

- charging platform," *IEEE Transactions on Industrial Electronics*, vol. 66, no. 5, pp. 4097-4107, 2019.
- [11] L. V. Bewley, *Flux linkages and electromagnetic induction*. Macmillan, 1952.
 - [12] S. Nikolettseas, Y. Yang, and A. Georgiadis, *Wireless power transfer algorithms, technologies and applications in ad hoc communication networks*. Springer, 2016.
 - [13] A. Kurs, A. Karalis, R. Moffatt, J. D. Joannopoulos, P. Fisher, and M. Soljačić, "Wireless Power Transfer via Strongly Coupled Magnetic Resonances," *Science*, vol. 317, no. 5834, pp. 83–86, Jul. 2007.
 - [14] Zierhofer, C. M., and E. S. Hochmair. "The class-E concept for efficient wide-band coupling-insensitive transdermal power and data transfer." 1992 14th Annual International Conference of the IEEE Engineering in Medicine and Biology Society, vol. 2, pp. 382-383, 1992.
 - [15] Ziaie, Babak, et al. "A self-oscillating detuning-insensitive class-E transmitter for implantable microsystems." *IEEE Transactions on Biomedical Engineering*, vol. 48, no.3, pp. 397-400, 2001.
 - [16] D. Ahn and S. Hong, "Wireless Power Transmission With Self-Regulated Output Voltage for Biomedical Implant," *IEEE Trans. Ind. Electron.*, vol. 61, no. 5, pp. 2225–2235, 2013.
 - [17] H. Dai, X. Wang, A. X. Liu, H. Ma, G. Chen, and W. Dou, "Wireless charger placement for directional charging," *IEEE/ACM Transactions on Networking (TON)*, vol. 26, no. 4, pp. 1865-1878, 2018.
 - [18] Q. Li and Y. C. Liang, "An inductive power transfer system with a high-Q resonant tank for mobile device charging," *IEEE Transactions on power electronics*, vol. 30, no. 11, pp. 6203-6212, 2015.
 - [19] T.-D. Yeo, D. Kwon, S.-T. Khang, and J.-W. Yu, "Design of maximum efficiency tracking control scheme for closed-loop wireless power charging system employing series resonant tank," *IEEE Transactions on Power Electronics*, vol. 32, no. 1, pp. 471-478, 2016.

- [20] P. K. S. Jayathurathnage, A. Alphones, and D. M. Vilathgamuwa, "Optimization of a wireless power transfer system with a repeater against load variations," *IEEE Transactions on Industrial Electronics*, vol. 64, no. 10, pp. 7800-7809, 2017.
- [21] S. R. Hui, "Magnetic resonance for wireless power transfer," 2016.
- [22] J. I. Agbinya, *Wireless power transfer*. River Publishers, 2015.
- [23] Z. Lin, X. Li, R. Zhao, X. Song, Y. Wang, and L. Huang, "High-efficiency Bessel beam array generation by Huygens metasurfaces," *Nanophotonics*, vol. 8, no. 6, pp. 1079-1085, 2019.
- [24] J. O. Mur-Miranda *et al.*, "Wireless power transfer using weakly coupled magnetostatic resonators," *Proc. IEEE ECCE*, pp. 4179-4186, 2010.
- [25] T. Imura and Y. Hori, "Maximizing air gap and efficiency of magnetic resonant coupling for wireless power transfer using equivalent circuit and Neumann formula," *IEEE Transactions on industrial electronics*, vol. 58, no. 10, pp. 4746-4752, 2011.
- [26] J. Schindler, Z. Lin, J. M. Lee, H. Ramezani, F. M. Ellis, and T. Kottos, "PT-symmetric electronics," *Journal of Physics A: Mathematical and Theoretical*, vol. 45, no. 44, p. 444029, 2012.
- [27] M. Hajizadegan, M. Sakhdari, and P.-Y. Chen, "PT-Symmetric inductive displacement sensors," in *2018 IEEE MTT-S International Microwave Workshop Series on Advanced Materials and Processes for RF and THz Applications (IMWS-AMP)*, 2018: IEEE, pp. 1-3.
- [28] H. Hajizadegan, M. Sakhdari, S. Liao, and P. Y. Chen, "High-sensitivity wireless displacement sensing enabled by PT-symmetric telemetry," *IEEE Transactions on Antennas and Propagation*, vol. 67, pp. 3445 – 3449, 2019.
- [29] P.-Y. Chen *et al.*, "Generalized parity–time symmetry condition for enhanced sensor telemetry," *Nature Electronics*, vol. 1, no. 5, pp. 297 – 304, 2018.
- [30] M. Sakhdari, M. Hajizadegan, Y. Li, M. M.-C. Cheng, J. C. Hung, and P.-Y. Chen, "Ultrasensitive, parity-time-symmetric wireless reactive and resistive sensors," *IEEE Sensors Journal*, 2018.

- [31] C. M. Bender and S. Boettcher, "Real Spectra in Non-Hermitian Hamiltonians having PT -Symmetry," *Physical Review Letters*, vol. 80, no. 24, pp. 5243-5246, 1998.
- [32] M. C. Rechtsman, "Optical sensing gets exceptional," *Nature*, vol. 548, p. 161, 2017.
- [33] K. G. Makris, R. El-Ganainy, D. N. Christodoulides, and Z. H. Musslimani, "PT-symmetric optical lattices," *Physical Review A*, vol. 81, no. 6, p. 063807, 2010.
- [34] R. Fleury, D. Sounas, and A. Alù, "An invisible acoustic sensor based on parity-time symmetry," *Nature Communications*, Article vol. 6, p. 5905, 2015.
- [35] M. Sakhdari, N. M. Estakhri, H. Bagci, and P.-Y. Chen, "Low-threshold lasing and coherent perfect absorption in generalized PT-symmetric optical structures," *Physical Review Applied*, vol. 10, no. 2, p. 024030, 2018.
- [36] Z. Lin, H. Ramezani, T. Eichelkraut, T. Kottos, H. Cao, and D. N. Christodoulides, "Unidirectional invisibility induced by PT-symmetric periodic structures," *Physical Review Letters*, vol. 106, no. 21, p. 213901, 2011.
- [37] H. Ramezani, T. Kottos, R. El-Ganainy, and D. Christodoulides, "Unidirectional nonlinear PT-symmetric optical structures," *Physical Review A*, vol. 82, no. 4, p. 043803, 2010.
- [38] J. Schindler, A. Li, M. C. Zheng, F. M. Ellis, and T. Kottos, "Experimental study of active LRC circuits with PT-symmetries," *Physical Review A*, vol. 84, no. 4, p. 040101, 10/13/2011.
- [39] M. P. Kennedy, "Chaos in the Colpitts oscillator," *IEEE Transactions on Circuits Systems*, vol. 41, no. 11, pp. 771-774, 1994.
- [40] B. Razavi, *RF microelectronics*. Prentice Hall New Jersey, 1998.
- [41] M. Sakhdari, M. Farhat, and P.-Y. Chen, "PT-symmetric metasurfaces: wave manipulation and sensing using singular points," *New Journal of Physics*, vol. 19, no. 6, p. 065002, 2017.
- [42] J. Wiersig, "Sensors operating at exceptional points: general theory," *Physical Review A*, vol. 93, no. 3, p. 033809, 2016.

VII. LOW-THRESHOLD LASING AND COHERENT PERFECT ABSORPTION IN THE GENERALIZED PT-SYMMETRIC OPTICAL STRUCTURES

Parts of this chapter have been presented in (Sakhdari et al., 2018, PR Applied). Copyright©2019, PRL.

Achieving exact balance between spatially separated gain and loss is generally considered as a weaker constraint for parity–time (PT)-symmetric classical wave systems [1]-[12]. Here, I introduce a generalized PT (gPT)-symmetric optical structures, which have an asymmetric and unbalanced gain/loss profile, while exhibiting similar scattering properties and PT phase transitions as traditional PT-symmetric optical systems around the design frequency. Particularly, I show that the concept of gPT-symmetry may help reducing the threshold gain in achieving newly discovered PT-enabled applications, such as the coherent perfect absorber (CPA)-laser and exceptional points. The concept proposed herein will facilitate the practice of PT-symmetric optical devices by offering greater design flexibility to tailor gain-loss profiles and their thresholds.

7.1 Coherent Perfect Absorber Laser

Very recently, PT-symmetric optics has attracted intense research interest because it provides an experimentally-accessible platform to study real eigenspectra in physical systems with non-Hermitian Hamiltonians [1]-[12]. Optical systems satisfying PT-symmetry usually consist of a lasing medium and its time-reversed lossy counterpart, of which gain and loss contributions are equally balanced and symmetrically distributed in space, e.g., an optical system with complex permittivities having a profile of $\varepsilon(\mathbf{r}) = \varepsilon^*(-\mathbf{r})$. [1],[2] During recent years, numerous intriguing optical phenomena and applications have been observed in PT-symmetric systems, such as

PT-symmetry phase transitions and exceptional points [1],[2], unidirectional reflectionless light propagation [3]-[5], negative refraction and sub-diffraction focusing [6], as well as optical isolators and circulators [7]. Particularly, a PT-symmetric optical system can behave simultaneously as a CPA that fully absorbs incoming waves and a laser oscillator that emits outgoing coherent waves. Such an optical device is referred to as CPA-laser [8]-[12] because it exhibits both lasing and coherent perfect absorption modes at the same frequency, switchable via adjusting amplitudes and phases of incoming waves.

In this project, instead of engineering optical structures with balanced loss and gain, as in traditional PT-symmetric systems [Fig. 7-1a], I investigate a generalized PT (gPT)-symmetric optical system [Fig. 7-1b], which could have net optical gain less than optical loss and vice versa, while displaying similar PT phase transitions and extraordinary scattering properties as traditional PT-symmetric system. More specifically, this gPT-symmetric system consists of the reciprocally scaled gain and loss, e.g., $\kappa^2 \epsilon(\mathbf{r})$ and $\epsilon^*(-\mathbf{r})/\kappa^2; \{\kappa \in \mathbb{R} : \kappa \geq 0\}$. It is therefore possible that loss is greater than gain in the gPT-symmetric CPA-laser, which in some sense similar to “loss-induced revival of lasing” [12].

7.2 The concept of the generalized PT-symmetric optical systems

Figure 7-1a features a traditional one-dimensional PT-symmetric optical system containing homogeneous, isotropic loss and gain media, whose permittivities are $\epsilon_{loss} = \epsilon_r + i\epsilon_i$ and $\epsilon_{gain} = \epsilon_{loss}^*$. [1]-[2] Assuming a deeply subwavelength thickness for gain/loss media, i.e., $t \ll \lambda$, this optical system can be described by a transmission-line model shown in Fig. 7-1a (bottom), which consists of two admittance sheets with complex-valued surface admittances:

$$Y_{s,loss} = Y_{s,r} + iY_{s,i} \approx j\omega\epsilon_{loss}t \text{ and } iY_{s,gain} = (iY_{s,loss})^*, \text{ where } \omega \text{ is the angular frequency [13].}$$

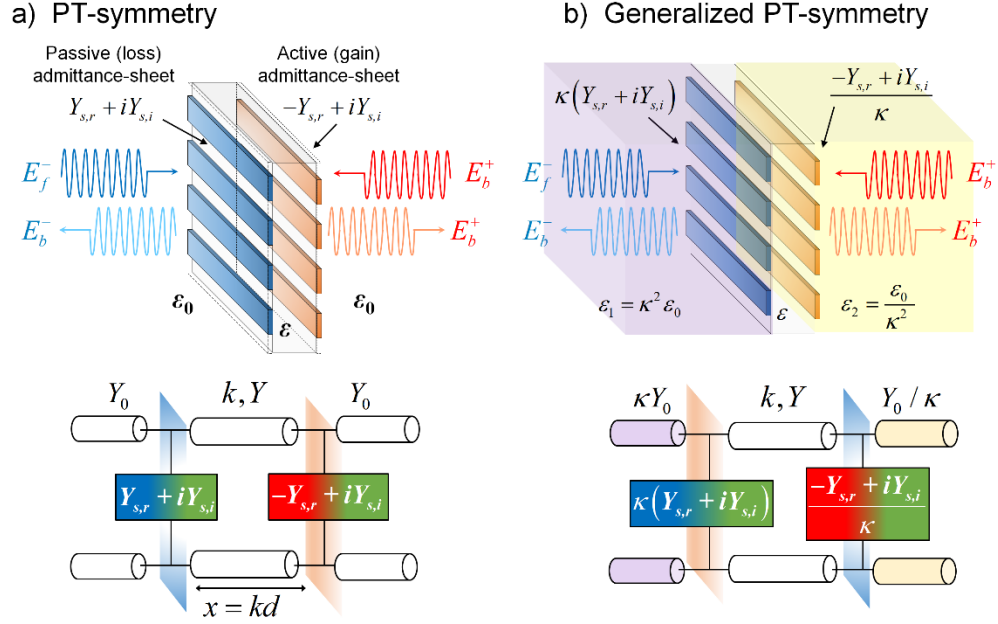


Figure 7-1 Schematics for (a) the PT-symmetric and (b) the generalized PT (gPT)-symmetric optical structures (top) comprising paired gain and loss components, and their corresponding transmission-line network model (bottom). Provided that the structured gain and loss media have subwavelength thickness and unit cells, their optical behaviors can be described by a surface admittance (or surface impedance). In the gPT-symmetric system, if the scaling coefficient $\kappa \neq 1$, the gain-loss balance, as a weaker constraint of PT-symmetry, can be broken, while the scattering properties remain the same at the design frequency.

On the interface of each admittance sheet, electric fields are nearly the same $E_t^+ = E_t^-$ and tangential magnetic fields are discontinuous: $\hat{n} \times (H_t^+ - H_t^-) = E_t^+ Y_s$. These two gain and loss sheets are separated by a dielectric slab with thickness d and admittance $Y = \sqrt{\varepsilon / \varepsilon_0} Y_0$, where admittance of background medium $Y_0 = \sqrt{\varepsilon_0 / \mu_0}$. Intuitively, such admittance sheets can also be realized with metasurfaces or two-dimensional nanomaterials [14],[15], e.g. graphene under equilibrium

(plasmon loss) [16] and population-inversion (plasmon gain) [17]. Figure 7-1b proposes the gPT-symmetric optical system, in which the surface admittance of the passive sheet and the admittance of its host substrate are scaled by the dimensionless scaling factor κ , whereas those of the active sheet and its substrate are scaled by $1/\kappa$. For the composite structures in Fig. 7-1, the electric field on left and right sides $E^{-(+)} = E_f^{-(+)} e^{ik^{-(+)}z} + E_b^{-(+)} e^{-ik^{-(+)}z}$ can be decomposed into forward- and backward-propagating waves, whose amplitudes are related by:

$$\begin{pmatrix} E_f^+ \\ E_b^+ \end{pmatrix} = \mathbf{M} \begin{pmatrix} E_f^- \\ E_b^- \end{pmatrix}, \quad (7-1)$$

where \mathbf{M} is the 2×2 transfer matrix, $E_{f(b)}$ is the amplitude of the forward (backward) traveling waves, the superscript $+(-)$ indicates left (right) of the composite structure, and k is the wave number. Since $\det(\mathbf{M}) = 1$, both PT- and gPT-symmetric systems exhibit reciprocal and unidirectional scattering. The transmission (t) and reflection (r) coefficients for left (L) and right (R) incidences can be expressed in terms of transfer matrix elements as $r_L = -M_{21}/M_{22}$, $r_R = M_{12}/M_{22}$ and $t_L = t_R = 1/M_{22}$. The scattering matrix linking incoming and outgoing waves is given by:

$$\mathbf{S} = \begin{pmatrix} t_L & r_R \\ r_L & t_R \end{pmatrix} \text{ and } \begin{pmatrix} E_f^+ \\ E_b^+ \end{pmatrix} = \mathbf{S} \begin{pmatrix} E_f^- \\ E_b^- \end{pmatrix}. \quad (7-2)$$

The validity of PT-symmetry imposes a generalized conservation relation on the scattering matrix:

$$\mathbf{S}^*(\omega) = \mathcal{P} \mathcal{T} \mathbf{S}(\omega) \mathcal{P} \mathcal{T} = \mathbf{S}^{-1}(\omega) [9], [18], \text{ where the parity operator } \mathcal{P} = \begin{pmatrix} 0 & 1 \\ 1 & 0 \end{pmatrix}, \text{ the time-reversal}$$

operator $\mathcal{T} = \begin{pmatrix} 0 & 1 \\ 1 & 0 \end{pmatrix} \mathcal{K}$, and \mathcal{K} is the complex conjugation operator. In addition, $\mathbf{M}^* = \mathbf{M}^{-1}$ and

$M_{22} = M_{11}^*$ can be similarly derived. For the gPT-symmetric system in Fig. 7-1b, scattering coefficients in \mathbf{S} can be derived using the transfer-matrix method as:

$$\begin{aligned} t_R = t_L &= -\frac{i2\kappa Y Y_0 \csc(x)}{\kappa \left[Y^2 + (Y_0 + iY_{s,i})^2 - Y_{s,r}^2 \right] + Y \left[Y_{s,i}(\kappa^2 + 1) - i(Y_0(\kappa^2 + 1) + Y_{s,r}(\kappa^2 - 1)) \right] \cot(x)}; \\ r_R &= \frac{(Y_0^2 + Y_{s,r}^2 + 2Y_0 Y_{s,r} + Y_{s,i}^2 - Y^2) \kappa + Y \left[i(Y_{s,r} + Y_0)(\kappa^2 - 1) - Y_{s,i}(\kappa^2 + 1) \right] \cot(x)}{\kappa \left[Y^2 + (Y_0 + iY_{s,i})^2 - Y_{s,r}^2 \right] + Y \left[Y_{s,i}(\kappa^2 + 1) - i(Y_0(\kappa^2 + 1) + Y_{s,r}(\kappa^2 - 1)) \right] \cot(x)}; \\ r_L &= \frac{(Y_0^2 + Y_{s,r}^2 - 2Y_0 Y_{s,r} + Y_{s,i}^2 - Y^2) \kappa - Y \left[i(Y_{s,r} - Y_0)(-\kappa^2 + 1) - Y_{s,i}(\kappa^2 + 1) \right] \cot(x)}{\kappa \left[Y^2 + (Y_0 + iY_{s,i})^2 - Y_{s,r}^2 \right] + Y \left[Y_{s,i}(\kappa^2 + 1) - i(Y_0(\kappa^2 + 1) + Y_{s,r}(\kappa^2 - 1)) \right] \cot(x)}, \end{aligned} \quad (7-3)$$

where the electrical length between two admittance sheets $x=kd$. From Eq. (3), I can readily find that if $x=(2n-1)\pi/2$ and n is a positive integer, all scattering coefficients become independent of κ , and, more interestingly, they are identical to those of the PT-symmetric setup in Fig. 7-1a, which are given by:

$$\begin{aligned} t_R = t_L &= -\frac{i2Y Y_0}{Y_0^2 + Y^2 + 2iY_0 Y_{s,i} - Y_{s,i}^2 - Y_{s,r}^2}; \\ r_R &= \frac{Y_0^2 - Y^2 + (Y_{s,r} + Y_{s,i})^2}{Y_0^2 + Y^2 + 2iY_0 Y_{s,i} - Y_{s,i}^2 - Y_{s,r}^2}; \\ r_L &= \frac{Y_0^2 - Y^2 + (Y_{s,r} - Y_{s,i})^2}{Y_0^2 + Y^2 + 2iY_0 Y_{s,i} - Y_{s,i}^2 - Y_{s,r}^2}. \end{aligned} \quad (7-4)$$

In this case, PT- and gPT-symmetric optical systems would share exactly the same \mathbf{S} and \mathbf{M} , and, therefore, a gPT-symmetric device, although having “unbalanced” gain and loss, can achieve similar optical scattering properties enabled by PT-symmetry. As a result, the optical structure in Fig. 7-1b can be considered as a “generalized” PT-symmetric system. In other words, the traditional PT-symmetric system in Fig. 7-1a is the degenerate case of the gPT-symmetric system with $\kappa=1$. Since PT- and gPT-symmetric systems share the same \mathbf{S} and its two eigenvalues $\lambda_{1,2}$,

the transition between the *symmetry* and *symmetry-breaking* phases, typical for PT-symmetric scatters, can also be found in the gPT-symmetric system. The phase transition can be characterized by the evolution of eigenvalues given by [18]: $\lambda_{1,2} = t \pm \sqrt{r_L r_R} = t \left(1 \pm i \sqrt{1/|t|^2 - 1} \right)$. In the symmetry phase, the two eigenvalues are nondegenerate and unimodular (i.e., $|\lambda_{\pm}| = 1$) and $|t| < 1$. In the broken-symmetric phase, they are non-unimodular (i.e., $\lambda_+ = 1/(\lambda_-)^*$) and $|t| > 1$, with a transition point called exceptional point where $\lambda_+ = \lambda_- = 1/(\lambda_+)^*$ and $t = 1$. The lasing mode does occur in the symmetry-breaking phase of PT- and gPT-symmetric systems with $|t| > 1$, since the asymmetric **S** and eigenmodes could trap the excitation for a longer time in the gain part of the medium, rather than in the loss part.

A laser oscillator, by definition, is an optical device that provides output fields $E_b^-, E_f^+ \neq 0$, even though input fields $E_f^-, E_b^+ \approx 0$. The coherent perfect absorption mode would otherwise require that $E_b^- = E_f^+ = 0$ and $E_f^-, E_b^+ \neq 0$. Hence, a laser is developed if $M_{22} = 0$ and an CPA is developed if $M_{11} = 0$. These two conditions, in general, do not occur simultaneously at the same frequency in the same system, but may be possible with the PT- and gPT-symmetric systems that allow $M_{22} = M_{11}^* = 0$. The occurrence of CPA and laser has recently been theoretically studied [8],[9] and experimentally demonstrated [10],[11]. These two exotic behaviors can be characterized by the overall output coefficient Θ , defined as the ratio of the total intensity of outgoing (reflected/transmitted) waves to that of the incoming waves:

$$\Theta = \frac{|E_b^-|^2 + |E_f^+|^2}{|E_f^-|^2 + |E_b^+|^2} = \frac{|1 + M_{12}\alpha|^2 + |\alpha - M_{21}|^2}{(1 + |\alpha|^2)/M_{22}^2}, \quad (7-5)$$

where $\alpha = E_b^+ / E_f^-$. I should emphasize that for $\alpha = M_{21}$, which yields vanishing of Θ , a CPA can be realized. On the other hand, for $\alpha \neq M_{21}$ (e.g. $\alpha = 0$ when considering only left-incident wave), the lasing mode is always obtained. For the PT-symmetric system in Fig. 7-1a, a CPA-laser can be attained in its breaking-symmetry phase, with a surface admittance profile:

$$Y_{s,loss} = Y_{s,r} + iY_{s,i} = Y_0 \sqrt{1 + (Y \csc(x) / Y_0)^2} + iY \cot(x); \quad (7-6a)$$

$$Y_{s,gain} = -Y_{s,r} + iY_{s,i}, \quad (7-6b)$$

which leads to $M_{22} = M_{11}^* = 0$. At the CPA-laser point, two eigenvalues of \mathbf{S} become zero and infinity, which respectively correspond to the CPA and lasing modes [9]. The CPA-laser can be similarly achieved in the generalized PT-symmetric system, but the required conditions become:

$$Y_{s,loss} = \kappa Y_0 \sqrt{1 + Y^2 / Y_0^2}; \quad (7-7a)$$

$$\text{and } Y_{s,gain} = -\kappa^{-1} Y_0 \sqrt{1 + Y^2 / Y_0^2}, \quad (7-7b)$$

where κ is the scaling factor. From Eq. (7), I note that in the gPT-symmetric system, two surface admittances must be purely real. Except for the special case of $\kappa = 1$, gain and loss are not equally balanced. Moreover, even if low-gain and high-loss media are paired (i.e. a large κ yielding $-\text{Re}[Y_{s,gain}] < \text{Re}[Y_{s,loss}]$), the CPA-laser point can still be attained. As a result, for $\alpha \neq M_{21}$, a low-threshold laser may be realized with a large κ . Likewise, a small κ , yielding net gain greater than loss in the system, can interestingly achieve coherent perfect absorption if $\alpha = M_{21}$. Such non-intuitive properties are somehow analogous to recently explored “loss-induced lasing” and “gain-induced absorption” effects [12].

7.3 Implementations of generalized PT-symmetric CPA-laser

In this Letter, I illustrate the gPT-symmetric system by examples of dispersive gain media with Lorentzian lineshape, whose complex-valued permittivity can be expressed as:

$$\varepsilon_{\text{gain}}(\omega) = \varepsilon_0 - \frac{\omega_p^2}{\omega_0^2 - \omega^2 + i\omega\gamma}, \quad (7-8)$$

where ω is the angular frequency, ω_p is the angular plasma frequency (here $\omega_p = 2\omega_0$), ω_0 is the angular resonance frequency, and γ is the linewidth of amplification governing the magnitude of resonance (here $\gamma = 0.198, 0.396$, and $1.99\omega_0$). In order to satisfy the Kramers-Kronig relation and causality, γ of an active medium must be positive. Further, a thin sheet of such a medium can be described by a surface conductivity $\sigma_{s,\text{gain}}(\omega) \approx -i\omega\varepsilon_{\text{gain}}(\omega)t$ or a surface admittance

$Y_{s,\text{gain}} = \sigma_{s,\text{gain}}$. At the design frequency ω_D (or wavelength λ_D) of the gPT-symmetric CPA-laser,

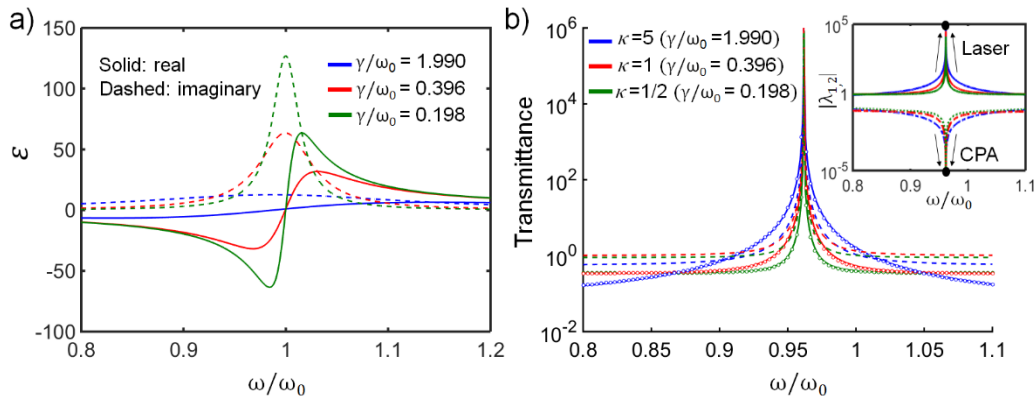


Figure 7-2 (a) Real (solid) and imaginary (dashed) parts of permittivity of active gain media with different linewidths of amplification γ . (b) Transmittance spectra of gPT-symmetric optical structures in Fig. 7-1b,

of which the amplifying metasurface made of gain media in (a); dashed lines and symbols represent analytical and full-wave simulation results, respectively. By varying the scaling coefficient κ , the CPA-laser point with eigenvalues going to zero and infinite (inset) can be achieved, regardless of the resonant gain magnitude. Here, I consider only one excitation source, and, thus, only the lasing mode is observed.

the amplifying and attenuating sheets are separated by a medium, with admittance $Y=Y_0$ and electrical length $x=\pi/2$. In order to satisfy the CPA-laser condition, $Y_{s,gain}(\omega_D)=-\sqrt{2}Y_0/\kappa$, as described in Eq. (7), this Lorentzian gain media must be patterned into proper metasurface structures. One possible structure can be an array of subwavelength strips with periodicity p and gap g [Fig. 7-1], whose equivalent surface admittance has an explicit form [see Appendix A]. The attenuating surface is assumed to be a resistive thin slab with constant conductivity (e.g. metals in the long wavelength region), resulting in $Y_{s,loss}(\omega_D)=\kappa\sqrt{2}Y_0$. Also, the host substrates for attenuating and amplifying sheets have a permittivity profile: $\epsilon_1=\kappa^2\epsilon_0$ and $\epsilon_2=1/\kappa^2\epsilon_0$, which respectively render material admittances κY_0 and Y_0/κ , as shown in Fig. 7-1b. For simplicity illustrating the gPT-symmetry, here I assume that both host substrates are lossless and non-dispersive. However, our theoretical results (not presented here) show that around the design frequency, the CPA-laser mode is robust to moderate substrate losses.

Figure 7-2b shows the transmittance ($T=|t|^2$) against the normalized frequency for different gPT-symmetric CPA-laser devices [Fig. 7-1b], illuminated by a single excitation source ($\alpha \neq M_{21}$).

The gain media in Fig. 7-2a with $\gamma = 0.198, 0.396$, and $1.99\omega_0$ (which render large, medium and

small resonant gain) are respectively utilized to realize gPT-symmetric CPA-laser devices with design frequency $\omega_D = 0.962\omega_0$ and scaling factor $\kappa = 1/2, 1$, and 5 . For each CPA-laser, the thickness and gap-to-period ratio of metasurface are fixed as $t = 0.004 \lambda_D$ and $g/p = 0.08$, while the optimal period p is calculated using the explicit formula to achieve the CPA-laser mode. For example, if $\kappa = 5$, the active metasurface with $Y_{s,gain}(\omega_D) = -\sqrt{2}Y_0 / \kappa$ is placed on the substrate with $\varepsilon_2 = \varepsilon_0 / 25$ (i.e., epsilon-near-zero (ENZ) material [19]), whereas the lossy sheet with $Y_{s,loss}(\omega_D) = \kappa\sqrt{2}Y_0$ is on a substrate with $\varepsilon_1 = 25\varepsilon_0$. From Fig. 7-2b, I find that regardless of γ , a lasing peak with gigantic transmittance/reflectance can be always be achieved at ω_D , implying that there is, in principle, no lasing threshold, namely lasing could happen even with a poor gain related to a large γ . Figure 7-2b also compares analytical results (lines) with full-wave simulations based on the finite-element method (dots) [20], showing good agreements around ω_D . The inset of Fig. 7-2b shows magnitudes of $\lambda_{1,2}$, which respectively approach infinity and zero at ω_D , typical of a CPA-laser. Figure. 3a presents contours of transmittance (T) as functions of κ and γ for this gPT-symmetric optical device under a single monochromatic excitation source with frequency of ω_D ; for each value of κ , permittivities of host substrates are changed accordingly and the metasurface's period are optimized to achieve the maximum transmittance/reflectance. From Fig. 7-3a, it is seen that for any arbitrary γ , the lasing mode can always be found by choosing a proper κ . Moreover, peaks of transmittance are consistent with the locus of optimal sets of κ and γ (white dashed line) that achieve $Y_{s,gain}(\omega_D) = -\sqrt{2}Y_0 / \kappa$.

Here, I also study lasing behaviors of an individual active metasurface and a traditional PT-symmetric CPA-laser, in order to make a fair comparison with the gPT-symmetric CPA-laser. Figure 7-3b is similar to Fig. 7-3a, but considering only the amplifying sheet, as shown in the inset of Fig. 7-3b. In this case, one side of the active metasurface is air and the other side is dielectric substrate with permittivity $\varepsilon = \varepsilon_0 / \kappa^2$. In this case, the lasing mode with infinite reflectance/transmittance occurs when $Y_{s,gain} = -(1 + \sqrt{\varepsilon})Y_0$, exhibiting an upper bound: $Y_{s,gain} \big|_{\kappa \rightarrow \infty} \simeq -Y_0$, possible with an ENZ substrate. As can be seen in Fig. 7-3b, in sharp contrast to

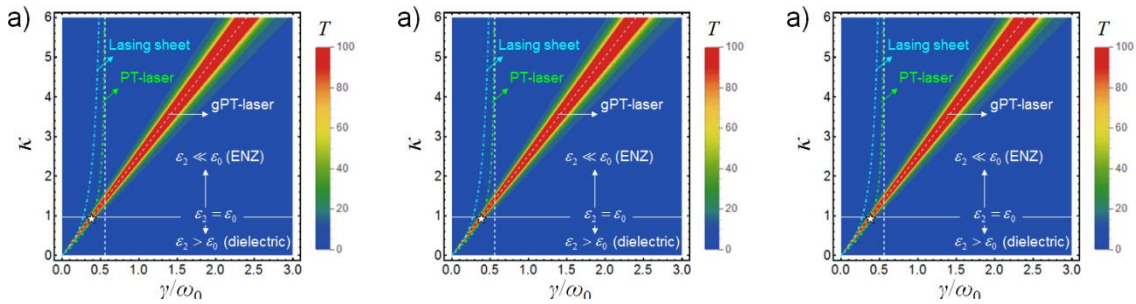


Figure 7-3 Contours of Transmittance as functions of γ and κ for the gPT-symmetric optical system in Fig. 7-1(b); here, the locus of optimal (γ, κ) sets, giving the lasing effect, for an individual active metasurface (inset of Fig. 7-3(b)), PT- and gPT-symmetric optical systems are presented for comparison. For a large γ , corresponding to a weak resonant gain, the lasing effect can only be achieved with the gPT-symmetric metasurfaces. If $\kappa = 1$, the system would degenerate into the common PT-symmetric setup, as highlighted with a star. (b) is similar to (a), but for an individual active metasurface, showing an upper bound for lasing in terms of γ . Contours of Transmittance as functions of γ and κ (electrical length between amplifying and attenuating surfaces) for the PT-symmetric optical system in Fig. 7-1(a), varying the dielectric permittivity of spacer $\varepsilon = \varepsilon_0 / \kappa^2$. In this case, a physical bound similar to an individual active metasurface in (b) is still obtained.

The gPT-symmetric metasurface, it is not always feasible to attain the lasing mode at γ . As γ increases beyond the threshold $\gamma_{th} = 0.56 \omega_0$, which makes $\text{Re}[\sigma_{gain}(\omega_D, \gamma_{th})] = -Y_0$, the real part of metasurface's surface admittance is always out of the upper bound of $-Y_0$ (remind that $\text{Re}[\sigma_{s,gain}] \leq \text{Re}[Y_{s,gain}] < 0$). Next, I consider the PT-symmetric optical system in Fig. 7-1a, with $iY_{s,loss} = (iY_{s,gain})^*$ and an intermediary medium with $\varepsilon = \varepsilon_0 / \kappa^2$ and $x = k_0 d / \kappa$. Figure 7-3c presents contours of T as functions of γ and κ for this PT-symmetric system, under a single monochromatic excitation source with frequency of ω_D ; the left, middle and right panels show results for $\kappa = 1, 1/2$ and 5, respectively, and for each set of κ and x , the active metasurface is optimized by fixing g/p to 0.08 and sweeping p to reach the maximum transmittance/reflectance. As can be seen in Fig. 7-3c, although it is possible to attain the CPA-laser mode in such a system, γ_{th} does exist for the lasing (single excitation source) and CPA (two excitation sources) modes. Although a large κ and a suitable electrical length $x = (2n-1)\pi/2$, leading to a CPA-laser condition of $Y_{s,r} = -Y_0 \sqrt{1 + (Y \csc(x) / Y_0)^2} \sim -Y_0$ and $Y_{s,i} = -Y_0 Y \cot(x) / Y_0 \sim 0$, may help increase γ_{th} , the maximum γ_{th} cannot be greater than $0.56 \omega_0$, analogous to that of an individual amplifying metasurface. Figure 7-3a also compares optimum γ against κ at the lasing point ω_D for the single metasurface amplifier (blue dashed line) [Fig. 7-3b], PT-symmetric metasurface with $x = \pi/2$ (green dashed line) [Fig. 7-3c], and the gPT-symmetric metasurface [Fig. 7-3a]. It is clearly evident that if the constituent gain media of active metasurface has a large γ , corresponding to a low

resonant gain, the lasing effect is only achievable in the gPT-symmetric system that essentially has no gain threshold.

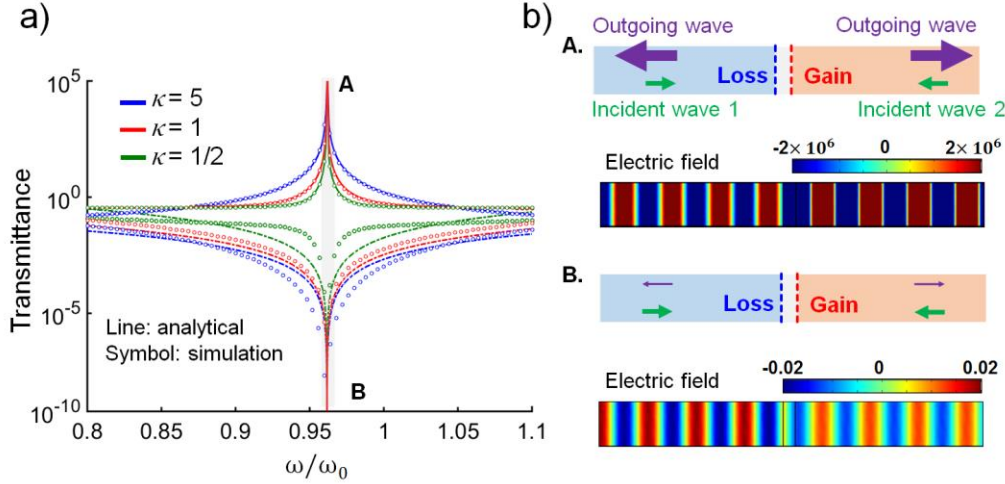


Figure 7-4 (a) Transmittance spectra for CPA-laser devices based on gPT-symmetric metasurfaces, which are designed using different scaling coefficients; here, lasing and CPA modes are excited by single and two coherent incident waves. (b) Snapshots of electric fields for the gPT-symmetric CPA-laser in (a) ($\kappa = 1$), operated in the lasing mode (top) and the CPA mode (bottom).

Finally, I also study the CPA mode of gPT-symmetric composite structures in Fig. 7-2b. Figure 7-4a shows their output coefficient Θ against frequency; here, the solid lines represent the one-sided illumination with $\alpha = 0$ (which leads to the lasing mode) and the dashed lines represent the doubled-sided illuminations with $\alpha = M_{21}$; for all three cases, $M_{21} = i(-1 + \sqrt{2})$ at ω_d . It can be seen from Fig. 7-4a that the coherent perfect absorption and lasing can be obtained at the same frequency by simply switching the amplitude and phase of the second incoming signal. I should note that variations in transmittance/reflectance (i.e., modulation depth) of gPT-symmetric CPA-laser can be quite dramatic, which is ideal for optical switching and modulation applications.

Figure 7-4b presents the full-wave simulation results for the CPA (top panel) and lasing (bottom panel) effects at ω_D , showing that the outgoing wave can be either fully suppressed or amplified, depending on how the coherent signal is tuned. Again, there is no threshold gain for a gPT-symmetric CPA.

7.4 Metasurface designs

According to impedance boundary conditions, a discontinuity on the tangential magnetic field on the metasurface is related to the induced averaged surface current by the surface admittance. Assuming perfectly-conducting strips of negligible thickness are aligned parallel to the magnetic field of the transverse magnetic (TM) incident wave, the equivalent surface admittance can be explicitly written as [13]:

$$Y_s = -i2\alpha Y_{eff}, \quad (7-9)$$

$$\begin{aligned} \text{and } \alpha &= \frac{k_{eff} p}{\pi} \left[\ln \left(\csc \left(\frac{\pi g}{2p} \right) \right) + \frac{1}{2} \sum_{n=-\infty, n \neq 0}^{\infty} \left(\frac{2\pi}{\sqrt{(2\pi n)^2 - k_{eff}^2 p^2}} \frac{1}{|n|} \right) \right] \\ &\approx \frac{k_{eff} p}{\pi} \ln \left(\csc \left(\frac{\pi g}{2p} \right) \right) \quad \text{if } k_{eff} p \ll 2\pi \end{aligned} \quad (7-10)$$

where $Y_{eff} = \sqrt{\epsilon_{eff} / \mu_0}$, $k_{eff} = \omega \sqrt{\mu_0 \epsilon_{eff}}$, $\epsilon_{eff} = (\epsilon + \epsilon_0) / 2$. When a dispersive medium is used to constitute the metasurface, the surface admittance is usually complex-valued, $Y_s = Y_{s,r} + iY_{s,i}$, where the surface conductance $Y_{s,r}$ and the surface susceptance $Y_{s,i}$ account for the gain/loss magnitude and the net stored energy in the near field, respectively. When considering a complex-valued sheet conductivity, the surface impedance of metasurface should be modified as [1]:

$$Y_s = \left[\frac{1}{\sigma_s (1 - g/p)} + i \frac{1}{2\alpha Y_{eff}} \right]^{-1}. \quad (7-11)$$

7.5 Scattering from an individual metasurface

The scattering coefficients for an individual metasurface, placed on the interface between the left-sided background medium with admittance Y_0 and the right-sided medium with admittance Y , are given by:

$$\begin{aligned} r_L &= \frac{Y_0 - Y - Y_{s,gain}}{Y + Y_0 + Y_{s,gain}}, \quad r_R = \frac{Y - Y_0 - Y_{s,gain}}{Y + Y_0 + Y_{s,gain}}, \\ t_R &= \sqrt{Y_0 / Y} (1 + r_R), \quad t_L = \sqrt{Y / Y_0} (1 + r_L), \quad \text{and} \quad t_R = t_L. \end{aligned} \quad (7-12)$$

The lasing condition that achieves transmittance/reflectance peaks can be derived as:

$$Y_{s,gain} = -(1 + \sqrt{\varepsilon})Y_0. \quad (7-13)$$

7.5 Conclusion

Controlling the balance between gain and loss was the regarded as the necessary condition to realize a PT-symmetric classical wave system. Here, I have introduced the idea of a generalized PT-symmetric system with unbalanced, reciprocally-scaled gain and loss, which interestingly possesses similar scattering properties and eigenvalue bifurcations as typical PT-symmetric systems. Specifically, I have demonstrated this idea using the PT-symmetric metasurfaces, and shown that the CPA-laser mode can be realized even though the system has a small net gain. Our results may provide new directions for advances in PT-symmetry and its electromagnetic, acoustic, and circuit applications via breaking the gain/loss balance and eradicating the threshold gain/loss for reaching exotic properties of PT-symmetry, such as the and CPA-laser mode and exceptional points.

REFERENCES

- [1] K. G. Makris, R. El-Ganainy, and D. N. Christodoulides, Beam Dynamics in PT Symmetric Optical Lattices, *Phys. Rev. Lett.* **100**, 103904 (2008).
- [2] R. El-Ganainy, K. G. Makris, D. N. Christodoulides, and Z. H. Musslimani, Theory of Coupled Optical PT-Symmetric Structures, *Opt. Lett.* **32**, 2632-2634 (2007).
- [3] Z. Lin, H. Ramezani, T. Eichelkraut, T. Kottos, H. Cao, and D. N. Christodoulides, “Unidirectional invisibility induced by PT-symmetric periodic structures.” *Phys. Rev. Lett.* **106**, 213901 (2011).
- [4] H. Ramezani, T. Kottos, R. El-Ganainy, and D. N. Christodoulides, Unidirectional Nonlinear PT – Symmetric Optical Structures, *Phys. Rev. A* **82**, 043803 (2010).
- [5] R. Fleury, D. L. Sounas, and A. Alù, “An invisible acoustic sensor based on parity-time symmetry,” *Nat. Communications* **6**, 5905 (2015).
- [6] R. Fleury, D. L. Sounas, and A. Alù, “Negative refraction and planar focusing based on parity-time symmetric metasurfaces,” *Phys. Rev. Lett.* **113**, 023903 (2014).
- [7] B. Peng, Ş. K. Özdemir, F. Lei, F. Monifi, M. Gianfreda, G. L. Long, S. Fan, F. Nori, C. M. Bender, and L. Yang, Parity-Time-Symmetric Whispering-Gallery Microcavities, *Nat. Phys.* **10**, 394 (2014).
- [8] S. Longhi, PT -Symmetric Laser Absorber, *Phys. Rev. A* **82**, 031801(R) (2010).
- [9] Y. D. Chong, L. Ge, and A. D. Stone, “PT-Symmetry Breaking and Laser-Absorber Modes in Optical Scattering Systems,” *Phys. Rev. Lett.* **106**, 093902 (2011).
- [10] Y. Sun, W. Tan, H. Q. Li, J. Li, and H. Chen, “Experimental demonstration of a coherent perfect absorber with PT phase transition,” *Phys. Rev. Lett.*, **112**, 143903 (2014).
- [11] Z. J. Wong, Y. L. Xu, J. Kim, K. O'Brien, Y. Wang, L. Feng, and X. Zhang, “Lasing and anti-lasing in a single cavity,” *Nat. Photon.* **10**, 796-801 (2016).
- [12] B. Peng, S. K. Özdemir, S. Rotter, H. Yilmaz, M. Liertzer, F. Monifi, C. M. Bender, F. Nori, and L. Yang, “Loss-induced suppression and revival of lasing.” *Science* **346**, 328-332 (2014).

- [13] S. Tretyakov, *Analytical modeling in applied electromagnetics*, Artech House, London (2003).
- [14] P. Y. Chen, M. Farhat, H. Bağcı, “Graphene metascreen for designing compact infrared absorbers with enhanced bandwidth,” *Nanotechnol.* **26**, 164002 (2015).
- [15] P. Y. Chen, and J. Jung, *PT*-Symmetry and Singularity-Enhanced Sensing Based on Photoexcited Graphene Metasurfaces. *Phys. Rev. Appl.* **5**, 064018 (2016).
- [16] P. Y. Chen, and A. Alù, “Atomically thin surface cloak using graphene monolayers,” *ACS Nano* **5**, 5855-5863 (2011).
- [17] D. Svintsov, V. Ryzhii, A. Satou, T. Otsuji, and V. Vyurkov, Carrier-Carrier Scattering and Negative Dynamic Conductivity in Pumped Graphene, *Opt. Express* **22**, 19873 (2014).
- [18] L. Ge, Y. D. Chong, and A. D. Stone, Conservation Relations and Anisotropic Transmission Resonances in One-Dimensional *PT*-Symmetric Photonic Heterostructures, *Phys. Rev. A* **85**, 023802 (2012).
- [19] I. Liberal, and N. Engheta, “Near-zero refractive index photonics,” *Nat. Photonics* **11**, 149–158 (2017).
- [20] COMSOL Multiphysics: <http://www.comsol.com>.

VIII. CONCLUSION AND FUTURE WORKS

I have applied PT -symmetry and the generalized PTX -symmetry condition to RF sensor telemetry with a particular focus on compact wireless micro-mechatronic sensors, actuators and wireless power transfer. I have theoretically studied and experimentally demonstrated the possibility of using the PT -symmetry concept to wirelessly read the (lossy) capacitive and resistive sensors, with high spectral resolution and high sensitivity. The proposed wireless sensing technique is potentially revolutionary, as it may be beneficial to a plurality of environmental, wearable, and implantable wireless sensors, as well as emerging applications in the fields of IoTs and RFIDs.

I have introduced the notion of divergent exceptional points in multi-elements PT -symmetric electronic systems and shown that it can lead to gigantic eigenfrequency splitting. I have tested the predictions experimentally in a PT -symmetric “gain-neural-loss” electronic trimer and have demonstrated that, indeed, the eigenfrequency bifurcation around the divergent exceptional point can be quite dramatic, with a physical upper bound approaching infinity. This work may not only open new avenues for high-performance RF sensors, but I also have extended it to wireless power transfer system.

I have shown that a real and constant eigenfrequency in specific higher-order PT -symmetric electronic systems can be exploited to realize a robust wireless power transfer platform locked to the frequency of operation. this effect is prominent even for the mid-range wireless power transfer with loose magnetic coupling. The third-order PT circuit described here also exhibits bifurcating eigenfrequencies, which, together with the invariant and real one, may enable a multi-functional platform that provides wireless charging and sensing at the same time. Further studies may make a breakthrough in dynamic and alignment-free wireless charging technology with extended range.

My Proposed generalized PTX -symmetry condition compared with the standard PT -symmetry offers greater design flexibility in manipulating resonance linewidths and Q-factors, while exhibiting eigenfrequencies identical to the associated PT -symmetric system. I have extended the idea of a generalized PT -symmetric system with unbalanced, reciprocally-scaled gain and loss to the optical PT -symmetric systems. Specifically, I have demonstrated this idea using the PT -symmetric metasurfaces, and shown that the CPA-laser mode can be realized even though the system has a small net gain. My results may provide new directions for advances in PT -symmetry and its electromagnetic, acoustic, and circuit applications via breaking the gain/loss balance and eradicating the threshold gain/loss for reaching exotic properties of PT -symmetry, such as the and CPA-laser mode and exceptional points.

Although the PT -symmetric electronic circuits platform which have been studied in this thesis consist of one (multi) pair coupled oscillators, but it is not a required condition for the PT -symmetric system and a non-oscillators circuit system may satisfy the Parity and Time symmetry condition. Such systems may contain one or multi pairs of coupled RL (-RL) circuit (series inductor- resistance one with gain, -R, one with loss, R); This non-oscillators system is invariant under combined parity and time operations and similar to the oscillator PT -symmetric system may provide high spectral resolution and high sensitivity for sensing applications like non-destructive eddy current test where the device under test (metal surface) is modeled as an series RL circuit. This eddy current sensing technique which may be considered as future work, is potentially revolutionary to ultra-sensitive non-destructive eddy current testing in which the traditional eddy current test is unable to measure the low conductivity (e.g. superalloy) with high accuracy.

APPENDIX: COPYRIGHT PERMISSIONS

In this appendix, I present the copyright permissions for the articles, whose contents were used in this thesis. The list of the articles includes an article in Nature Electronic (Chen et al., 2018, Nat. Electron.), an article in IEEE sensor Journals (Sakhdari et al., 2018, IEEE Sensor), an article in IEEE Transaction on Antenna and Propagation (Hajizadegan et al., 2019, IEEE TAP), an article in Physical Review Letter (Sakhdari et al., 2019, PRL), an article in Physical Review Research (Sakhdari et al., 2020, PRR) and an article in Physical Review Applied (Sakhdari et al., 2018, PR Applied).



Generalized parity–time symmetry condition for enhanced sensor telemetry

Author: Pai-Yen Chen, Maryam Sakhdari, Mehdi Hajizadegan, Qingsong Cui, Mark Ming-Cheng Cheng et al.

Publication: Nature Electronics

Publisher: Springer Nature

Date: May 14, 2018

Copyright © 2018, Springer Nature

SPRINGER NATURE

Author Request:

If you are the author of this content (or his/her designated agent) please read the following. If you are not the author of this content, please click the Back button and select no to the question "Are you the Author of this Springer Nature content?"

Ownership of copyright in original research articles remains with the Author, and provided that, when reproducing the contribution or extracts from it or from the Supplementary Information, the Author acknowledges first and reference publication in the Journal, the Author retains the following non-exclusive rights:

To reproduce the contribution in whole or in part in any printed volume (book or thesis) of which they are the author(s).

The author and any academic institution, where they work, at the time may reproduce the contribution for the purpose of course teaching.

To reuse figures or tables created by the Author and contained in the Contribution in oral presentations and other works created by them.

To post a copy of the contribution as accepted for publication after peer review (in locked Word processing file, of a PDF version thereof) on the Author's own web site, or the Author's institutional

repository, or the Author's funding body's archive, six months after publication of the printed or online edition of the Journal, provided that they also link to the contribution on the publisher's website.

Authors wishing to use the published version of their article for promotional use or on a web site must request in the normal way.

If you require further assistance please read Springer Nature's online [author reuse guidelines](#).

For full paper portion: Authors of original research papers published by Springer Nature are encouraged to submit the author's version of the accepted, peer-reviewed manuscript to their relevant funding body's archive, for release six months after publication. In addition, authors are encouraged to archive their version of the manuscript in their institution's repositories (as well as their personal Web sites), also six months after original publication.

v1.0

**Ultrasensitive, Parity-Time-Symmetric Wireless Reactive and Resistive Sensors**

Author: Maryam Sakhdari

Publication: IEEE Sensors Journal

Publisher: IEEE

Date: 1 Dec.1, 2018

Copyright © 2018, IEEE

Thesis / Dissertation Reuse

The IEEE does not require individuals working on a thesis to obtain a formal reuse license, however, you may print out this statement to be used as a permission grant:

Requirements to be followed when using any portion (e.g., figure, graph, table, or textual material) of an IEEE copyrighted paper in a thesis:

- 1) In the case of textual material (e.g., using short quotes or referring to the work within these papers) users must give full credit to the original source (author, paper, publication) followed by the IEEE copyright line © 2011 IEEE.
- 2) In the case of illustrations or tabular material, we require that the copyright line © [Year of original publication] IEEE appear prominently with each reprinted figure and/or table.
- 3) If a substantial portion of the original paper is to be used, and if you are not the senior author, also obtain the senior author's approval.

Requirements to be followed when using an entire IEEE copyrighted paper in a thesis:

- 1) The following IEEE copyright/ credit notice should be placed prominently in the references: © [year of original publication] IEEE. Reprinted, with permission, from [author names, paper title, IEEE publication title, and month/year of publication]

2) Only the accepted version of an IEEE copyrighted paper can be used when posting the paper or your thesis on-line.

3) In placing the thesis on the author's university website, please display the following message in a prominent place on the website: In reference to IEEE copyrighted material which is used with permission in this thesis, the IEEE does not endorse any of [university/educational entity's name goes here]'s products or services. Internal or personal use of this material is permitted. If interested in reprinting/republishing IEEE copyrighted material for advertising or promotional purposes or for creating new collective works for resale or redistribution, please go to http://www.ieee.org/publications_standards/publications/rights/rights_link.html to learn how to obtain a License from RightsLink.

If applicable, University Microfilms and/or ProQuest Library, or the Archives of Canada may supply single copies of the dissertation.



RightsLink®



High-Sensitivity Wireless Displacement Sensing Enabled by PT-Symmetric Telemetry

Author: Mehdi Hajizadegan

Publication: Antennas and Propagation, IEEE Transactions on

Publisher: IEEE

Date: May 2019

Copyright © 2019, IEEE

Thesis / Dissertation Reuse

The IEEE does not require individuals working on a thesis to obtain a formal reuse license; however, you may print out this statement to be used as a permission grant:

Requirements to be followed when using any portion (e.g., figure, graph, table, or textual material) of an IEEE copyrighted paper in a thesis:

- 1) In the case of textual material (e.g., using short quotes or referring to the work within these papers) users must give full credit to the original source (author, paper, publication) followed by the IEEE copyright line © 2011 IEEE.
- 2) In the case of illustrations or tabular material, we require that the copyright line © [Year of original publication] IEEE appear prominently with each reprinted figure and/or table.
- 3) If a substantial portion of the original paper is to be used, and if you are not the senior author, also obtain the senior author's approval.

Requirements to be followed when using an entire IEEE copyrighted paper in a thesis:

- 1) The following IEEE copyright/ credit notice should be placed prominently in the references: © [year of original publication] IEEE. Reprinted, with permission, from [author names, paper title, IEEE publication title, and month/year of publication]
- 2) Only the accepted version of an IEEE copyrighted paper can be used when posting the paper or your thesis on-line.

3) In placing the thesis on the author's university website, please display the following message in a prominent place on the website: In reference to IEEE copyrighted material which is used with permission in this thesis, the IEEE does not endorse any of [university/educational entity's name goes here]'s products or services. Internal or personal use of this material is permitted. If interested in reprinting/republishing IEEE copyrighted material for advertising or promotional purposes or for creating new collective works for resale or redistribution, please go to http://www.ieee.org/publications_standards/publications/rights/rights_link.html to learn how to obtain a License from RightsLink.

If applicable, University Microfilms and/or ProQuest Library, or the Archives of Canada may supply single copies of the dissertation.



21-Feb-2020

This license agreement between the American Physical Society ("APS") and Maryamsadat Sakhdari ("You") consists of your license details and the terms and conditions provided by the American Physical Society and SciPris.

Licensed Content Information

License Number: RNP/20/FEB/023002

License date : 21-Feb-2020

DOI: 10.1103/PhysRevLett.123.193901

Title : Experimental Observation of \mathbb{Z}_2 Symmetry Breaking near Divergent Exceptional Points

Author: M. Sakhdari et al.

Publication: Physical Review Letters

Publisher: American Physical Society

Cost: USD \$ 0.00

Request Details

Does your reuse require significant modifications: No

Specify intended distribution

locations:

United States

Reuse Category: Reuse in a thesis/dissertation

Requestor Type : Student

Items for Re use : Whole Article

Format for Re use : Electronic

Information about New Publication:

University/Publisher: University of Illinois at Chicago

Title of dissertation/thesis: Parity-time symmetric telemetry systems for wearable and implantable sensors

Author(s): Mayam sakhdari

Expected completion date : Feb. 2020

License Requestor Information

Name : Maryamsadat Sakhdari

Affiliation: Individual

Email Id: msakhd2@uic.edu

Country: United States

TERMS AND CONDITIONS

The American Physical Society (APS) is pleased to grant the Requestor of this license a non-exclusive, non-transferable permission,

limited to Electronic format, provided all criteria outlined below are followed.

1. You must also obtain permission from at least one of the lead authors for each separate work, if you haven't done so already. The author's name and affiliation can be found on the first page of the published Article.
2. For electronic format permissions, Requestor agrees to provide a hyperlink from the reprinted APS material using the source material's DOI on the web page where the work appears. The

hyper link should use the standard DOI resolution URL, <http://dx.doi.org/{DOI}>. The hyperlink may be embedded in the copyright credit line.

3. For print format permissions, Requestor agrees to print the required copyright credit line on the first page where the material appears: "Reprinted (abstract/excerpt/figure) with permission from [(FULL REFERENCE CITATION) as follows:

Author's Names, APS Journal Title, Volume Number, Page Number and Year of Publication.] Copyright (YEAR) by the American Physical Society."

4. Permission granted in this license is for a one-time use and does not include permission for any future editions, updates, databases, formats or other matters. Permission must be sought for any additional use.

5. Use of the material does not and must not imply any endorsement by APS.

6. APS does not imply, purport or intend to grant permission to reuse materials to which it does not hold copyright. It is the requestor's sole responsibility to ensure the licensed material is original to APS and does not contain the copyright of another entity, and that the copyright notice of the figure, photograph, cover or table does not indicate it was reprinted by APS with permission from another source.

7. The permission granted herein is personal to the Requestor for the use specified and is not transferable or assignable without express written permission of APS. This license may not be amended except in writing by APS.

8. You may not alter, edit or modify the material in any manner.

9. You may translate the materials only when translation rights have been granted.

10. APS is not responsible for any errors or omissions due to translation.

11. You may not use the material for promotional, sales, advertising or marketing purposes.

12. The foregoing license shall not take effect unless and until APS or its agent, Aptara, receives payment in full in accordance with Aptara Billing and Payment Terms and Conditions, which are incorporated herein by reference.

13. Should the terms of this license be violated at any time, APS or Aptara may revoke the license with no refund to you and seek relief to the fullest extent of the laws of the USA. Official written notice will be made using the contact information provided with the permission request. Failure to receive such notice will not nullify revocation of the permission.

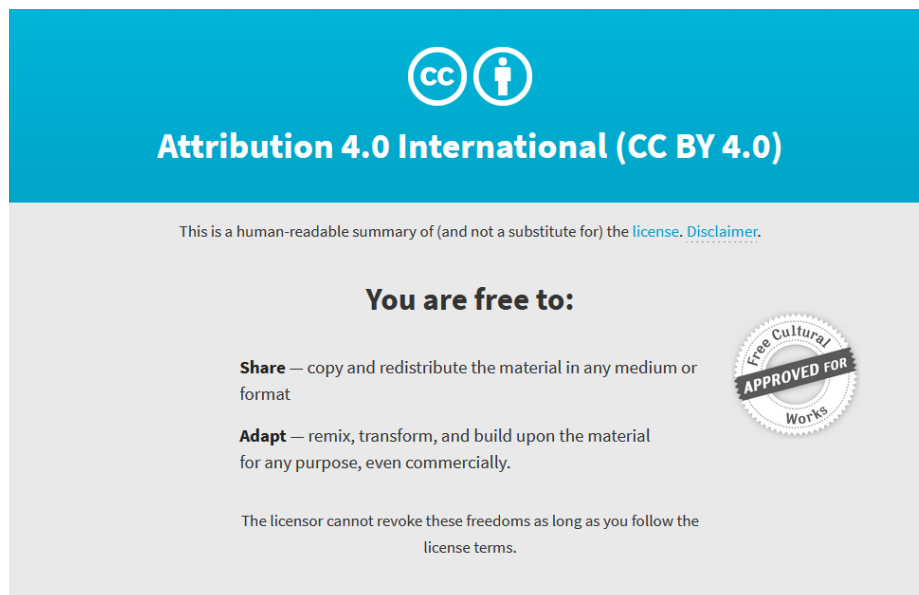
14. APS reserves all rights not specifically granted herein.

15. This document, including the Aptara Billing and Payment Terms and Conditions, shall be the entire agreement between the parties relating to the subject matter hereof.

Sakhdari, M., et al. "Experimental Observation of P T Symmetry Breaking near Divergent Exceptional Points." *Physical review letters* 123.19 (2019): 193901.

Reuse & Permissions

It is not necessary to obtain permission to reuse this article or its components as it is available under the terms of the [Creative Commons Attribution 4.0 International](https://creativecommons.org/licenses/by/4.0/) license. This license permits unrestricted use, distribution, and reproduction in any medium, provided attribution to the author(s) and the published article's title, journal citation, and DOI are maintained. Please note that some figures may have been included with permission from other third parties. It is your responsibility to obtain the proper permission from the rights holder directly for these figures.





04-Nov-2019

This license agreement between the American Physical Society ("APS") and Maryamsadat Sakhdari ("You") consists of your license details and the terms and conditions provided by the American Physical Society and SciPris.

Licensed Content Information

License Number: RNP/19/NOV/020010

License date: 04-Nov-2019

DOI: 10.1103/PhysRevApplied.10.024030

Title: Low-Threshold Lasing and Coherent Perfect Absorption in Generalized PT-Symmetric Optical Structures

Author: Maryam Sakhdari et al.

Publication: Physical Review Applied

Publisher: American Physical Society

Cost: USD \$ 0.00

Request Details

Does your reuse require significant modifications: No

Specify intended distribution

locations:

United States

Reuse Category: Reuse in a thesis/dissertation

Requestor Type : Author of requested content

Items for Re use : Whole Article

Format for Re use : Electronic and Print

Total number of print copies: Up to 1000

Information about New Publication:

University/Publisher:

Title of dissertation/thesis: Parity-time symmetric telemetry systems for wearable and implantable sensors

Author(s): Maryam Sakhdari

Expected completion date : Nov. 2019

License Requestor Information

Name : Maryamsadat Sakhdari

Affiliation: Individual

Email Id: msakhd2@uic.edu

Country: United States

American Physical Society

Reuse and Permissions License

TERMS AND CONDITIONS

The American Physical Society (APS) is pleased to grant the Requestor of this license a non-exclusive, non-transferable permission,

limited to Electronic and Print format, provided all criteria outlined below are followed.

1. You must also obtain permission from at least one of the lead authors for each separate work, if you haven't done so already. The author's name and affiliation can be found on the first page of the published Article.
2. For electronic format permissions, Requestor agrees to provide a hyperlink from the reprinted APS material using the source material's DOI on the web page where the work appears. The hyperlink should use the standard DOI resolution URL, <http://dx.doi.org/{DOI}>. The hyperlink may be embedded in the copyright credit line.
3. For print format permissions, Requestor agrees to print the required copyright credit line on the first page where the material appears: "Reprinted (abstract/excerpt/figure) with permission from [(FULL REFERENCE CITATION) as follows:
Author's Names, APS Journal Title, Volume Number, Page Number and Year of Publication.] Copyright (YEAR) by the American Physical Society."
4. Permission granted in this license is for a one-time use and does not include permission for any future editions, updates, databases, formats or other matters. Permission must be sought for any additional use.
5. Use of the material does not and must not imply any endorsement by APS.
6. APS does not imply, purport or intend to grant permission to reuse materials to which it does not hold copyright. It is the requestor's sole responsibility to ensure the licensed material is original to APS and does not contain the copyright of another entity, and that the copyright notice of the figure, photograph, cover or table does not indicate it was reprinted by APS with permission from another source.

7. The permission granted herein is personal to the Requestor for the use specified and is not transferable or assignable without express written permission of APS. This license may not be amended except in writing by APS.
8. You may not alter, edit or modify the material in any manner.
9. You may translate the materials only when translation rights have been granted.
10. APS is not responsible for any errors or omissions due to translation.
11. You may not use the material for promotional, sales, advertising or marketing purposes.
12. The foregoing license shall not take effect unless and until APS or its agent, Aptara, receives payment in full in accordance with Aptara Billing and Payment Terms and Conditions, which are incorporated herein by reference.
13. Should the terms of this license be violated at any time, APS or Aptara may revoke the license with no refund to you and seek relief to the fullest extent of the laws of the USA. Official written notice will be made using the contact information provided with the permission request. Failure to receive such notice will not nullify revocation of the permission.
14. APS reserves all rights not specifically granted herein.
15. This document, including the Aptara Billing and Payment Terms and Conditions, shall be the entire agreement between the parties relating to the subject matter hereof.

VITA

NAME: Maryam Sakhdari

EDUCATION: B.A., Electrical Engineering, IRAN University of Science and Technology, Tehran, IRAN, 2009

M.S., Electrical Engineering, Tarbiat Modares University, Tehran, IRAN, 2013

Ph.D., Electrical and Computer Engineering, University of Illinois at Chicago, IL, 2020

PUBLICATION: P. Y. Chen, **M. Sakhdari**, and M. Hajizadegan, “Parity-Time (PT)-Symmetric Wireless Telemetric Sensors and Systems,” U.S. Patent Application No. 16/504, 664.

P. Y. Chen, M. Farhat, **M. Sakhdari**, and Hakan Bagci, “Graphene Nanoelectromagnetism: from Radio-Frequency to Mid-Infrared,” in “Carbon-Based Nanoelectromagnetics,” 31, 2019.

M. Sakhdari, M. Hajizadegan, and P-Y Chen “Robust Extended-Range Wireless Power Transfer Using a Higher-Order PT-Symmetric Platform,” vol. 2, 013152, 2020.

M. Sakhdari, et al, “Experimental observation of PT symmetry breaking near divergent exceptional points,” Physical Review Letter, vol. 123, 193901, 2019.

M. Hajizadegan, **M. Sakhdari**, and P. Y. Chen, “High-Sensitivity Wireless Displacement Sensing Enabled by PT-Symmetric Telemetry,” IEEE Transaction on Antenna and Propagation, vol. 67, 3445-3449, 2019.

P. Y. Chen, **M. Sakhdari**, M. Hajizadegan, Q. Cui, M. Cheng, R. El-Ganainy, and A. A. Alù, “Generalized Parity-Time Symmetry Condition for Enhanced Sensor Telemetry,” Nature electronics, vol. 1, 297, 2018.

M. Sakhdari, N. M. Estakhri, H. Bagci, and P. Y. Chen, “Low-Threshold Lasing and Coherent Perfect Absorption in the Generalized PT-Symmetric Optical Structures,” *Physical Review Applied*, Vol. 10, 024030, 2018.

M., Sakhdari, M., Hajizadegan, Y., Li, Cheng, M.M.C., J.C. Hung, and P.Y., Chen, “Ultrasensitive, Parity-Time-Symmetric Wireless Reactive and Resistive Sensors,” *IEEE Sensors Journal*, vol. 18, 2018.

M. Sakhdari, M. Farhad, P. Y. Chen, “PT-symmetric metasurfaces: wave manipulation and sensing using singular point.” *New Journal of Physics*, vol. 19, 065002, 2017.

Q. Cui, **M. Sakhdari**, B. Chamlagain, H.J. Chuang, Y. Liu, M. Cheng, Zh. Zhou, P.Y. Chen,” Ultrathin and atomically flat transition-metal oxide: promising building blocks for metal-insulator electronics”,*ACS Applied Materials & Interfaces*, vol. 8, 34552-34558, 2017.

H. H. Huang, **M. Sakhdari**, M. Hajizadegan, A. Shahini, D. Akinwandeand, P. Y. Chen , “Toward transparent and self-activated graphene harmonic transponder sensors.”, *Applied Physics Letters*, vol. 108(17), p.173503,2016.

P.Y. Chen, M. Hajizadegan, M.Sakhdari, and A. Alù,“giant photoresponsivity of midinfrared hyperbolic metamaterials in the photon-assisted-tunneling regime,” *Physical Review Applied*, 5(4), p.041001, 2016

M. Sakhdari, M. Hajizadegan, M. Farhat, and P. Y. Chen, “Efficient, broadband and wide-angle hot-electron transduction using metal-semiconductor hyperbolic metamaterials,” *Nano Energy*, 26, pp.371-381, 2016.

M. Hajizadegan, V. Ahmadi, and M. Sakhdari “design and analysis of ultrafast and tunable all optical metamaterial switch enhanced by metal nanocomposite,” *Journal of Lightwave Technology*, vol. 31, pp. 1877-1883, 2013.

M. Hajizadegan, Davood Fathi, M. Sakhdari “All-optical metamaterial switch based on Kerr effect with MWCNT composite,” *Phys. E*, vol. 48, pp. 1-6, 2013.

Fathi, Davood, **M. Sakhdari**, and M. Hajizadegan. "All optical SRR switch using carbon nanotube composite." *Optik-International Journal for Light and Electron Optics* 125.16, pp. 4405-4410, 2014.

M. Sakhdari, et al. "giant photoresponsivity of midinfrared hyperbolic metamaterials in the photon-assisted-tunneling regime," *Physical Review Applied*, 5(4), p.041001, 2016

M. Sakhdari, et al. "Efficient, broadband and wide-angle hot-electron transduction using metal-semiconductor hyperbolic metamaterials," *Nano Energy*, 26, pp.371-381, 2016.

Conferences

M. Sakhdari, P. Y. Chen, "Parity-Time Symmetric Telemetry Sensor Systems and Wireless Power Transfer", International Conference on Microwaves for Intelligent Mobility (ICMIM), Detroit, Michigan, 2019.

M. Sakhdari, P. Y. Chen, "Efficient and Misalignment-Robust PT-Symmetric Wireless Power Transfer", 2019 IEEE International Symposium on Antennas and Propagation/USNC-URSI National Radio Science meeting, Atlanta, Georgia, 2019.

M. Sakhdari, P. Y. Chen, "First and Higher-Order PT-Symmetric Telemetric Sensing Systems", National Radio Science Meeting (URSI 2017), Boulder, Colorado, US, 2018.

M. Sakhdari, P. Y. Chen, "Ultrasensitive telemetric sensor based on adapted parity-time symmetry", 2017 IEEE International Symposium on Antennas and Propagation/USNC-URSI National Radio Science meeting, San Diego, California, USA, 2017.

M. Sakhdari, P. Y. Chen, "Parity-time-reciprocal symmetry in radio-frequency electronics", National Radio Science Meeting (URSI 2017), Boulder, Colorado, US, 2017.

M. Hajizadegan, **M. Sakhdari**, P-Y. Chen, "PT-Symmetric Inductive Displacement Sensors", IEEE MTT-S International Microwave Workshop Series on Advanced Materials and Processes for RF and THz Applications (IMWS-AMP), Ann arbor, Michigan, US, 2018.

M. Hajizadegan, **M. Sakhdari**, P-Y. Chen, “Hyperbolic metamaterial-based plasmoelectronic nanodevices for detection and harvesting of infrared radiation”, Micro-and Nanotechnology Sensors, Systems, and Applications X, 2018.

M. Sakhdari, P-Y. Chen, “ Transparent and Self-Activated Harmonic Sensor Using Integrated Graphene Antennas and Circuits”, 2016 IEEE International Symposium on Antennas and Propagation/USNC-URSI National Radio Science meeting, Fajardo, Puerto Rico, 2016.

M. Sakhdari, P-Y. Chen, “Giant Photoresponsivity of Mid-Infrared Hyperbolic Metamaterials in the Quantum Regime”, National Radio Science Meeting (URSI 2016), Boulder, Colorado, US, 2016.

shahini, **M. Sakhdari**, M. Hajizadegan, P-Y. Chen, “Self-Powered and Transparent All-Graphene Biosensor”, IEEE SENSORS 2016 Conference in Orlando, Florida, 2016.

M. Sakhdari, Mohammad Kazem Moravvej-Farshi, and Arash Karimkhani “Photonic Switch Based on Nano-structured Metamaterial” The 19th Iranian Conference on Optics and Photonics and the fifth Iranian Conference on Photonics Engineering (ICEP 2013), Zahedan University, Iran, 2013.

M. Sakhdari, A. Karimkhani, M. K. Moravvej-farshi, “Nanostructure Metamaterial All-optical Switch whit Optimum Dimensions”, International Congress on Nanoscience & Nanotechnology (ICNN2012), Kashan University, Iran, 2012.

M. Hajizadegan, and **M. Sakhdari**, V. Ahmadi “Design of a kerr effect based terahertz all-optical switch using metallic nanocomposite metamaterial structure” Second Conference on Millimeter -Wave and Terahertz Technologies (MMWaTT), Tehran University, Iran, 2012.

M. Hajizadegan, and **M. Sakhdari**, V. Ahmadi “Design of a tunable all-optical metamaterial switch enhanced by metal nanocomposite” 19th Iranian Conference on Optics and Photonics (ICOP), Zahedan University, Iran, 2013.

M. Hajizadegan, and **M. Sakhdari**, V. Ahmadi “Investigation of density and distribution of metal nanoparticles effect on the plasmonic absorption

in metal nanocomposite using FEM” (In Persian Language), 1st National Congress and Workshop on Nanoscience and Nanotechnology (NCWNN), Tarbiat Modares University, Tehran, Iran, 2013.

M. Sakhdari, “The adaptive front lighting system based on road image processing and lane detection”, the Second International Symposium on Computing in Science and Engineering (ISCSE), Gediz University, Turkish, 201.